Fabrication & Characterization of Titania-Germanium (TiO_2- Ge) Based Nanocomposites

By

Asma Nazir
Reg. No. **05-FBAS/PHDPHY/S10**

Department of Physics
Faculty of Basic and Applied Sciences
International Islamic University, Islamabad
Pakistan
2018

Fabrication & Characterization of Titania-Germanium (TiO_2- Ge) Based Nanocomposites

By

Asma Nazir
Reg. No. **05-FBAS/PHDPHY/S10**

Supervisor

Dr. Shaista Shahzada

Co-Supervisor

Prof. Dr. Ehsan Ullah Khan (T.I)
(HEC Supervisor)

Department of Physics (FC)
Faculty of Basic and Applied Sciences
International Islamic University, Islamabad
Pakistan

2018

Fabrication & Characterization of Titania-Germanium (TiO_2- Ge) Based Nanocomposites

By

Asma Nazir
Reg. No. **05-FBAS/PHDPHY/S10**

A Thesis submitted in Partial Fulfillment of the requirements for the degree of ***Doctor of Philosophy in Physics*** at the Department of Physics (FC), Faculty of Basic and Applied Sciences, International Islamic University, Islamabad

Supervisor
Dr. Shaista Shahzada

Co-Supervisor
Prof. Dr. Ehsan Ullah Khan (T.I)
(HEC Supervisor)

Department of Physics (FC)
Faculty of Basic and Applied Sciences
International Islamic University, Islamabad
Pakistan

2018

Author's Declaration

I, **Asma Nazir** Reg. No. **05-FBAS/PHDPHY/S10** hereby state that my Ph.D. thesis titled: **Febrication & Characterization of Titania-Germanium (TiO_2-Ge) Based Nanocomposites** is my own work and has not been submitted previously by me for taking any degree from this university, **International Islamic University, Sector H-10, Islamabad, Pakistan** or anywhere else in the country/world.

At any time if my statement is found to be incorrect even after my Graduation the university has the right to withdraw my Ph.D. degree.

Asma Nazir
Reg. No. **05-FBAS/PHDPHY/S10**
Dated: **31/08/2018**

Plagiarism Undertaking

I solemnly declare that research work presented in the thesis titled: **Febrication & Characterization of Titania-Germanium (TiO_2-Ge) Based Nanocomposites** is solely my research work with no significant contribution from any other person. Small contribution/help wherever taken has been duly acknowledged and that complete thesis has been written by me.

I understand the zero tolerance policy of the HEC and University, **International Islamic University, Sector H-10, Islamabad, Pakistan** towards plagiarism. Therefore, I as an Author of the above titled thesis declare that no portion of my thesis has been plagiarized and any material used as reference is properly referred/cited.

I undertake that if I am found guilty of any formal plagiarism in the above titled thesis even after award of Ph.D. degree, the university reserves the rights to withdraw/revoke my Ph.D. degree and that HEC and the University has the right to publish my name on the HEC/University Website on which names of students are placed who submitted plagiarized thesis.

(Asma Nazir)

Certificate of Approval

This is to certify that the research work presented in this thesis, entitled: **Febrication & Characterization of Titania-Germanium (TiO_2-Ge) Based Nanocomposites** was conducted by **Ms. Asma Nazir,** Reg. No. **05-FBAS/PHDPHY/S10** under the supervision of **Dr. Shaista Shahzada** no part of this thesis has been submitted anywhere else for any other degree. This thesis is submitted to the **Department of Physics, FBAS, IIU, Islamabad** in partial fulfillment of the requirements for the degree of **Doctor of Philosophy in Physics, Department of Physics, Faculty of Basic & Applied Science, International Islamic University, Sector H-10, Islamabad, Pakistan.**

_____

Asma Nazir

Examination Committee:

a) External Examiner 1:
Prof. Dr. Anis ur Rehman _____
Physis Department,
COMSATS, Islamabad.

b) External Examiner 2:
Dr. Shafqat Karim _____
Head Nanomaterial Research Group,
Physics Division, PINSTECH, P.O.
Nilore, Islamabad.

c) Internal Examiner:
Dr. Saba Shafaq _____
Assistant Professor

Supervisor:
Dr. Shaista Shahzada _____
Associate Professor

Co-Supervisor:
Prof. Dr. Ehsan Ullah Khan, T.I _____

Chairperson Physics Deptt (FC):
Dr. Shaista Shahzada _____

Dean FBAS:
Prof. Dr. Arshad Zia _____

Dedicated to

My Parents and Teachers

Acknowledgement

It gives me an immense pleasure and satisfaction to acknowledge the endowment of **Allah Almighty,** the most gracious, compassionate and beneficent to His creature, who strengthened me in bringing this tired research journey to its destination successfully.

I am deeply indebted and wish my utmost gratitude to the worth mentioning supervision of **Dr. Shaisata Shahzada** and **Prof. Dr. Ehsan Ullah Khan (T.I)** who guided and supported me during my PhD duration. Moreover, their supervision enabled me to develop an understanding of the field and honestly without their sincere efforts I was unable to end up with this hard task.

I am obliged to **Dr. Muhammad Mushtaq, DG NILOP** for providing me opportunity to work at **NILOP,** Islamabad, exclusively **Dr. Ali Nadeem** and **Dr. Arshad Janjua** for facilitating in Lab work and characterizations. I am thankful to **Dr. Manzar** (advisor) and **Dr. Waqar** at **Physics Department CIIT**, Islamabad for their valuable suggestions and help in various characterizations. Special kind of thanks to **Mr. Tahir Mehmood** at **Material Science Engineering Department IST,** Islamabad.

Special gratitude to **Prof. Dr. Ahmed Shujah** as I have been benefited a lot from **Advanced Engineering Lab** at **IIUI**, Islamabad through discussions after acquiring results and interpreting them. **Engineer Muhammad** Ali and **Engineer Shoaib Alam** had been very much co-operative in discussing results to achieve some worth-ful outcomes.

In addition, I would express my sincere thanks to all faculty members of **Department of Physics IIUI,** Islamabad especially to **Dr. Muhammad Mumtaz, Dr. Javed Iqbal Saggu, Dr. Waqar Ahmed Adil Syed** and **Dr. Rehana Mustafa.** I also express my thanks to all staff of **Physics Department, IIUI,** for their various services. Thanks to all other faculty members of my university for their sincere appreciations, comments, and suggestions.

I shall express my heartiest thanks to my research colleagues **Anbrain Fatima Tanzeeha, Kaneez Fatima** and especially to **Maria, Ghulam Aisha, Hira Shakil** and **Abdul Jabbar** and for being very supportive and co-operative throughout my research work. I would like to take the opportunity to gratitude old friend **Alvina Butt** for her constant support and motivation to complete the studies. **Dr. Bilal Khan Niazi** has also

been a very supportive for helping me during trouble shooting in research and academics.

There are some people without their support and help this project would not have been accomplished like all the members of Laser Spectrosopy Lab; specially **Dr. Sami Ul Haq**, **Mr. Mahmood Shah**, **Mr. Qamar Abbas**, **Mr. M. Ashraf** , **Mr. Mudassir** and **Mr. Waheed**.

Finally, I need to thanks some individuals on the personal side of my life. To my loving parents, brothers and sisters, my sincerest gratitude for all they have done. Especially to my elder brother, **Saleem Ahmed** who had been a great helping hand and stood by me during the whole research. I could not wish for a most supportive, loving family, and for them I am deeply thankful and blessed.

Asma Nazir

Content

List of Tables

No table of figures entries found.

List of Figures

No table of figures entries found.

Symbols and Abbreviations

CVD	*Chemical Vapour Deposition*
Dim	*Dimensional*
ε_1	*Dielectric Constant*
e-h	*Electron hole*
E_g	*Energy Bandgap*
δ	*Dislocation Density*
ε_2	*Dielectric Loss*
eV	*Electron Volt*
EDX	*Energy Dispersive X-Ray*
EL	*Electroluminescence*
F-W growth	*Frank-Vander Merwe- Growth*
FWHM	*Full Width At Half Maxima*
Ge	*Germanium*
Hz	*Hertz*
ICDD	*International Centre For Diffraction Data*
I-V	*Current –Voltage*
IR	*Infra-Red*
JCPDS	*Joint Committee On Powder Diffraction Standard*
K_n	*Knudsen Number*
k	*Extinction Coefficient*
LDM	*Low Dimensional Materials*
LED	*Light Emitting Diode*
LBL	*Layer By Layer Deposition*
MOSFET	*Metal Oxide Semiconductor Field Effect Transistor*
µA	*Micro Ampere*
min	*Minutes*
λ_{mph}	*Mean Free Path*
nm	*Nanometer*
NC	*Nanocrystal*
NPLs	*Nano Platelets*
ns	*Nanosecond*
Nd:YAG	*Neodymium: Yttrium Aluminum Garnet*
OFETs	*Organic Field-Effect Transistors*
OE	*Optoelectronic*
PLD	*Pulsed Laser Deposition*

PL	*Photoluminescence*
PV	*Photo Voltaic*
QCE	*Quantum Confinement Effect*
η	*Strain*
Si	*Silicon*
SC	*Standard Clean*
Sa/V	*Surface Area to Volume*
S-K growth	*Stranski- Krastonov Growth*
SEM	*Scanning Electron Microscope*
TF	*Thin Film*
TFTs	*Thin Film Transistor*
TiO_2	*Titanium Dioxide/ Titania*
UV	*Ultra Violet*
UV/Vis	*Ultra Violet Visible*
V-W growth	*Volmer- Weber Growth*
V_H	*Hall Voltage*
XRD	*X-Ray Diffraction*

Abstract

Composite nano-films of TiO_2-Ge were grown by 'pulsed laser deposition' (PLD) technique on Si wafers while deposition conditions were changed. Firstly single run deposition for a longer time (30 min) with varying Ge concentration in N and p-type polished Si wafers. Secondly films were deposited as single, bi- and tri-layers on n-type polished and unpolished Si wafers such that each layer was deposited for 5 mins. In the first batch of samples target-substrate distance was varied to find its effect on optoelectronic properties of film. It was observed that Ge concentration decreased as target-substrate separation was increased. Also substrate type and separation between target and substrate effected the crystallinity, optical & electrical response of film. On p-type (111) Si wafer thin films showed dominant amorphous behaviour with decreasing Ge concentration. Thin films deposited on Si wafer showed an improvement in crystallinity as target-substrate distance was increased resulting in decrease in crystallite size, increase in defects and strains. Raman spectroscopic results and EDX analysis confirmed the Ge presence in all the samples. Ge identification in Raman and its non-identification through XRD may possibly be due to non-crystalline nature of Ge. Composite nature was identified by the Ge peak related to cubic structure rather than tetragonal (i.e. did not follow crystalline structure of TiO_2) i.e. no doping occurred. Films grown at a distance of 6 cm from the target showed better optoelectronic properties which exhibited minimum reflectance but maximum direct and indirect absorption transitions it is also confirmed by its photoluminescence (PL) response. It has a constant refractive index with a stable extinction coefficient. This film demonstrated a positive dielectric constant and a negligible dielectric loss confirming its stable optoelectronic behaviour which was confirmed by its I-V response. Better optoelectronic response for the above mentioned film can be positively due to strains and size reduction of crystallite size. In the second batch of experiment single, di- and tri-layered composite films were grown on polished and n-type unpolished Si (100) wafer. Amorphous nature was observed dominantly in all the samples. Di-layered film deposited on polished n-type Si wafer showed a better optical response which is due to minimum variation in its n. Maximum direct and indirect transitions are also observed in it and a broad PL peak is observed around 2-3.5 eV. Although it does not show better electrical properties as compared to tri-layered thin films but overall optoelectronic response of this film is better as compared to other samples. The reason may be the

outcome of crystalline nature of film. Thin films (for 5 min) shows reduced crystallinity and hence optoelectronic response in comparison to that for 30 min, this variance can be attributed to the reduced thickness of film. Single layer film has variable n responsible for lower dielectric constant and hence lowest electrical response.

Chapter 1

INTRODUTION

This section explains introduction to

a. Research project describing:
- Motivation
- Objectives
- Thesis structure

b. Application based materials.

c. Material used in this project

d. Film Growth Process.

e. Pulsed Laser Deposition (PLD) Process.

Chapter 1

1 Introduction

Optoelectronics has emerged as fascinating field in research and industry. Photo dependent electrical responses of materials to a specific or whole spectral range makes them to be exploited as sensors, photocells, actuators etc. Importance of these materials has been increased manifolds due to increasing need for energy source. Conserving the environment is the main driving factor to device and derive alternative sources as replacement to previously adopted conventional energy sources which include coal, natural gas, fuel and nuclear energy to harness electricity. A clean renewable alternative to all the conventional energy sources is solar energy. Initially Si was studied for photovoltaic (PV) applications. Amorphous silicon (a-Si) photovoltaic (PV) cell being inexpensive had a drawback of photo induced degradation in PV properties. Therefore many crystalline materials such as silicon, "gallium indium phosphide" (GaInP), "gallium arsenide" (GaAs), "Copper Indium Gallium Selenide" (CIGS) and "Cadmium Telluride" (CdTe) were then considered for photovoltaic applications[1]. However, the fabrication processes of all the above mentioned materials are complex and expensive. Moreover, CdTe based solar cells are environmentally instable, which is the biggest disadvantage, therefore there is a need to develop such PV materials which are low cost and easy to fabricate [2].

Titanium dioxide-germanium (TiO_2–Ge) is a nanocomposite which is thermodynamically stable having homogenous distribution of Ge nano-dots in TiO_2 matrix is considered as the potential candidate to serve as optoelectronic materials. Ti having low electronegativity 1.54 Pauling is oxidizes easily as compared to Ge having a comparatively higher electronegativity i.e. 2.1 Pauling [3]. The enthalpies (ΔH_f°) for the formation of GeO_2 & TiO_2 are -580 kJ/mol & -944.0 kJ/mol [3] respectively. So, GeO_2 is less stable as compared to TiO_2. These oxidation kinetics of Ge and Ti are helpful in developing thermodynamically stable nanocomposite of TiO_2–Ge.

Nanostructured crystalline Titania (TiO_2) being semiconductor is extensively utilized in photocatalysis applications because band gap of bulk TiO_2 is '3.2 eV' which lies in ultraviolet (UV) spectral region. Efficiency of TiO_2 based solar cells can be increased with modification in band gap. Thus, different modifications are done in TiO_2 nano particles by different methods, for example, doping [4], size optimization, dye sensitization [5], various surface modifications [6], etc. One of the most successful way in this regard is dye sensitization where organic nature of dye is responsible to charge transport and instability issues.

TiO_2–Ge nanocomposite being stable inorganic composite with improved optoelectronic properties can replace the dye sensitized TiO_2 by adopting specific fabrication conditions. Thus, this research is mainly focused on the fabrication of the materials for optoelectronic applications. We synthesized TiO_2-Ge composite nanoparticles through Pulsed Laser Ablation process in water as an initial step the work has been published in Canadian Journal of Physics which is ISI indexed journal (Annex I, Paper 1). The work presented in this dissertation is based on the fabrication of TiO_2-Ge nanocomposite thin films by ablating composite target (made from bulk TiO_2 and Ge) employing pulsed laser deposition (PLD) technique while changing deposition conditions i.e.

- Single run deposition for a longer time,
- Variation in target-substrate separation.
- Layer by layer deposition (LBL) such that each layer was deposited for a comparatively shorter time.

Various properties including structural, morphological, composition, optical, electrical properties of these samples were then studied using various characterization techniques. X-Ray diffraction (XRD), Energy Dispersive X-Ray spectroscopy (EDX), Raman spectroscopy, Ultra Violet Visible (UV- Vis) spectroscopy, I-V measurement in dark and light were the various tools employed in this research work. Ellipsometry was utilized to find the possible connection between the light absorption with electron hole (e-h) generation, recombination and energy dissipation in near infra-red (IR), ultra violet (UV) and visible region of solar spectrum. A part of this research work has also been published in Arabian Journal for Science and Engineering (Appendix I, Paper 2)

Chapter 1 includes the introduction, scope, summary of research work, thesis organization, literature review on TiO_2, Ge and their composites as well as various models involved in thin film growth, discussion on pulsed laser deposition process and various characterization tools. Chapter 2 is related to chamber design, thin film optimization and experimental details. Chapter 3 consists of structural and compositional analysis of thin films. Chapter 4 and 5 is related to the optical and electrical studies. Conclusions are elaborated in Chapter 6.

1.1 Introduction to Application Based Materials

This section gives a brief description of the materials used in this research, their properties and previous work.

1.1.1 Nanocomposites

The composites, with one of their phase in nanometer (nm) range are called nanocomposites (NC's). Micro-composites and monolithics have been replaced by nanocomposite with the limitation in their preparation involving the control over the stoichiometry and elemental composition. These materials exhibit high performance as a result of exclusive design possibilities and combination of unusual properties [7]. Moving towards nano regime phase interfacial interactions become more prominent thus resulting in the enhancement of material properties. Minimum size limit at which properties change extraordinarily is called 'critical size'. Therefore these changes should be evaluated as to be dependent on the surface area to volume ratio (Sa/V) of the materials. Three types of NC's exist subject to matrix materials as: Ceramic, Metal and Polymer [7].

In thin films (TF's) existence of 'low-dimensional material' (LDM) which can be structured by various methods including co-sputtering, co-evaporation or laser ablation of target. This technology which is now at its initial stage [8-21] is used in manufacturing instrument hard coatings, electronic devices, ornamental and optical coatings since half century [8, 22-24]. Thickness is found to effect properties of film as extremely thin film have high surface to volume ratio which depends on the 'Quantum confinement effect' (QCE) and surface of film.

1.1.2 Optoelectronic Materials

Optoelectronics (OE) is a branch of technology in which semiconductor materials are designed to develop electronic systems and optical devices that not only act as source but also detect and control light (i.e. visible, IR and UV radiations). Commercially available advance OE devices are 'light emitting diodes' (LED's), 'optical waveguides', 'laser diodes', 'electro-optic modulators', and 'photodetectors'[25].

Previously optoelectronic devices were manufactured from "homo and heterostructures", at micro-level which is recently replaced by nano scale heterostructures. Heterostructures are mostly preferred because of following advantages:

1. Employing multiple materials provides a control over the electron hole mobility in a specific direction which is useful in making laser of appreciably high efficiency.
2. Materials with different refractive index can be utilized in making mirror like structures and waveguides from the same material.
3. Fabrication of structures for devices is possible which can radiate or absorb light in a specific wavelength range.
4. Quantum confinement effect (QCE) in electron and holes in very thin layers made out of different materials, thus making the devices that are engineered quantum-mechanically.

Lattice constants of deposit and substrate should be very close to grow crystalline heterostructures. Otherwise these structures may contain a number of defects [26].

Optical and electrical properties of materials depend on the shape and size of semi conducting nanomaterials. Modification in properties arises from the quantum mechanical effects as density of states of electron hole pair changes from discrete to 0-dimensional (Dim.) structures. Small dielectric constant in surrounding media gives a control on the variation in the strength of Coulomb coupling in Electron–hole pairs depending on possible alteration in shape of nanostructures. Therefore the exciton binding energy increases in Nano rods [27], 2-Dim. nanocrystals (NCs) [28]. As a result excitons can easily couple with the emitted photons as the electric field of the photons is not affected in 1-Dim/ 2-Dim. semiconductor nanostructures which have a shortened

fluorescence decay time [3].

2 Dim. colloidal nanocrystals (NCs) being semiconductor in nature are the promising materials for optoelectronic applications. These nanocrystals are commonly named as Nano platelets (NPLs) [29], which are ultra-thin and flat having lateral dimension and thickness is of few to tens of nanometers and several singlelayers respectively [29]. Their applications include light emitting diodes [30], lasers [31], nonlinear optical absorption [32], pseudo capacitors [33], Immunohistopathology [34], Electroluminescent NPLs showing emission at a wavelength of 396 nm, 463 nm, 513nm and 553 nm [35] can be utilized in light emitting diodes [36] etc.

Optical properties of colloidal NCs can be tailored by having a control on geometry and composition depending on synthesis method [37, 38]. 2-Dim. transition metal nanocrystals have been synthesized through generalized synthesis protocol having a well-defined geometry [37, 38]. 2 Dim. nanocrystals of CdSe/CsS encapsulated in water soluble shells are a potential material for single mode lasing [37, 38].

1.2 Application of Materials Used in Experiment

An introduction containing a detailed literature about materials used in this research project have been included in this section. A detailed overview of TF materials including titanium dioxide and germanium, their properties and applications have been explained.

1.2.1 Titania (TiO2)

Titanium dioxide (TiO_2) has been a fascinating material in nanoscience research community due to its exciting features [39, 40].It has three allotropes, i.e rutile, anatase and brookite. Rutile is most stable allotrope in tetragonal crystalline form (E_g= 3.0 eV). Whereas anatase (tetragonal, E_g=3.2 eV) and brookite (orthorhombic, E_g= 1.9 eV) are converted to rutile when annealed.

There is a huge literature available on the studies based on TiO_2 and its application in various fields. Some examples of the application based research are elaborated in Table 1.1. apart from bulk & micro scale, studies related to quantum confinement are conducted in doped (Al, Cr, Mn) [41, 42] and undoped [6, 43, 44] in rutile [45] and

anatase [41]. It was observed that absorption bands width can be considerably narrowed in the TiO_2 as compared to microstructures TiO_2 as a result of quantum confinement in TiO_2.

Table 1.1: Application based reseach work carried out on TiO_2 .

Features	**Application**	**Reference**
High refractive index	Pigment in paints, coatings and polymers (as powder)	[40, 46-50].
Band gap in UV range	UV blocker in sunscreen	[51-58]
Nanocrystalline TiO_2 having electrochromic nature.	Smart windows/ mirrors	[53, 54, 59-61]
Addition of dye molecules in TiO_2	Dye sensitized solar cells	[62-69]
Doping of metals 1.SnO_2 in TiO_2 2.Pb in TiO_2	Varistor	 [70] [71]
Improvement in conductivity in Gas environment.	Gas sensor for 1. O_2 2. CO, 3. NO_2 and 4. H_2.	 1.[72, 73], 2.[21, 74, 75] 3.[75] 4.[66, 76-79]
Control of electronic structure of TiO_2/ SnO_2 stacked layers.	Photocatalysis	[80, 81]

1.2.2 **Germanium**

Si and Germanium are the inventory semiconductors (4^{th} group elements) but commercial Si research is 10 times higher than Ge reported in last 30 years. Although Ge has some promising properties like high 'refractive index', 'mobility' and small 'effective mass' but substantial focus on Si is paid due to its easy processing as compared to Ge. Inverse band gap of Ge has been an additional reason for not being considered in semiconductor processing at micro. Ge has attracted the nano-research community due to a relatively higher 'Bohr magnetron radius'~ 25 nm. Therefore 'QCE' in Ge is observed when any one dimension is $\leq$ 25 nm to be exploited in tunable optoelectronic materials [82-84]. Due to this exciting feature, Ge has replaced Si at nanoscale fabrication of 'transistors' [85-87], 'photo-voltaic devices' [88-90], 'longer wavelength photo-detectors' [91], 'bio-detection devices' [92, 93] and 'non-volatile memories' [94-96].Ge nanowires exhibiting 'QCE' have been observed to show improved electrical properties [97]. Thin films of Ge deposited on Si substrate (annealed upto 550°C) have been observed to show field emission properties [98].

'QCE' in Ge nano-films (crystallite size ~ 1.2 nm) resulted in conduction band shifting upto 1.1 eV[99]. Blue shifting in absorption edge was reported as an outcome of reduction in film thickness (200-5 nm). Decrease in thickness and crystallite size are in direct correlation such that crystallite size << film thickness [100]. Chemical etching of these films produced nano-porous crystallites exhibiting photoluminescence (PL) around 1.55 eV possibly due to exciton generation. [101]. Whereas PL observed in laser induced etching of nano-crystallites (size ~ few nanometers) has been attributed to phononic confinement [102].

Direct bandgap related to Ge (0.8 eV) is compatible to indirect band gap of Si (1.1 eV), therefore scientific study has been conducted on Ge related to on-chip communications technology [103]. Direct band gap of Ge has resulted in electroluminescence in bulk [104], 'quantum dots' [105] and 'quantum well' [106].Ge NC's demonstrated 'QCE' in GeO_2 layer was observed through their PL and Raman spectra [107]. Similar behaviour was observed in Ge NC's embedded into TiO_2 films [108, 109], by controlling their size for photovoltaic cells [1, 110].

Ge has been observed to show properties related to multiple applications given below:

1. High diffusivity of Au in Ge has made Ge/Au films to be used in rewritable DVD's [111].
2. High resistivity in Ge with SiO has been exploited in 'thermal imaging cameras' .
3. Ge is used in 'optical fibers' [112-117] and wire free devices [118-120].

1.2.3 Titania-Germanium (TiO_2-Ge) composite

Composite nano-films of TiO_2-Ge were initially speculated by Sukti Chatterjee [109] as one amongst the next generation thermoelectric materials. A uniform distribution of Ge nanodots (size ~ 5nm) in TiO_2 were found to be responsible for increase in efficiency. In another experiment by this group [108] nanocomposite films of TiO_2- Ge were fabricated by composite targets sputtering RF magnetron setup. Films having three different Ge concentrations i.e. 33%, 15% and 9% by weight % were studied and films with minimum Ge concentration exhibited highest photoresponse among three samples. Increase in band gap (from UV to NIR) was observed in annealed films

obtained by successive deposition of TiO_2 (6.8 nm) and Ge (0.99 nm) layers on quartz substrate [121].

Stacked layers of Ge and TiO_2 (~ 20 nm) deposited on BK7 glass in such a way that Ge film thickness in each sand-witched layer was increased by 2nm from the previous Ge layer; initial Ge layer thickness being 2nm [122]. In total 11 layers of TiO_2 and 10 layers of Ge were deposited onto each other. Post deposition heat treatment (for 2 Hrs) at 200°C, 400°C, 450°C and 500°C was observed to increase in absorption transitions. Multiple transitions observed in films annealed at 450°C and 500°C were attributed to 'QCE' in Ge.

A. Slav et al [123] investigated 'QCE' in Ge-TiO_2 films for their potential application in photovoltaics. Effect of deposition conditions was studied by employing three different reactive gas concentration (2, 4 and 6% oxygen) resulting in 3, 22 and 35 % of Ge in TiO_2 matrix.in different concentrations. It was found that films containing 22% Ge had maximum optical absorption with band gap around 3.6 eV. Another experiment was performed by him on TiO_2 and Ge composite nano films with different concentration of both components grown on fused silica and Si [2]. TiO_2 : Ge % concentration ratio in three different samples was 97%:3%, 78%:22% and 65%:35%. It was observed that increase in Ge contents results in increase of indirect band gap, which means number of free carriers increases. Doping of nickel, zinc [124], tungsten [125], Sn [126], Cr, Al and Ni [4] nanoparticles in TiO_2 is reported to improve PV response of whole material.

1.3 Fundamentals of Film Growth

Thin film growth is a complex process as it involves nucleation of deposited material on substrate along with various phase transformations. Formation of various nanostructures and crystallinity of thin films depends on nucleation process. Thin film deposition process in nano regime is very dependent on initial nucleation process; which thus by effects the Gibbs free energy [127]. One of the main aspect of initial nuclei to effect Gibbs free energy volume is their shape and size. This change in Gibbs free energy is a net effect caused by 'supersaturation' and energies (surface and interface) as explained through Young's equation [128]. No other considerable interactions exist between the substrate and film. Initial nucleation leading to film

growth is effected by substrate and film interaction [129] and hence promote film growth governed by nucleation modes given below:

1. Island or Volmer-Weber growth (V-W growth)
2. Layer or Frank-van der Merwe growth (F-M growth)
3. Island-layer or Stranski-Krastonov growth (S-K growth)

Figure 1.1 demonstrates the above mentioned modes of initial nucleation for film growth. If cohesive forces among deposited species are stronger than adhesive forces between substrate and deposited species then Island growth is favoured.

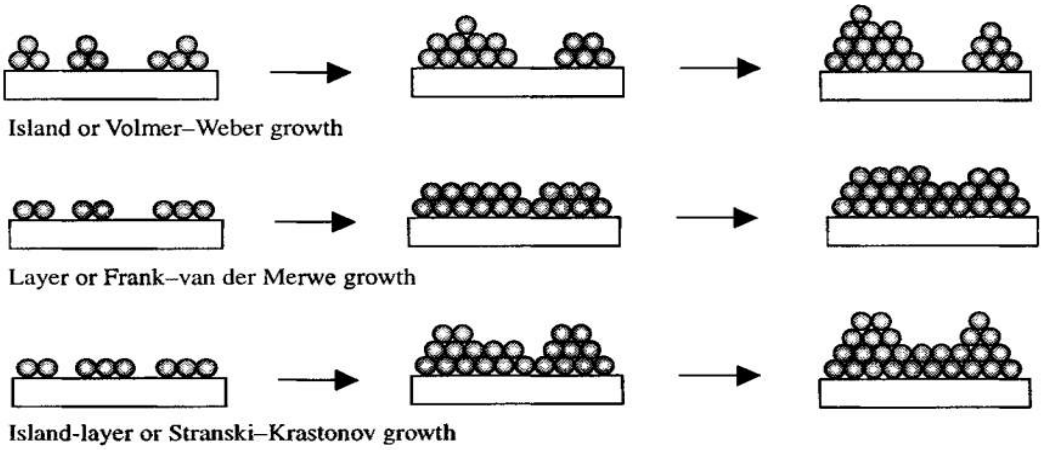

Figure 1.1: An illustration of growth mechanisms for island, layer and island-layer growth mode on substrate.

So metallic layer on insulator, graphite, alkali halides and mica substrates follow this type of nucleation and finally islands coalesce forming a film.

Layer growth mode is governed by opposite behaviour of deposited species and substrate as observed in island growth mode [130] which manifests film growth of single crystal. Combination of V-W and F-M growth mode results in island-layer growth which gives rise to stress simultaneously forming nuclei and films [128, 131, 132].

Nucleation process can be categorized into two types

- Homogeneous nucleation (condensation of same phase on seed)
- Heterogeneous nucleation (seed and condensing atoms/ molecules are of different phase)

Thin film deposition process can be studied by considering the process as heterogeneous nucleation taking place on a planar solid substrate. Development of a different phase at the surface of some other material is called 'heterogeneous nucleation' [129].

Here we assume that substrate surface is being impinged by growth species (vapour phase) which then diffuse and accumulate forming cap shaped nucleus as explained in Fig.1.2.

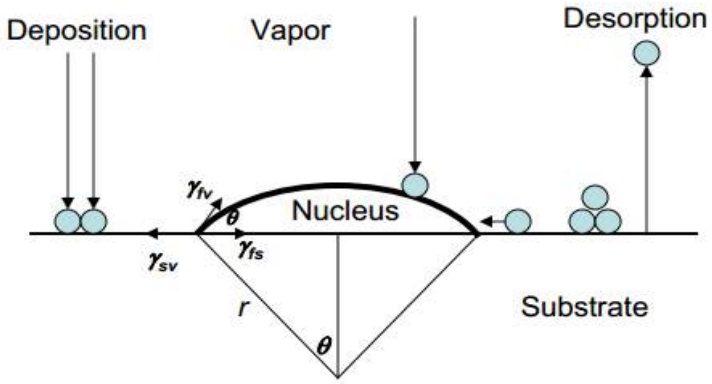

Figure 1.2: Thin film growth mechanism as an effect of surface and interface energies of substrate, deposit and film.

In Fig. 1.2 γ_{fv}, γ_{fs} and γ_{sv} are the surface or interface energy of 'vapour-nucleus', 'nucleus-substrate' and 'substrate-vapour' interfaces. Gibbs free energy for nucleation is given by Eq. 1.1 [128]

$$\Delta G = a_3 r^3 \Delta\mu_v + a_1 r^2 \gamma_{fv} + a_2 r^2 \gamma_{fs} - a_2 r^2 \gamma_{sv} \qquad 1.1$$

Where r is the 'average diameter' of nucleus, $\Delta\mu_v$ is the change in 'Gibbs free energy per unit volume' and ***'a_1', 'a_2'*** and ***'a_3'*** are constants related to nucleus geometry given by [128]

$$a_1 = 2\pi\,(1 - cos\theta) \qquad 1.2$$

$$a_2 = \pi\, sin^2\theta \qquad 1.3$$

$$a_3 = 3\pi\,(2 - 3\,cos\theta + cos^2\theta) \qquad 1.4$$

where θ = 'contact angle' (it depends on the surface and interface) explained by Young's equation:

$$\gamma_{sv} = \gamma_{fs} + \gamma_{fv} cos\theta \qquad 1.5$$

Gibbs free energy of new phase has an inverse relationship with total 'surface energy' and nucleus stability increases if its size becomes larger than a 'critical size', r^*.

$$r^* = \frac{2\pi\gamma_{fv}}{\Delta G_v}\left\{\frac{sin^2\theta.cos\,\theta+2cos\theta-2}{2-3cos\theta+cos^3\theta}\right\} \qquad 1.6$$

$$\Delta G_h^* = \left\{\frac{16\pi\gamma_{fv}}{3(\Delta G_v)^2}\right\}\left\{\frac{2-3cos\theta+cos^3\theta}{4}\right\} \qquad 1.7$$

Where, $\Delta G_H^* = \frac{16\pi\gamma_{fv}}{3(\Delta G_v)^2}$ = Threshold energy for 'homogeneous nucleation' and 2nd term is wetting factor which depends on θ. Therefore thin film growth will depend on contact angle so [128, 133]

- If θ = 180° wetting factor is 1, hetrogeneous barrier would be equal to homogeneous nucleation as shown in equation? Also Young's equation can be represented by

  $$\gamma_{sv} = \gamma_{fs} - \gamma_{fv} \qquad 1.8$$

  In such a case vapour will not be deposited on the substrate and homogeneous nucleation of vapours will be favoured.
- If 0<θ < 180°

  Here,Energy barrier for

  'Heterogenous nucleation' < 'Homogeneous nucleation'

  Therefore thin film will be grown on the substrate. For θ>0°. Young's equation will be written as

  $$\gamma_{sv} < \gamma_{fs} + \gamma_{fv} \qquad 1.9$$

  Such a situation will favour island growth so quantum dots and/or nanoparticles will be synthesized on substrate
- If θ = 0° wetting factor < 1 then there will be no energy barrier for heterogeneous nucleation, it is the only case when the deposit and substrate are of same material and young equation becomes

  $$\gamma_{sv} = \gamma_{fs} + \gamma_{fv} \qquad 1.10$$

Single crystal growth is one of the important layer growth mechanism obtained through homo-epitaxy or hetro-epitaxy. In both the cases there is no or small difference between the lattice parameters of substrate and depositing material. Homoepitaxial layer can be considered as an extension of substrate due to non-existence of interference. Growth

species are adsorbed/ absorbed after condensation on substrate although chemical composition of deposit and substrate are different, therefore the thin films will have different lattice constants from substrate. This difference can develop stresses which is the reason for the S-K growth. In situ development of stresses makes S-K growth mode a complicated process which initially starts from layer growth then stresses arise due to the lattice mismatch. Further layer growth results in an increase in stresses and hence strain energy. Strain energy increases with the increase in deposit volume in the absence of plastic deformation/ relaxation[133]. These stresses are therefore responsible for modification in many physical properties like optical [134], electrical and optoelectronic response [129].

Therefore Gibbs free energy for heterogeneous nucleation (ΔG_h^*) calculated in Eq. 1.7 will include strain energy (ω) per unit volume as shown below [128]

$$\Delta \boldsymbol{G_h^*} = \left\{\frac{\boldsymbol{16\pi\gamma_{fv}}}{\boldsymbol{3(\Delta G_v+\omega)^2}}\right\}\left\{\frac{\boldsymbol{2-3cos\theta+cos^3\theta}}{\boldsymbol{4}}\right\} \qquad \textbf{1.11}$$

As ΔG_v is negative and ω is positive the nucleation energy increases as compared to the case when there is no stress in thin film. As stress increases ΔG_h^* decreases and there is a critical limit when $\omega >> \gamma_{fv}$ beyond which ω cannot further increase, Gibbs free energy (ΔG_h^*) reaches to minimum value. Under such condition nucleation takes place on already deposited layer. Therefore, 'Surface energy' of substrate surpasses combined effect of deposit 'surface energy' and 'interface energy' [128, 135]

$$\boldsymbol{\gamma_{sv} < \gamma_{fs} + \gamma_{fv}} \qquad \textbf{1.12}$$

Volume of Gibbs free energy is also changed by [128, 135]

- Generation of 'screw dislocations' due to nucleation at cleavage steps and hence release stress from film.
- Impurities and substrate charge affect the ΔG_h^* by the change in surface 'electrostatic energy' & 'chemical potential'.

The above-mentioned models and mechanisms explain amorphous, polycrystalline, single crystal organic, inorganic and hybrid deposition process. Crystallinity of thin film depends on various growth conditions like impinging rate of deposit material, deposition temperature [127]. Some growth parameters of single, poly-crystalline & amorphous films are mentioned below:

a. Single crystal films growth requires [127, 136]:

i. Substrate (Single crystal) having no or low lattice mismatch with the deposit.

ii. Contamination/ impurity free substrate surface in order to prevent secondary nucleation.

iii. High substrate temperature so as to gain mobility enough to grow film.

iv. Low transfer rate of deposit in order to gain adequate time for diffusion and absorption of deposit into crystal structure necessary for structural relaxation to proceed further deposition.

b. Growth of amorphous films is possible when [127]:

i. Ambient temperature is low so that growth species may not have surface mobility to form larger crystals.

ii. Deposit influx is too high so that growth species may not have as much time to grow on lowest energy sites.

c. Polycrystalline film growth conditions fall between those of amorphous film deposition and single crystal growth [127].

Generally deposition is carried out at moderate temperature while influx of growth species is high. Low growth temperature results in hyper-abrupt surface with 2 or 3-dim nanostructures called quantum platelets or quantum dots [128]. Impurities & additive complicate the growth process to grow multi-component films. Overlying of single crystal on crystalline (Single) substrate or seed is acquainted as epitaxy. Epitaxial growth can be further divided into two types [127]

a) Homoepitaxy

This type of growth is achieved when both substrate and film are of same material and there is no lattice mismatch between substrate and film. Therefore, better quality film growth is achieved or to introduce dopants into the grown film.

b) Heteroepitaxy

When a dissimilar material is grown on substrate it is referred as heteroepitaxy. Another important thing is that there exists a mismatch (misfit factor; f) between grown material & substrate, which is given by [127, 128, 137]:

$$f = \frac{a_f - a_s}{a_f} \qquad \textbf{1.13}$$

where a= lattice constant and subscripts s & f stand for substrate and film. If

$f > 0$, strain → tension, and

$f < 0$, strain → compression.

Strain energy and film thickness are directly co-related. Strain and relaxation in films depend on the value of f [127] i.e. if it is

- small ⇒ smaller dislocations ⇒ strained films
- large ⇒ larger dislocations ⇒ relaxed films

Schematic illustration of lattice orientation among homo and hetroepitaxial structures is shown in Fig. 1.3

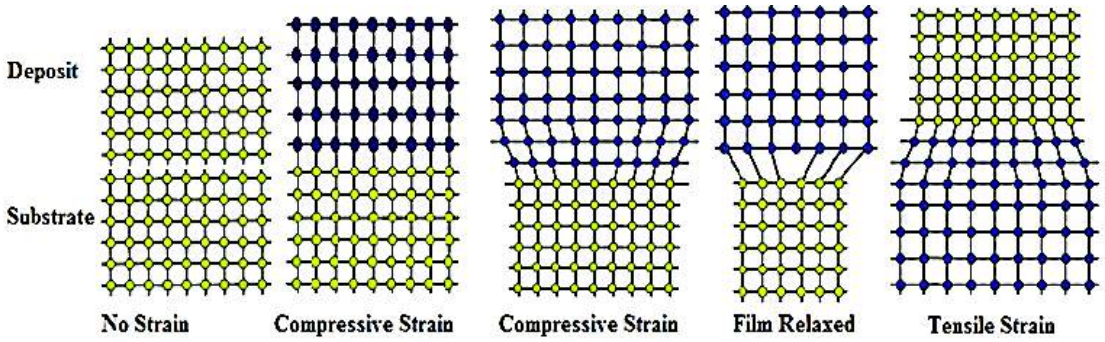

Figure 1.3: Unstrained, relaxed and strained film growths depending on compressive, tensile strain, dislocation or lattice misfit factor.

There is a critical thickness (t_c) of film beyond which the defects are introduced in film which is given in equation as follows [129]:

$$t_c = \frac{a_f^2}{2\,(a_f - a_s)} \qquad 1.14$$

In order to grow defect free films thin film thickness should be smaller as compared to critical thickness. Therefore thin film thickness plays a vital role in its electronic, optical & electrical properties of films. Being well-established growth techniques (homo and heteroepitaxial growth) have wide spread applications (specifically in electronic industry) [23, 138].

1.4 Pulsed Laser Deposition (PLD)

High quality multicomponent thin films can be deposited through pulsed laser deposition process by ablating target upon impinging laser beam [5, 139]. Ablated particles from target create a film by condensation on substrate (placed opposite to the

target) [140].

PLD being "physical vapor deposition process" has deliberate usage because of exhibiting similar properties related to "Molecular Beam Epitaxy" (MBE) and "sputter deposition process" [132]. PLD process is schematized in Fig. 1.4. In this technique high fluence pulsed laser-beam of nanoseconds pulse width is engrossed on a target to ablate, [5] its infinitesimal part establishing plume in the form of material flux for film growth [141]. This plume expands conically forming film on substrate [5]. Material is rapidly heated to a very high temperature, introducing stress waves of high amplitude in solid target accompanied by phase transitions. Absorption of this high energy in material boils it off which then expands out in gas phase [142].

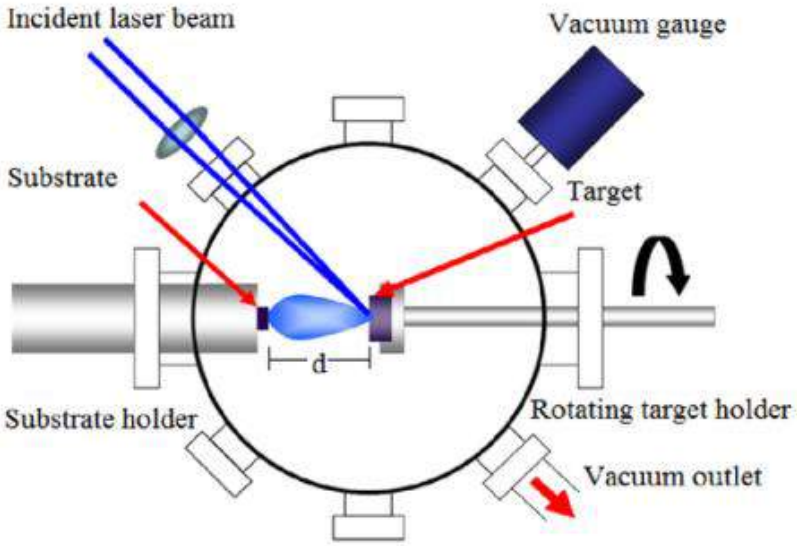

Figure 1.4: Pulsed Laser Deposition process going on in deposition chamber as a result of target ablated by incident laser beam and thin film is deposited at substrate kept at a distance d from target.

Epitaxy in inorganic materials (specifically multi-constituent) can be achieved by 'PLD' with high efficiency. Epitaxy of thin film depends on various factors like laser fluence, target density, target-substrate separation (indicated as "**d**" in Fig 1.4), ambient pressure, focal size etc.

Ablation efficiency is influenced by optical absorption coefficient of target, Laser fluence is the controlling factor for evaporation flux [132, 141]. If

Laser fluence < ablation threshold ⇒heating of target

Laser fluence > ablation threshold ⇒plume generation

Factors affecting the laser fluence are:

- Irradiance spot size.
- Laser frequency (2nd, 3rd and 4th harmonic)[132]
- Target density
    - High density ⇒ epitaxial growth
    - Low density targets ⇒ particulate growth [140, 143])

These factors also influence the deposition rate, which are explained later in this section [132].Atom ejection rate from the target directly depends on the density of target if target density is low then atom ejection rate would be slow, then the particles will undergo collisions free expansion, but if the target density is high then some of the atoms will collide and they will be scattered back into the target. This back scattering in multicomponent target may induce secondary sputtering thus by effecting the stoichiometry of target [144, 145]. This phenomena is basically dependent on the ionic mass (M) of ablated species, and their deceleration rate at a certain point in deposition chamber as explained by Singh and co-workers [146, 147]. This phenomena is explained in terms of spatial co-ordinates x, y and z of plume, time (t), plasma temperature (T_o) and mass of ionic species. Mathematical representation of this phenomena is explained by equation 1.15:

$$\boldsymbol{x\,(t)\left[\frac{1}{t}\frac{dx}{dt}+\frac{d^2x}{dt^2}\right]=y\,(t)\left[\frac{1}{t}\frac{dy}{dt}+\frac{d^2y}{dt^2}\right]=z\,(t)\left[\frac{1}{t}\frac{dz}{dt}+\frac{d^2z}{dt^2}\right]=\frac{RT_o}{M}} \qquad \boldsymbol{1.15}$$

Therefore in a multicomponent target the ionic species are ejected out depending on their absorption threshold but their density at a certain point is dependent on their deceleration rate. So the species with a smaller ablation threshold will be ejected out with higher velocity but their concentration will decrease as an inverse of their ionic mass. So materials with higher ablation threshold but with a smaller ionic mass will have smaller decrease in their density at a larger distance from the point of ablation.

Target-substrate separation variation can affect various features of laser-assisted deposited films. The properties which have been reported to be effected by target-substrate distance are structural properties and reflectivity [148], band gap [149], photoluminescence [150], surface roughness [129] and growth of various nanostructures [151].

Second main factor which effects thin film quality is the vacuum level. Mostly thin film deposition and all of the characterizations are carried out in vacuum. Ambient pressure

(P), temperature (T) and mean free path (λ_{mfp}) are some of inter-related parameters to understand the various processes undergoing during deposition or characterization under vacuum [152]. Mean free path is related to gas-pressure, given by [128] :

$$\boldsymbol{\lambda_{mfp} = \frac{5\times10^{-3}}{P}} \qquad \textbf{1.16}$$

At high pressure mean free path is too small to have high number of collisions in gas-molecules and at low pressure mean free path is smaller so gas molecules have smaller collision cross section. If the gas pressure < 10^{-3} torr; gaseous species have a much higher collision cross section so they collide to chamber walls prohibiting inter-molecular collision [153].

As well as thin film deposition rate in evaporation condensation, sputtering or PLD depends on both vacuum and plasma. Deposit is in gas phase during deposition therefore thin film growth rate depends on the gas molecules impinging rate (φ) on the substrate. Impinging rate is number of growth molecules in unit time per unit area and it can be calculated as [127]

$$\boldsymbol{\varphi = \frac{3.5\times10^{22}P}{(MT)^2}} \qquad \textbf{1.17}$$

Where M is the molecular weight of growth species.

Figure 1.5 exhibits the molecular, transition and viscous flow regimes for gases at various pressures. It is clear for a small dimension molecular flow can be achieved at a lower vacuum but for larger dimension the case is opposite.

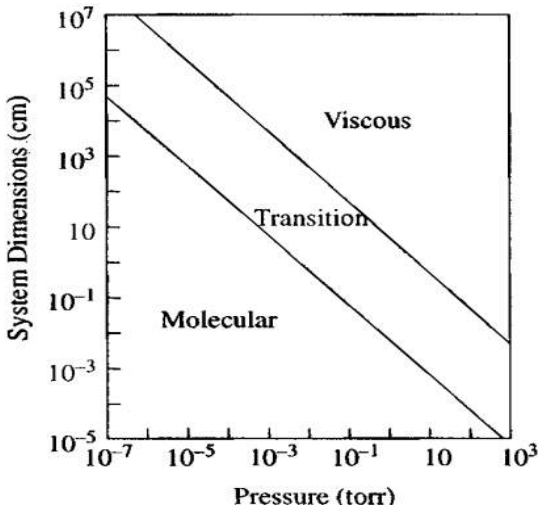

Figure 1.5: Various modes of gas flow and their dependance on system dimension (cm) and pressure.

Different processes can be carried out under various vacuum regimes [128] mentioned

below

- Medium to high vacuum → sputtering and low pressure CVD
- High to ultrahigh vacuum → film deposition and evaporation
- Ultrahigh vacuum → analytical appliances (SEM, TEM, PL, Raman etc.) are operational [154].

Gas flow is integrated in molecular (1st regime), intermediate (2nd regime) & viscous (3rd regime) [127]. Gas flow depends on magnitude of the "Knudsen number", K_n given by [152]:

$$K_n = \frac{D}{\lambda_{mfp}} \qquad 1.18$$

The table below explains the various regimes of gas flow

Table 1.2: Various gas flow regimes with reference to Knudsen number and D.P; D is the characteristic dimension of system and P is pressure

Gas flow Regimes	Knudsen number	D.P (cm. torr)
Molecular flow	$K_n < 1$	$D.P < 5\times10^{-3}$
Intermediate flow	$1 < K_n < 110$	$5\times10^{-3} < D.P < 5\times10^{-1}$
Viscous flow	$K_n > 110$	$D.P < 5\times10^{-1}$

Ion-energy distribution is essential aspect of PLD to effect morphology of films as interstitial stress (compressive) are developed by energetic "ion- implantation" [132, 140, 155]. Interaction of ion species with substrate in PLD is shown in Fig. 1.6.

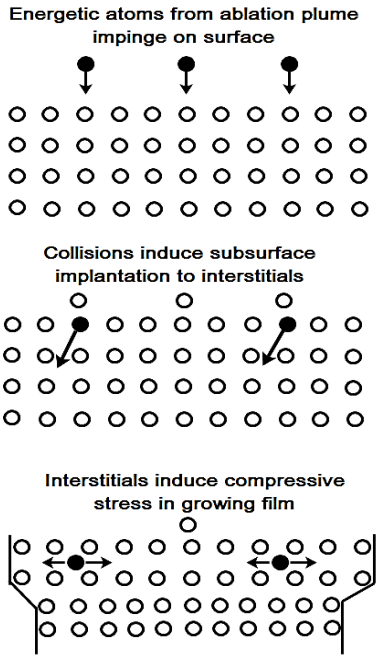

Figure 1.6 : Interaction of ion species with substrate in PLD.

High laser energy ascertains the removal of larger particles (~μm) from target

influencing single and multilayer epitaxy of film [139, 143]. To avoid larger particulates targets of high density are prepared therefore nano-size of particulates can be achieved during "PLD"[132]

Various nanostructures like nanowires, NC's and nanocomposites of photonic interest have been fabricated through "PLD" [156]. Many aspects make it advantageous in film research regime [140, 148] because :

a. It has a very high deposition efficiency (~ 70%), additionally it is simple and a quick method for nanostructures growth with stichiometry control thus by making it preferred industrial nanostructure material manufacturing means

b. Thickness variation creates strain in film which provides a control on modification, explicitly in structural, magnetic, electrical, optical properties of materials.

PLD provides a control on particle size and in semiconductors to quantum size thus by improving semiconducting properties [151].

1.5 Characterization Techniques

In this section brief introduction has been given about the analytical tools that were used in the present studies.

1.5.1 X-Ray Diffraction (XRD)

XRay diffraction (XRD) is a useful technique [128] to study the details of crystalline structure: including material identification, crystal orientation, lattice constants, strains, defects, geometry and identification of unknown materials as impurities, dopants, additives etc. Schematic of XRD has displayed in Fig. 1.7.

Usually a collimated X-Ray beam of wavelength 0.7 -2 A° directed on the sample is diffracted by the crystalline structure which can be explained by Bragg's law as

$$n\lambda = 2d \sin\theta \qquad 1.19$$

where

n= order of diffraction i.e. 1, 2, 3.

d= Inter-planer spacing

λ= Wavelength of Cu Kα X-rays

θ= Diffraction angle

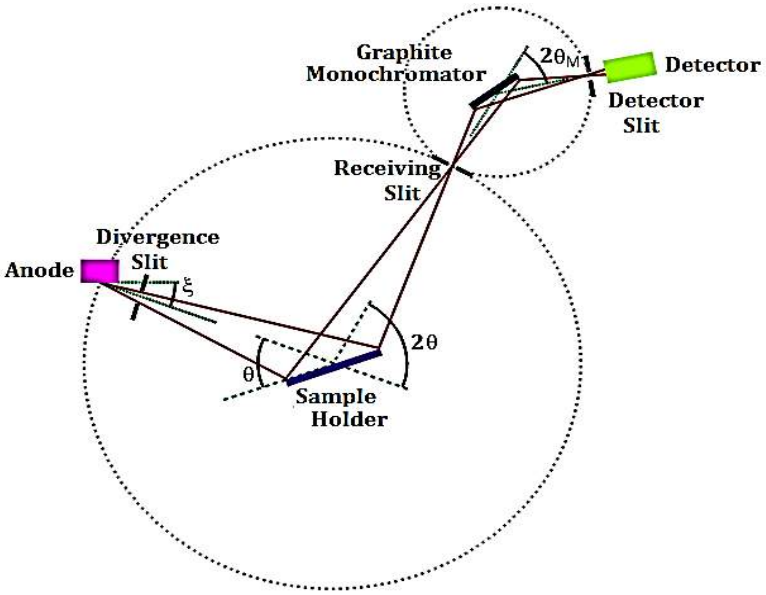

Figure 1.7 : Block Diagram of XRD [157].

Diffractogram obtained is an intensity plot as a function of 'diffraction angle' 2θ and/ or specimen's orientation. This obtained spectrum is helpful in identifying all the above mentioned properties

Accurate peak position determination gives an opportunity to the measure strains [128] either homogeneous/ inhomogeneous, , Mathematically strains are calculated by Williamson and Hall equation [158] as shown below

$$\frac{\beta cos\theta}{\lambda} = \frac{1}{\varepsilon} + \eta \frac{sin\theta}{\lambda} \qquad 1.20$$

Homogeneous strain are directly proportional to the change in the lattice constants and hence d spacing, observed as peak shifting, whereas inhomogeneous strains can arise in different or same crystallite which turn up as peak broadening as a function of Sinθ (in eq 1). The 'strain' (ε) obtained from 'peak broadening slope' (β$Cos\theta$) and $\sin\theta$ using the equation [4]

$$\beta = \frac{\lambda}{DCos\theta} - \varepsilon\, tan\theta \qquad 1.21$$

'Dislocation density' (δ) which is in fact the number of dislocations per unit length of dislocation lines of the crystal, was evaluated using [159, 160] formula

$$\delta = \frac{1}{D^2} \qquad 1.22$$

Peak broadening is also observed when particle size is very small; which is not dependent on sinθ quiet opposite to the behaviour observed in strained structures. So peak broadening can be very helpful in identifying the physical feature like decrease in particle size or inhomogeneous strain. Therefore crystallite size free of inhomogeneous strain can be estimated through Scherrer's formula which is given below:

$$\boldsymbol{D = \frac{K\lambda}{\beta \cos\theta}} \qquad \textbf{1.23}$$

where

K= Scherrer's constant / shape constant = 0.94,

λ= Wavelength of Cu K_α X-rays,

θ= Diffraction angle (degrees) and

β= FWHM of a diffraction peak (Radians),

Scherrer's formula may not give similar results for different structures of same material. A suitable amount of material is required for observable statistics to get information about crystallite size/ nanoparticle. Therefore, in case of nano-films feasible signal cannot be generated so slower scan rate is adopted to obtain appropriate results [161].Another important aspect observed in XRD is that materials with high Z show intense diffraction peaks as compared to small Z materials.One of the advantage of XRD is that it is non-destructive and sample preparation is easy [162].

1.5.2 **Raman Spectroscopy**

Visible mono chromatic light source (Laser) is incident on sample to obtain Raman spectra [160]. Earlier investigation employed mercury arc lamp as a source which has been replaced by various Laser sources. Scattered radiation spectrum is recorded by means of compatible visible spectrophotometer particularly at 90°. Raman intensity is 0.01% of source which may cause experimental error in detection & measurement. Shifting of Raman spectral lines towards longer wavelength (lower energy) and shorter wavelength (higher energies) are called Stoke and Anti-Stoke shifts. Intensities of anti-stoke lines are weaker than those of stokes. It is a powerful analytical tool to determine specific molecules by recording and identifying the spectrum of their vibrations. Generally wave number shift vs source line are being plotted in Raman spectrum. Wave number in terms of strokes peaks, can be calculated as

$$\Delta\sigma = \sigma_s - \sigma \qquad 1.24$$

Where σ_s is the wavenumber (in cm^{-1}) of particular source line and σ is the wavenumber of observed Raman peaks.

Raman intensity is proportional to the quantity of active specie. The intensity/ power of the Raman peak is four times higher as compared to the intensity/ power of the exciting source.

The instrumental setup [163] embodies three constituents i.e.

- Intense source; Helium/neon laser is most probably used as source at 50 mW.
- Sample illumination system; It records the wavenumber shift between two visible frequencies. Additionally samples of small dimensions can be scanned as the source is confined to small area.
- Spectrophotometer; It is incorporated with photomultipliers to record peak intensities. To reduce the noise two mono-chromators are employed and split beam design is included to compensate the fluctuations in source intensity [164].

The schematic diagram of a Raman setup is shown in Fig. 1.8.

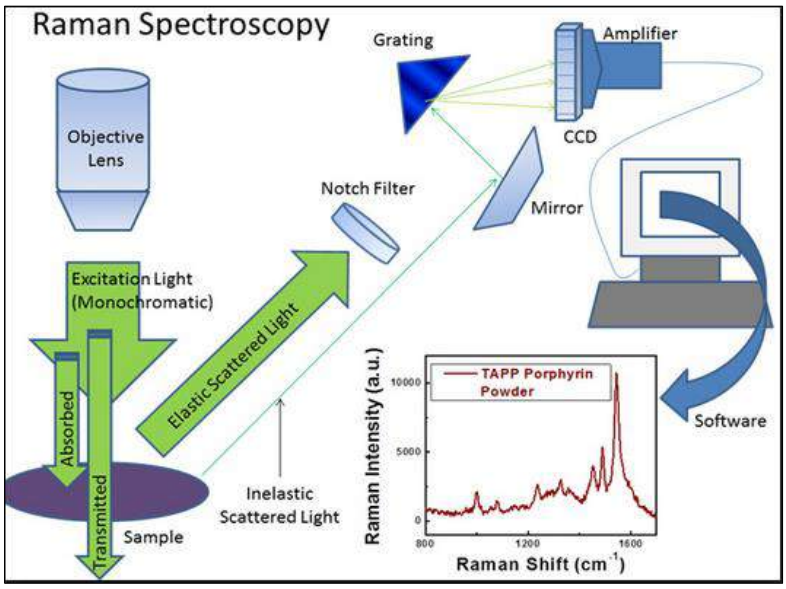

Figure 1.8 : Schematic diagram of Raman spectroscopy [165].

Raman studies are simple since they assess wavenumber differences among two visible frequencies. Metal associated bonds usually lie in the range 100- 700 cm^{-1} so most of such compounds are recognized in this range. Raman studies give information related

to structure and composition [166] as the various bonds show vibration in various wavenumber regime. Therefore, composites and dopants can be distinguished through this technique.

1.5.3 Energy dispersive X-Ray spectroscopy

In an energy dispersive X-Ray spectroscopy (EDX), electron beam incident on sample produces continuous and characteristic X-Rays [154, 167]. Continuous (background) X-rays appear in baseline of EDX whereas characteristic X-Ray peaks related to K_α K_β appear around respective energy range in energy Vs intensity plot. These collected X-Ray signals are detected by computer and transformed into peak by aided software which labels peaks by identifying constituent elements as shown in Fig. 1.9 [168]. A good peak to background ratio is needed for proper identification of characteristic peaks.

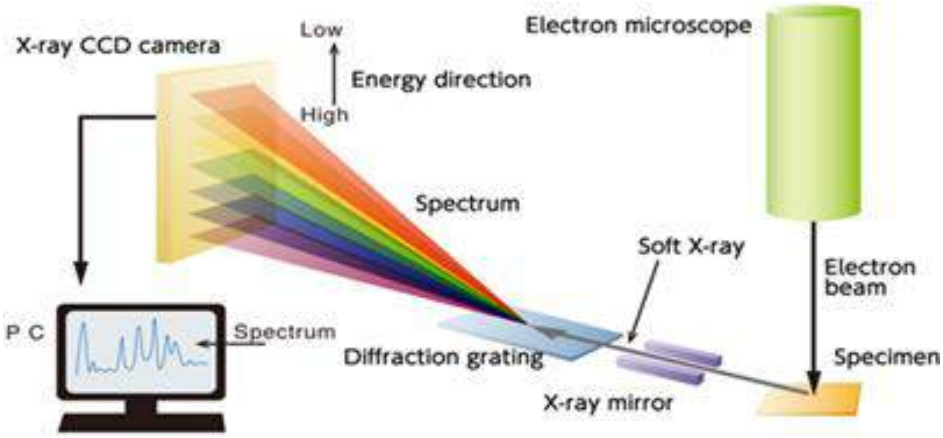

Figure 1.9: Illustration of EDX [155].

1.5.4 Ultra Violet Visible (UV/Vis) Spectroscopy

This tool is used to study electronic properties of material by means of optical properties [169]. Incident radiations either absorb, reflect, transmit, cause fluorescence etc. upon interaction with specimen [170]. Each material shows different optical properties i.e. transparency of materials is different for each material. Beam design for UV-Vis spectrometer is given in Fig. 1.10. UV-Vis spectrometers usually record transmission or absorption and rarely reflectance spectrum from specimen [169].

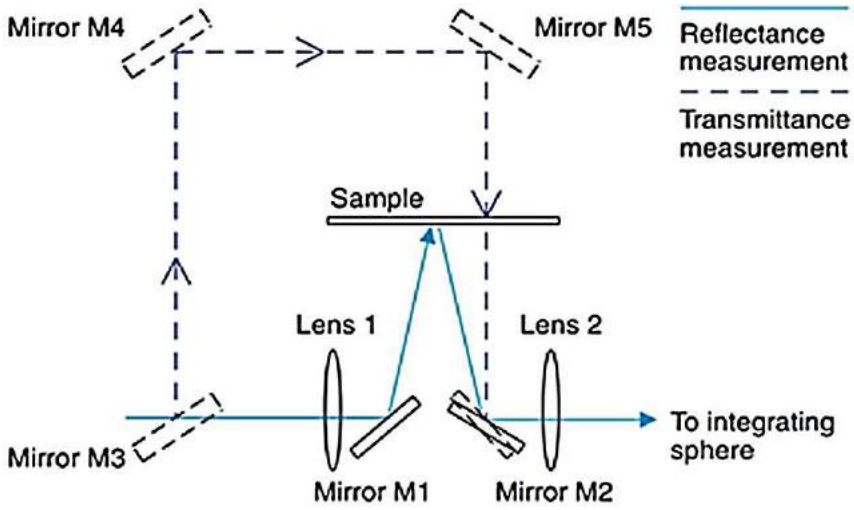

Figure 1.10: Beam design of UV-Vis spectrophotometer in transmittance and reflectance mode [171].

In UV Vis reflectance spectroscopy reflected light from a sample or thin film is obtained as absolute reflectance (R). This reflectance is then used to calculate absorbance "F(R)" through Kubelka Munk relation which is given [172] as follows

$$F(R) = \frac{(1-R)^2}{2R} = \frac{K}{S} \qquad 1.25$$

Where R is reflectance recorded for films. Kubelka-Munk absorption(k) and scattering (S) constants which is proportional to absorption and reflectance transitions in this thin film [172]. Mostly absorption from coloured materials lies in visible spectrum [173].

"Band gap" of a material is calculated by Tauc equation [174] which clearly explains the association between absorption and bandgap (E_g) of material given by equation below

$$\alpha h\upsilon = B\left(h\upsilon - E_g\right)^n \qquad 1.26$$

"B" basically determines the transition probabilities (almost constant), and n in above equation can have any value from $^1/_2, 2, ^3/_2$ or 3 depending on transition type.

1.5.5 **Ellipsometry**

It is a versatile approach employed to measure thickness & optical parameters like refractive index "n", dielectric constant "$\mathcal{E}_1$", extinction coefficient "k", and dielectric loss "$\mathcal{E}_2$" [165]. Although thickness measurement is not a direct procedure rather other optical properties are measured through which thickness is measured. Linearly

polarized light is incident on the sample surface making an angle to its surface and reflected light signal is recoded is shown in Fig. 1.11.

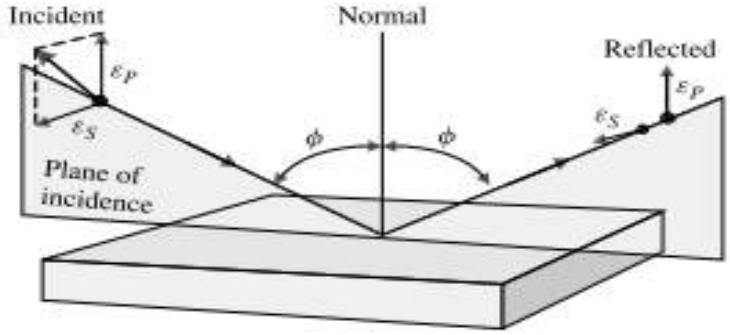

Figure 1.11: Schematic of light reflection from sample surface.

Difference in amplitude and phase shift is further processed to find the above mentioned properties of material. Since measurement involves angle measurement therefore variables measurement is more precise [138].

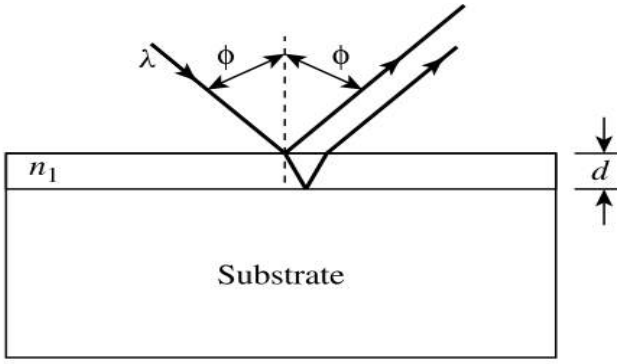

Figure 1.12: Reflection from the surface of film and interface.

Ellipsometry is considered as the most appropriate technique for the films with k=0 grown on semiconductor substrates [175]. Fig. 1.12 illustrates layer-on-substrate in which interfering reflected rays are in phase. These interferences are useful in thin film determination as mentioned in equation stated below [138].

$$\boldsymbol{d = \frac{\lambda}{2\sqrt{n_1^2 - sin^2\phi}}} \qquad \textbf{1.27}$$

1.5.6 **Photoluminescence (PL)**

It is one among the non-destructive method to analyze impurities in some materials (with poor radiative efficiency, low-quality indirect bandgaps) and semiconductors [176]. Deep and shallow level impurities can also be located provided they exhibit

radiative recombination [177], but their density cannot be measured. It can also be used to find the defects and doping in the materials.

The experimental setup consists of an excitation source, sample bench and detector as shown in Fig. 1.13.

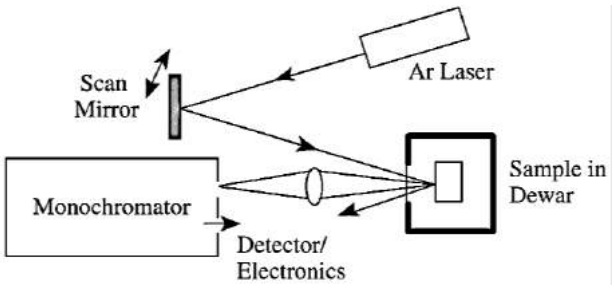

Figure 1.13: Schematic showing photoluminescence.

Optical excitation is carried out through a laser source having energy $h\nu > E_g$ (ν = Laser frequency) as a consequence electron holes are generated which recombine through radiative, non-radiative or surface recombinations. But only radiative recombinations are detected as mentioned earlier.

Maximum light intensity is ensured by an appropriate optic arrangement, excitation source wavelength can be varied by tuning it through dye laser. In PL absorption depth of the excitation source is ~ 10^{-6} m which can be reduced by using excitation source in UV range.

1.5.7 **I-V Measurements**

There are two most extensive methods to determine electrical resistance of materials i.e. two-point and four-point probe. It is comparatively easy to implement two-point probe method which requires two points of contact. Arrangement of "*two-point probe method"* is given Fig. 1.14 where each contact serves for *current* and *voltage.*

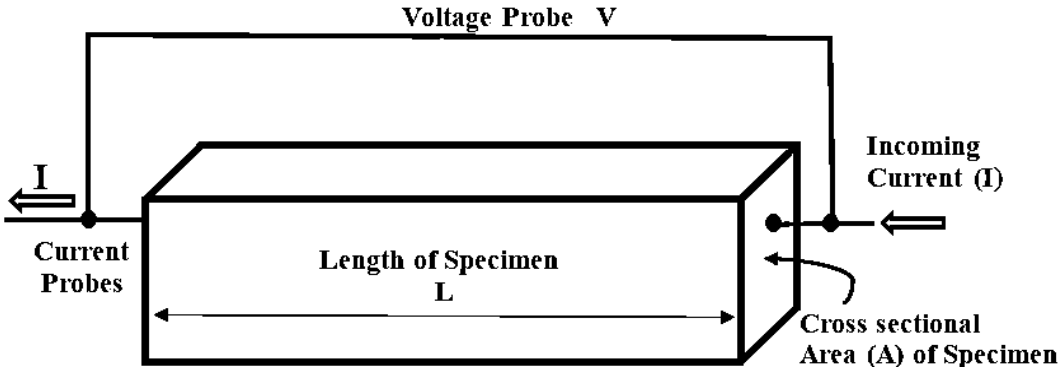

Figure 1.14: Illustration of "Two Point Probe Method".

Resistance can be calculated through Ohm law given as

$$R = {}^{V}/_{I} \qquad 1.28$$

Specimen resistivity is calculated as

$$\rho = {}^{VA}/_{IL} \qquad 1.29$$

Where, potential difference (V) and current (I) are measured for sample of surface cross section **(A)** and length **L**. Contact points and probe resistances have an impact on measured current.

1.5.8 Van der Pauw Measurement

Majority charge-carrier current as a result of applied magnetic field (B) is measured by Hall-effect measurement. "Vander Pauw" (four point probe) tool is used to measure "resistivity", "Hall mobility", "charge-carrier concentration" and "n/p-type" of material. [138, 178]. Hall measurement setup is shown in Fig. 1.15.

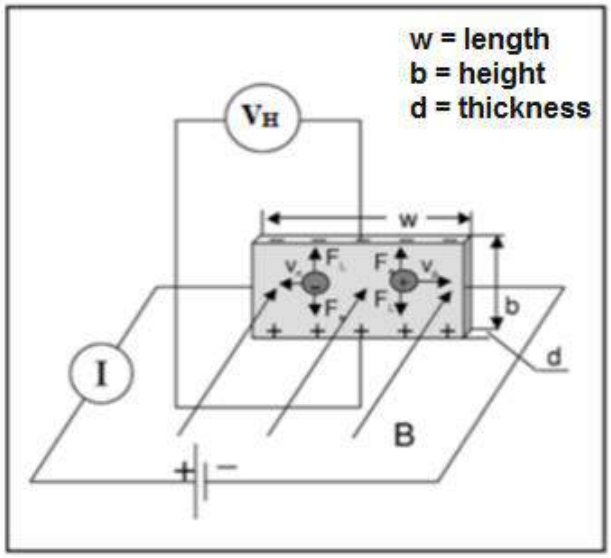

Figure 1.15: Design of Hall effect measurement setup.

If current I is permitted to flow through a conductor (/square/rectangular or thin film) , then "magnetic field" $B_{\perp}$ (plane of conductor) applies "Lorentz force" $F_{\perp}$ (direction of current in conductor and magnetic field) . This force is given by [138, 178]

$$F_{\perp} = q(V \times B_{\perp}) \qquad 1.30$$

This force deflects positive charges on one side and negative charges in opposite direction. Therefore a potential difference is created on the two opposite sides of

conductor, perpendicular to magnetic field which is known as hall voltage (V_H). Majority charge carriers can be assessed by potential polarity calculated by [138]

$$\boldsymbol{n = \frac{1}{e.R_H}} \qquad \textbf{1.31}$$

Hall voltage and Hall coefficient are related to each other as shown in equation below [138, 178]

$$\boldsymbol{R_H = \frac{V_H.d}{B.I}} \qquad \textbf{1.32}$$

Resistivity is given by [138, 178]

$$\boldsymbol{\rho = \frac{R.A}{w}} \qquad \textbf{1.33}$$

Where R is the resistance of material under observation and A is its cross sectional area.

EXPERIMENTAL

Chapter 2

This section comprises of a chapter covering three sub-sections

- Preperatory Stage
- Deposition Chamber Design
- Optimization of thin film deposition parameters

Chapter 2

2 Experimental Outline

This research project has been completed in two stages (phases). The first phase includes deposition chamber modification and optimization for a better thin film growth. Second phase involves composite film deposition including two steps as mentioned below:

Step 1: Films were deposited on n & p-type polished Si wafer. Target-substrate distance was also varied for optimization of Ge concentration for improved optoelectronic response.

Step 2: Layer by layer deposition was done such that each layer was deposited for a comparatively shorter time on n-type polished and unpolished substrate under optimized conditions.

Sample such prepared were characterized using various analytical tools details involving basic working and analysis of results are explained in this chapter. Before fabricating thin films TiO_2-Ge composite nano particles were synthesized to check whether composites can be fabricated through Laser ablation process which has been reported and attached in Annex 1. After successful synthesis of composite nanoparticles we fabricated thin films which are mentioned in this thesis.

A configuration step was also involved related to the target and substrate preparation before deposition.

2.1 Preparatory Stage

(Target and Substrate Preparation)

Targets consisting of pure TiO_2 & TiO_2-Ge composite were prepared and N & p-type Si wafers were polished and cleaned before deposition.

2.1.1 Target Preparation

TiO_2 and Ge powders (99.99% pure), purchased in bulk form from Sigma Aldrich to prepare pure TiO_2 (2g) and TiO_2-Ge (2g) composite targets. Thin films of pure TiO_2 were initially deposited to optimize the maximum achievable and sustainable pressure to be used to deposit thin films with minimum surface roughness. After pressure optimization, molar weight ratio of 1:4 (Ge: TiO_2) was chosen for sample preparation for present studies to prepare composite targets. Concentration ratio 1:4 was chosen as it is reported earlier by A.Slav [2] that thin films containing 22% Ge showed some absorption transitions in visible region. We mixed 0.37g of Ge (20% of molecules of Ge) in 1.63g of TiO_2 (80% of molecules of TiO_2) to make a 2g of TiO_2-Ge composite pellet.

Figure below shows the step by step process involved in composites target preparation, for TiO_2 target processes shown in yellow are not included.

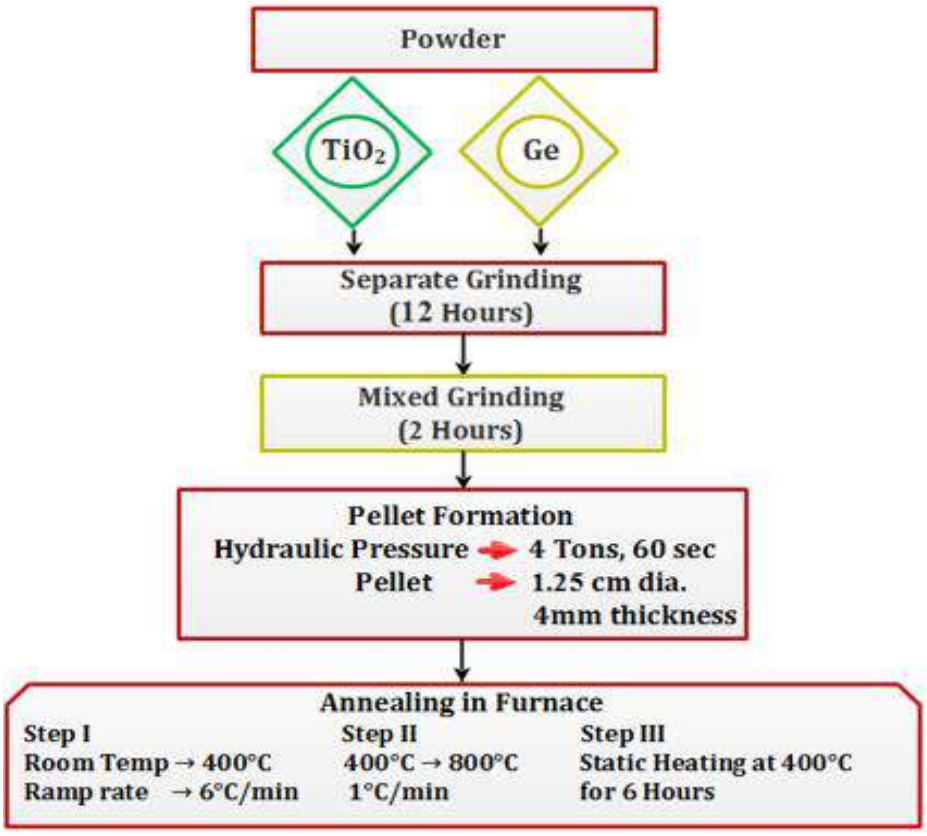

Figure 2.1: Detailed procedure for composite target preparation.

This raise in temperature in steps up to 800°C was adopted to refrain pellets from cracking as unstable phases (anatase & brookite) transform into stable phase (rutile) as per literature. The multiple phenomena's occurring during rise in temperature is summarized as follows.

Brookite is converted to anatase phase at temperature ~400°C [150]and anatase phases of TiO_2 start converting to rutile structure of TiO_2 in a wide temperature range of 400°-1200°C [179]. Complete conversion of anatase to rutile takes place around 750°-1200° C [150]. Ge has a melting point of 937°C So 800°C was chosen as annealing temperature for pellets so that Ge may not oxidize or react chemically with TiO_2. As the volume per molecule of brookite, anatase and rutile is 32.172 $Å^3$, 34.061 $Å^3$ and 31.216 $Å^3$ [149]. Therefore rise in temperature to 400°C will result in expansion of 1.889 $Å^3$ for every brookite molecule converted to anatase molecule. Rutile has minimum volume so when temperature is increased beyond 400°C anatase having maximum volume per molecule shrinks with reduction in lattice parameters forming rutile TiO_2. So decrease in volume per molecule is 2.845 $Å^3$ which results in cracking of pellet due to internal strains as a result of change in volume. So ramp rate of 1°C/ min was maintained from 400 to 800°C.

Structural properties of synthesized pellets were studied through X-ray diffraction, as well as to verify the composite formation No peak related to germanium oxide appeared in XRD of pellets, which can be verified by graph shown in Fig. 2.18 .

2.1.2 Substrate Preparation

As thin films were to be deposited on polished and unpolished silicon wafers, therefore half of wafers were polished and finally polishes and unpolished wafers were etched before deposition n and p-type Si wafers purchased from Solenergy Japan with orientation (100) and (111) respectively were polished by SiC. Polished & unpolished wafers are presented in Fig. 2.2.

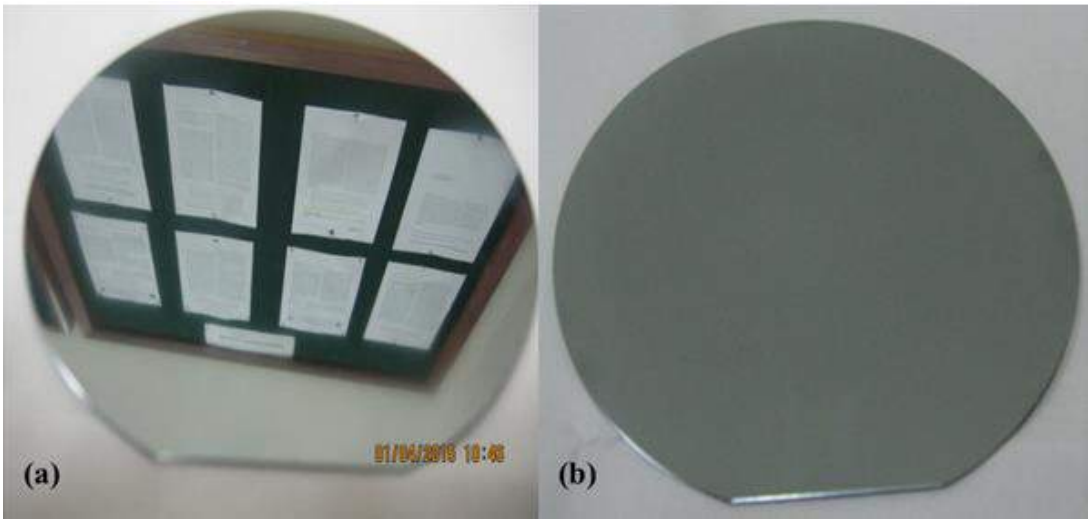

Figure 2.2: Photograph of polished (a) and unpolished (b) Si.

After polishing Si was cut into square pieces (1cm^2) using diamond cutter and cleaned in lab using standard RCA cleaning procedure in order to eliminate impurities i.e. carbon from SiC polish and other contaminations while handling. RCA is a standard etching process covering three steps; "standard clean protocols" (SC), titled as "SC1", "SC2" and "SC3" in Fig. 2.3.

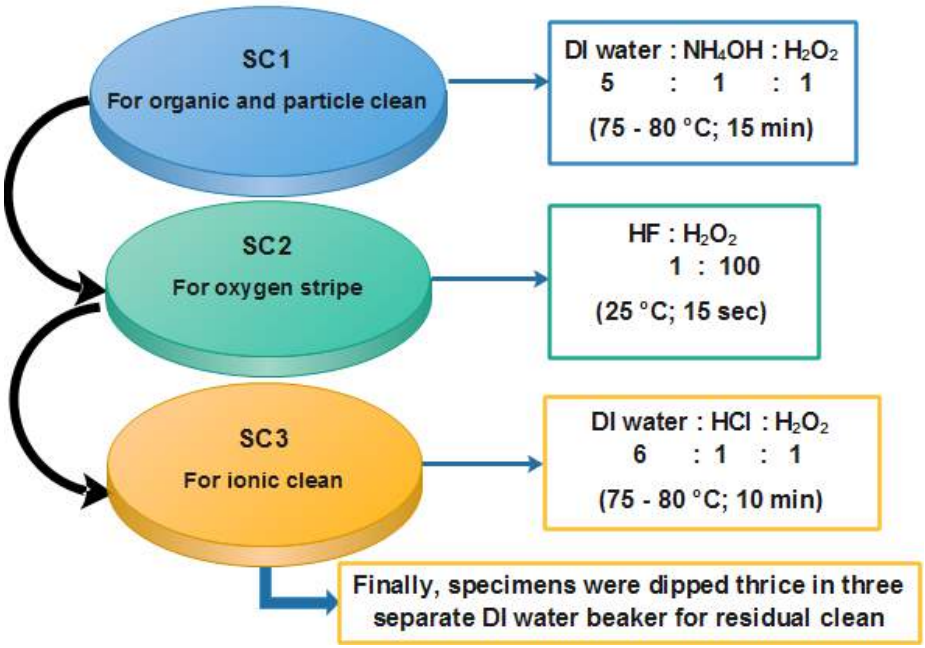

Figure 2.3: Pre deposition wafers cleaning procedure i.e. "Standard RCA clean procedure".

No carbon or contamination traces were identified on Si wafer through EDX and Laser Induced Breakdown Spectroscopy after RCA clean.

2.1.3 Deposition Chamber Design and Optimization for Thin Film Deposition

Deposition chamber was designed to in accordance to our experimental design. For the purpose a high vacuum grade stainless steel hoop of thickness 1 cm with inner diameter 29 cm and length 35 cm was utilized. Machining was done in workshop to add feed through for substrate and target holders such that target and substrate lie parallel to each other and at 45° with the laser beam. As well as groves were added to fit in seals in order to achieve high vacuum. Inlets were added through machining for vacuum and pressure gauge fitting.

Substrate and target holders were designed with fitting adjustment in accordance to feed through and avoid fall off or misalignment due to vacuum or rotation. Substrate and target holders feed through were fitted with motors having angular speed of 5 rev/min A quartz window with 99% transmittance to UV was added on front side of deposition chamber for laser irradiance on target. A side window was also added to view beam focusing on to target, plume and observing deposition process. Therefore the prepared chamber comprised mainly of:

- Stainless steel (SS) cavity with two windows, outlets (vacuum & air)
- Adjustable substrate & target (pellet) holder.
- Motors to rotate target and substrate

Design of deposition chamber is given in Fig.2.4.

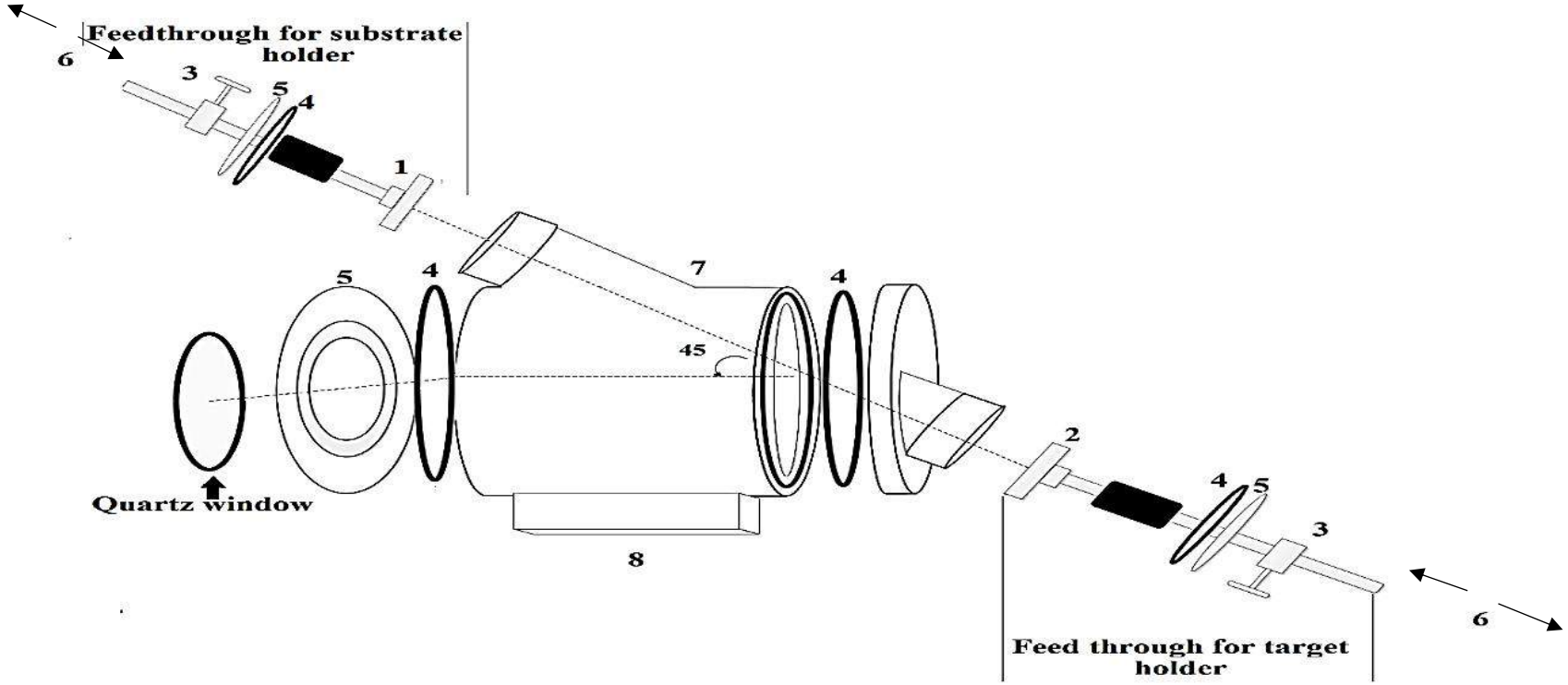

Figure 2.4: Illustration of deposition chamber design where (1) substrate holder, (2) Target holder, (3) stopper for target to fix the feed through at a fixed distane while it can ritate freely, (4) sealing rings to vacuum the chamber, (5) high vacuum grade stainless steel cover, (6) feed through movement for target-substrate distance variation, (7)) high vacuum grade stainless steel chamber and (8) chamber base for support. Side view window, inlets for gas & vacuum and motors are not shown for the sake of simplicity.

Front and rear view of the deposition chamber are shown in (Fig. 2.5a & b) where front Quartz window and view window can be observed.

Figure 2.5: Photograph displaying front (a) and rear view (b) of Deposition Chamber.

Target holder is aligned at 45° with incident laser beam adjusted by feed-through. Substrate holder (fixed on another feed-through) is adjusted facing opposite to target holder as demonstrated in Fig. 2.6 and previously shown in schematic diagram Fig. 2.4.

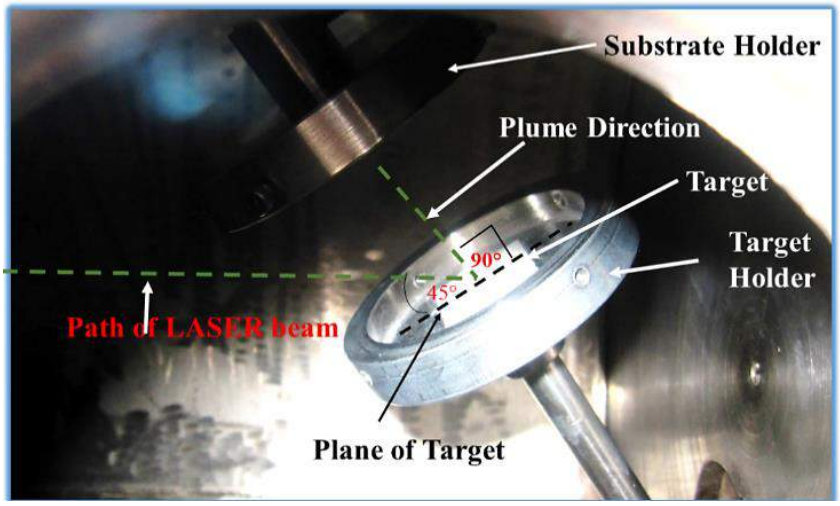

Figure 2.6: Internal view of substrate (above) and target holder (below) alignment.

Before deposition chamber was thoroughly cleaned to avoid any contamination during deposition. Therefore initially the chamber was cleaned by isopropanol and then by acetone. Final cleaning step was vacuum conditioning as it aids in attaining consistent results for experiments performed in vacuum. There are chances of moisture build up for any system placed in air for longer time [6] therefore, conditioning was carried out before running it for deposition. The chamber and all of the parts were first cleaned by

the nitrogen gun.

In the second and final step the system was run for vacuum until it got a stable vacuum for 24 hours. This process took a much longer time as any small impurity on the walls of chamber and any other part can cause instability in vacuum. Therefore the system was constantly run for vacuum through rotary pump to produce a vacuum of 4×10^{-3} m bar while heating its walls with heating tape (i.e. baking process) and after wards without applying heating tape for about 2 more weeks till it achieved a stable vacuum. Thin films were deposited at low vacuum (4×10^{-3} m bar) first and then characterized for their structural properties and surface morphology by XRD and SEM.

The second target was to achieve a high vacuum ~ 10^{-6} m bar. For the purpose system was coupled with diffusion pump backed up by rotary pump. It took a much longer time to achieve stable vacuum of 8×10^{-6} m bar, as the vacuum seals previously used at low vacuum could not be used for high vacuum therefore high vacuum seals were used. As well as leak diagnostics to achieve high vacuum becomes more difficult. Thin films deposited at high vacuum were also characterized to study their crystallinity and surface morphology by XRD and SEM.

For each deposition all components (target & substrate holders) and walls of chamber were cleaned to get rid of any impurities. Afterwards substrate and target were mounted on respective holders before vacuum. Low vacuum (~4×10^{-3} mbar) in chamber was achieved by rotary pump which was further increased to 8×10^{-6} mbar via diffusion pump

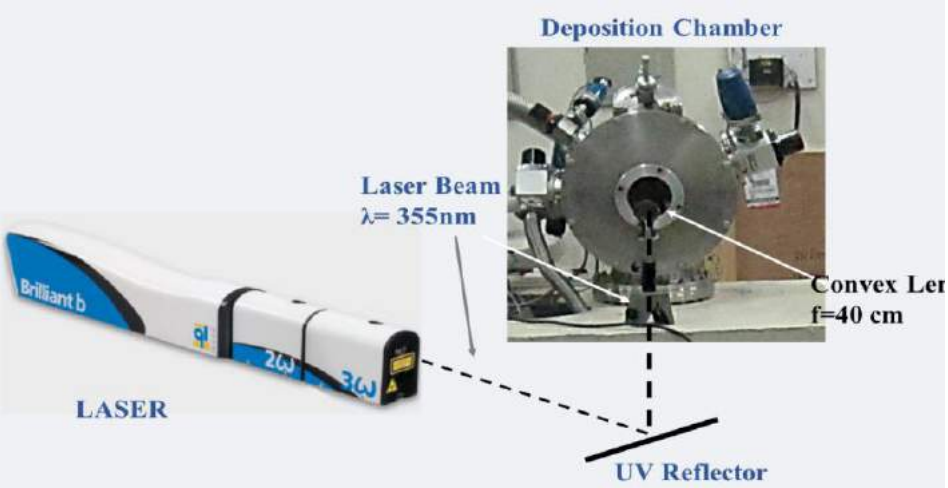

Figure 2.7: PLD Setup.

Major components of deposition setup were optics, deposition chamber and laser

source. Optical components i.e. UV-reflector and quartz lens were purchased from Ocean Optics. PLD setup is exhibited in Fig. 2.7.

"Nd:YAG Q-switched LASER" by "Quantel (Twins B)" having first harmonic lying in IR (i.e. λ= 1064 nm), maximum energy of 850 mJ/ pulse with 5ns pulse width, effective beam diameter of 9 mm and repetition rate of 10 Hz was energy source.

After approaching stable pressure of 8×10^{-6} mbar in deposition chamber, target ablation was performed by focusing third harmonic (λ = 355 nm; E = 100 mJ) on to target by a convex lens of focal length 40 cm with a spot size of 1 mm in diameter, such that the fluence was 12.73 J/cm^2. As a consequence of laser-target interaction conical-violet plume was formed which is presented in Fig 2.8.

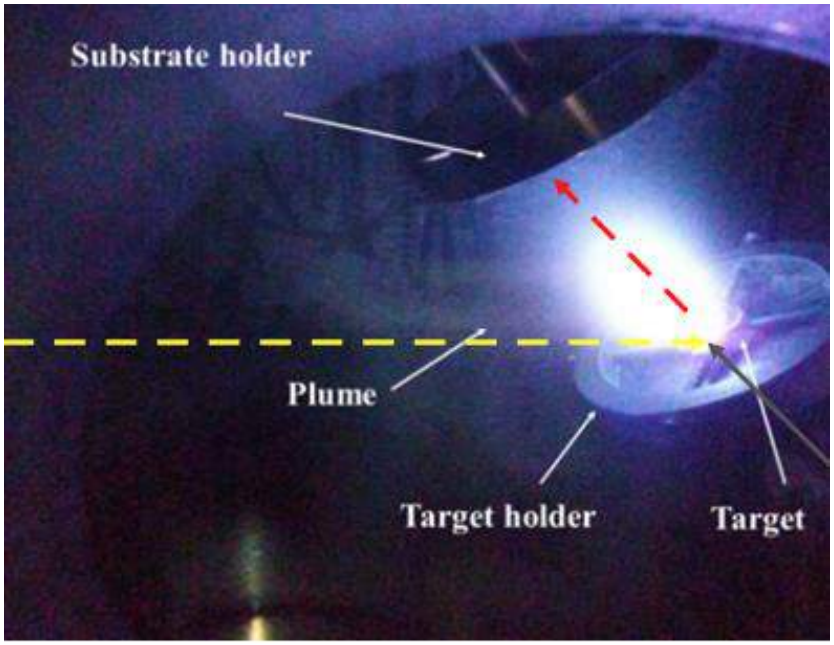

Figure 2.8: Conical plume formationd by laser irradiance showing direction of laser baem (yellow) and plume (red).

Evaporated material in the form of plasma drifted towards substrate where it was deposited as thin films. Pure TiO_2 film deposited at low and high vacuum were compared for their crystallinity by XRD and surface morphology by SEM.

Results and related discussion is explained in later section in this chapter. During each deposition some of the conditions were kept constant as mentioned in Table 2.1.

Table 2.1: Conditions maintained during each deposition process

Pressure in Deposition Chamber (mbar)	**Focal length of convex lens (nm)**	**Laser wavelength (nm)**	**Laser beam energy (mJ)**	**Laser fluence (J/cm^2)**	**Target composition (Molar ratio) TiO_2 : Ge**
8×10^{-6}	30	355	100	12.73	4 : 1

2.2 Composite Films Deposition Phase

Thin films were deposited in two batches. In each batch multiple samples were preparing for a specific condition and were compared for their properties. It was observed that repeated samples showed almost same properties explained in later sections. In the first batch TiO_2- Ge films were deposited on n (100) and p-type (111) polished Si by varying target-substrate separation from 5-8 cm. All the depositions were carried out for thirty minutes. Details of the samples are shown in table 2.2.

Table 2.2: Description of samples fabricated in Batch I

Sample Code	**Substrate**	**Deposition time'T' (min)**	**Target-substrate separation 'X' (cm)**
NSi5-30	n-type polished	30	5
NSi6-30			6
NSi7-30			7
NSi8-30			8
PSi5-30	p-type polished	30	5
PSi6-30			6
PSi7-30			7
PSi8-30			8

Samples fabricated in the first batch were characterized and it was found that the sample NSi6-30 (i.e. X=6 and T=30 min) had better optical and electrical properties which are discussed in chapter 4. Therefore, considering the deposition conditions for this sample as optimized, the second batch of samples was fabricated under these conditions for reduced time with a modified strategy. Single, di and tri-layered films were grown on

polished & unpolished n-type Si (100) wafer. These samples were then studied to investigate the effect of substrate surface and multilayers for the optoelectronic response. A detail of these samples is shown in Table 2.3.

Table 2.3: Detail of samples fabricated in Batch II at a X= 6 cm.

Sample Code	Substrate	Target-substrate separation (cm)	Deposition time for each layer (min)	Total No of layers	Total Deposition time (min)
NSi6-5	n-type polished	6	5	1	5
NSi6-10				2	10
NSi6-15				3	15
N´Si6-5	n-type unpolished	6	5	1	5
N´Si6-10				2	10
N´Si6-15				3	15

Schematic diagram of fabricated samples is depicted in the Fig. 2.9.

Figure 2.9: Representation of 1, 2 and 3 layer films deposited at X= 6 cm.

Thin films thickness as measured through ellipsometric data is given in Table 2.4 It is clear that film thickness films deposited in single, double and triple layer for 5 is approximately 35, 70 and 105 nm. Which shows that deposition rate was not effected for prolonged deposition.

Table 2.4: Description of thin film and their thickness measured by ellipsometry.

Sr #	Sample	Thickness "t" (nm)	Description
1.	2-NSi5-30	234.97	30 min deposition on n-type Si polished wafer
2.	2-NSi6-30	214.71	
3.	2-NSi7-30	211.37	
4.	2-NSi8-30	272.11	
5.	2-PSi5-30	310.15	30 min deposition on p-type Si polished wafer
6.	2-Psi6-30	289.04	
7.	2-Psi7-30	230.44	
8.	2-PSi8-30	246.71	
9.	2-NSi6-5	33.42	5 min deposition on n-type Si polished wafer
10.	NSi6-10	68.06	10 min deposition on n-type Si polished wafer
11.	NSi6-15	101.50	15 min deposition on n-type Si polished wafer
12.	N´ Si6-5	35.83	5 min deposition on n-type Si unpolished wafer
13.	N´ Si6-10	71.59	10 min deposition on n-type Si unpolished wafer
14.	N´Si6-15	106.76	15 min deposition on n-type Si unpolished wafer

Thin film thickness given in sample 2-NSi6-10, 2NSi6-15, 2nSi6-10 and 2nSi6-15 is the total thickness including the thickness of previous layer/layers.

2.3 Experimental Characterization Tools

X-Ray Diffraction spectroscopy was carried out at COMSATS Institute of Information Technology Islamabad. Thin films were characterized at grazing angle mode at a step size of 0.025° and at a scan rate of 2° per min. Bruker X-Ray diffractometer Model AXS; D8 ADVANCE (Fig. 2.10) under a working current and voltage of 40 mA and 40 KV, Cu-Kα beam ($\lambda = 1.5406$ Å) was used to scan thin films. The obtained data, was plotted in Origin Pro 8 after peak identification from *PANalytical X'Pert High*

Score and analyzed through *Check cell.*

Figure 2.10: X-Ray Diffractometer.

µ Ramboss spectrometer model number MST 100 A (Fig. 2.11) by DongWoo Optron Co. LTD., South Korea can be utilized for Raman spectroscopy under the excitation of He-Cd laser beam. Laser beam at 512 nm was used for Raman spectra respectively. Same arrangement with some modifications was utilized for PL spectroscopy under the excitation of He-Cd laser beam. Laser beam at 342 nm

Figure 2.11: µ Ramboss Spectrophotometer.

EDX spectroscopy was carried out for compositional analysis and distribution of Ti, O and Ge as a result of deposition through elemental mapping (Area scan) of thin films by MIRA3 TESCAN FESEM (Fig. 2.12) was carried out at Institute of Space Science and Technology Islamabad in scattering electron mode operated at 10 KV in a window size of 6 mm.

Figure 2.12 : Field Emission Scanning Electron Microscope.

UV visible reflectance was recorded from advance characterization Lab at NILOP by Hitachi U 4100 UV/VIS spectrophotometer (Fig. 2.13). Samples were scanned in the wavelength range of 300-1000 nm.

Figure 2.13 : UV/VIS spectrophotometer.

Ellipsometry characterization was carried out at IDB Lab International Islamic University Islamabad by meteorology grade spectroscopic ellipsometer from Sentech, Germany, Model No. SE 800 (Fig. 2.14). Samples were scanned under Xe lamp as illumination source in the wavelength range of 300-850 nm.

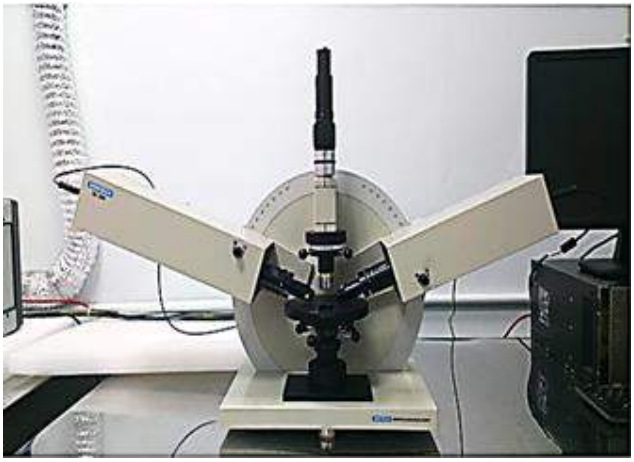

Figure 2.14 : Ellipsometer.

Electrical measurements were carried out using ASMEC electrophysical characterization system as shown in Fig. 2.15 which was operated in voltage range 0-5 V with current and charge sensitivity ranging to 1 pA and 5×10^{-16} C.

Figure 2.15: IV Measurements under vacuum.

Hall Effect measurements were carried out at Advance Electronics Lab at IIUI. SWIN is the electrical measurements setup aided with Hall effect measurement system with a permanent magnetic field of 1 T (Fig. 2.16). Van der Pauw four-point probe technique was employed for electrical resistivity, Hall mobility and n-type/Ptype identification of

thin films through it.

Figure 2.16: Hall effect measurement setup.

2.4 Optimization Phase

Pellets (targets) fabricated after sintering (for details see 2.1.1) were studied for their structural properties so that crystallinity and various stable phases can be identifies through XRD. XRD spectrum of TiO_2 pellet is shown in Fig 2.17. XRD pattern of TiO_2 pellet shows the presence of pure rutile.

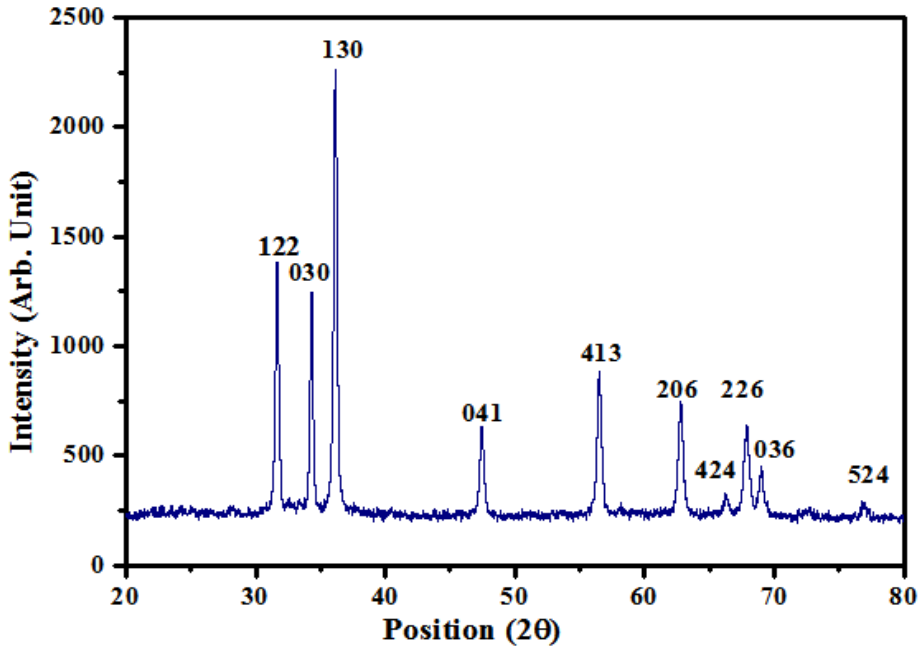

Figure 2.17: XRD of TiO_2 target after annealing.

The observed TiO_2 peaks and respective crystalline phases are identified at ***$2\theta \approx 31.7°$***

(122), 34.4° (030), 47.5° (041), 56.5° (413), 62.8° (206), 66.4° (424), 67.9° (226), 69.03° (036) and ***76.8 (524)*** in confirmation with ***JCPDS card # 01-076-0320***. Pellet has a polycrystalline nature as it contains various phases. No peak related to impurity or any other crystalline form is observed which shows the purity of TiO_2 pellet and conversion of all phases of TiO_2 to rutile during annealing.

XRD pattern of composite target demonstrates pure TiO_2-Ge composite formation (i.e. impurity peaks not detected). Ge reflection along with crystalline phases are observed and identified at ***2θ ≈ 54.1 (111), 54.5 (222)*** and ***66.01 (400) as*** confirmed by JCPDS card # ***00-004-0545*** (Fig.2.18). Three allotropes of TiO_2 i.e. "rutile", "brookite" and "anatase" are observed in XRD.

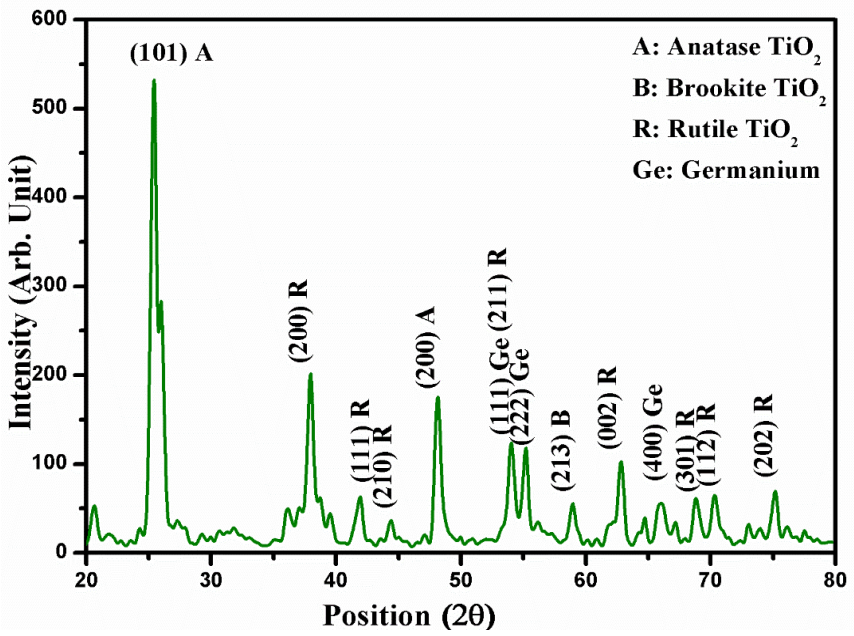

Figure 2.18: XRD of TiO_2-Ge composite target after annealing.

Maximum number of identified peaks exhibit rutile TiO_2 observed at ***2θ ≈ 38.68(200), 41.5 (111), 44.86 (210), 54.55 (211), 63.12 (002), 69.015 (301), 70.15 (112), 75.05 (202)*** and approved by JCPDS card # ***01-076-0320.*** Brookite (**2θ = *59.56 (213)***) and anatase TiO_2 (**2θ = *25.25 (101) & 48.50 (200)***) are hardly visible as distinguished by JCPDS card # ***01-075-1582*** and ***00-021-1272*** respectively. Target is polycrystalline composite in nature and peaks broadening confirms nano-particles formation of size range between 20-50 nm (calculated by Scherrer equation). Mild shifting observed in peak broadening can be attributed to strain developed by mechanisms involved in pellet fabrication.

In case of doping Ge should replace a Ti atom thus by adjusting itself in the lattice structure of TiO_2 so Ge should show tetragonal structure. But in the case of this target Ge appears in cubic crystalline form and does not follow tetragonal structure of TiO_2 thereby meaning that Ge do make composite with TiO_2. So we can say that pure TiO_2-Ge composite target was prepared successfully.

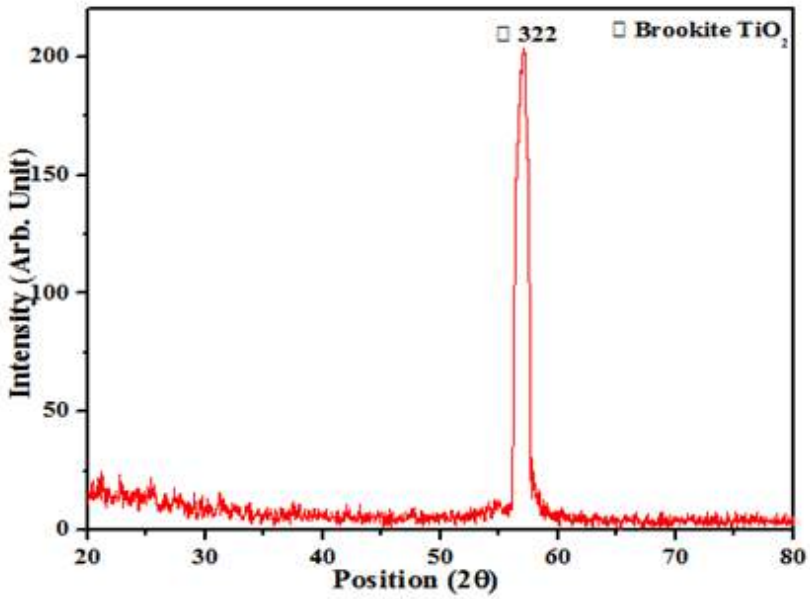

Figure 2.19: XRD of TiO_2 films deposited under low vacuum (~ 4×10 $^{-3}$ m bar).

These pellets were then used to grow thin films on Si wafers. In the initial stage TiO_2 pellet was used to grow thin films under low and high vacuum. Thin films deposited under low vacuum were initially studied by XRD which is shown in Fig. 2.19.

XRD spectrum of TiO_2 film deposited at low vacuum (Fig. 2.19) shows a prominent peak around ***2θ=57.05°*** which corresponds to brookite phase of TiO_2 as identified by JCPDS card # ***01-075-1582.*** Average crystallite size is found to be 40 nm. It is clear that an unstable phase of TiO_2 appears in films prepared at low vacuum.

The thin film deposited at high vacuum are polycrystalline in nature as can be observed through the XRD spectrum obtained for the film as shown in Fig. 2.20. Thin film grown at high vacuum was although polycrystalline but it has dominant rutile crystalline phase whereas a single peak related to brookite TiO_2 is observed around ***2θ= 50.61°***. Different phases of rutile TiO_2 are observed around ***2θ= 39.46°, 42.84°, 56.06°, 63.07°*** and ***70.99°*** as ***(200), (210), (220), (310)*** and ***(112) .*** Average crystallite size as per Scherrer formula was 50 nm. Conclusively, thin film grown under higher vacuum had a dominant stable

phase rutile and polycrystalline in nature. As well as phases observed in targets were nit observed in thin films.

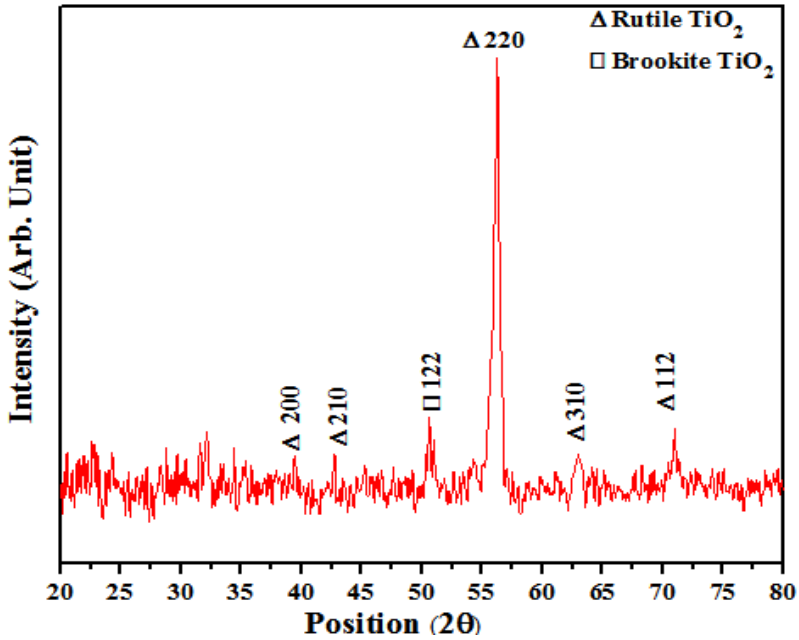

Figure 2.20: XRD of TiO_2 films deposited under high vacuum (~ 8×10^{-6} m bar).

Adherence test was carried out on these films and films developed under higher vacuum were more strongly adhered to the substrate. Therefore the films which were deposited under high vacuum were found to be stable.

Surface roughness of thin films was measured through Atomic force microscopy and the surface roughness was found to be 35.5 and 20.1 nm (Fig. 2.21) in thin films deposited at low vacuum and that of substrate to be 4.3 nm.

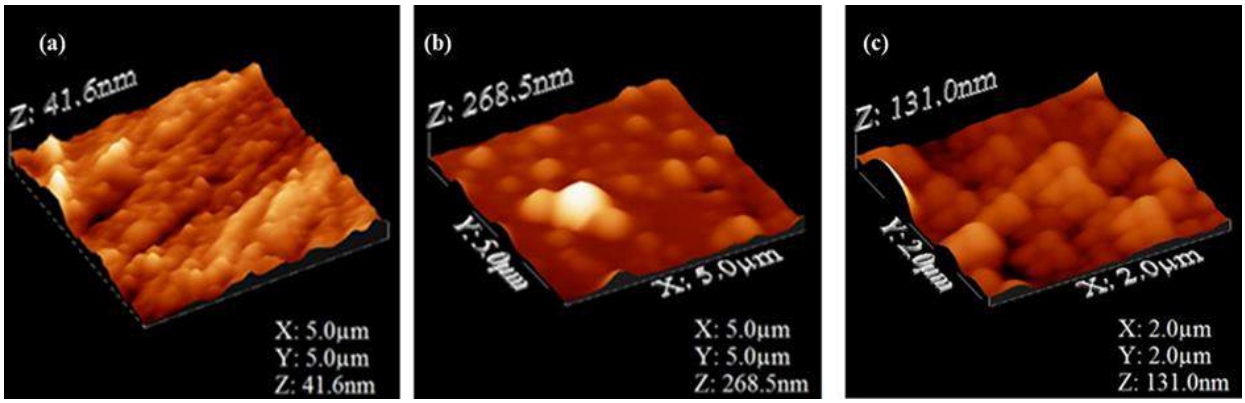

Figure 2.21: AFM images of (a)Si substrate, TiO_2 films deposited on Si substrate under (b) low and (c) high vacuum.

As film roughness reduced (smoothness enhanced) in thin films deposited at higher vacuum so all the composite films were deposited under high vacuum.

As thin film synthesis is a multiple step process (Fig. 2.22) which includes physical absorption on substrate, bond formation between particles and substrate, nucleation grain growth an d bulk diffusion.

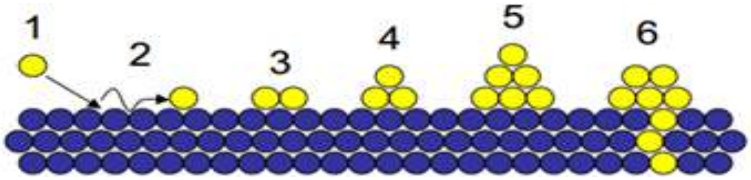

Figure 2.22: Various processe undergoing during and after thin film deposition, (1) condensation, (2) physical absorption on substrate, (3) bond formation between particles and substrate,(4) nucleation, (5) grain growth and (6) bulk diffusion.

Therefore deposited thin films were then kept under vacuum i.e. at 8×10^{-6} mbar for 24 hours to stabilize their bonds as the thin films which were removed from deposition chamber deposition few hours after deposition were peeled off from the substrate. SEM of peeled off samples is shown in Fig. 2.23.

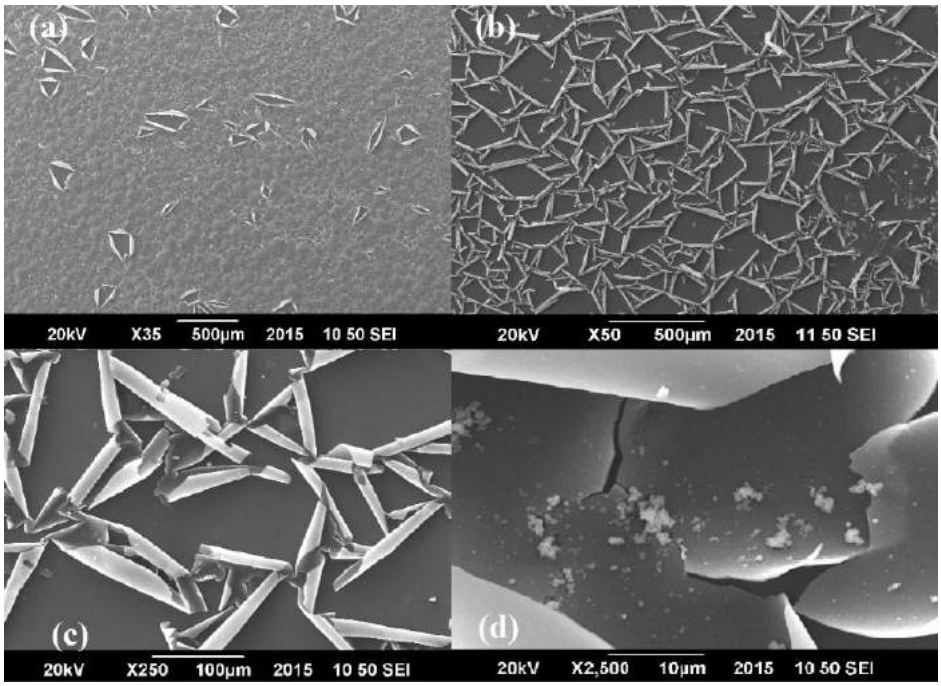

Figure 2.23: SEM micrographs of thin films peeled off when taken out of vacuum chamber after 4 hours.

It is clear that the films after peeling have rolled out which is due to strains in the film. Which is possibly due to much less time to adhere to substrate by diffusion of deposits in substrate.

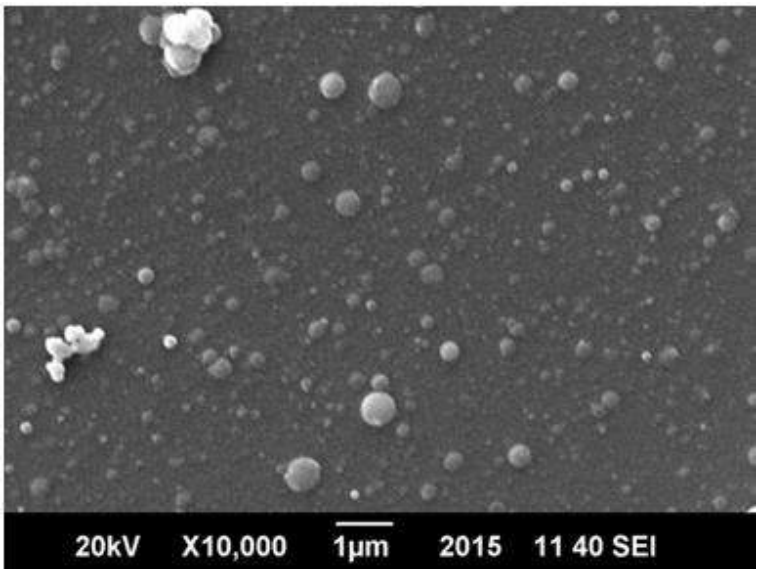

Figure 2.24: SEM micrograph of thin film which was kept in vacuum for 24 hours after deposition.

Therefore films were left in vacuum for 24 hours after diffusion resulting in a stable adhered film i.e. no cracking or peeling was observed (Fig. 2.24)

Therefore composite thin films were deposited on etched Si wafer at high vacuum ~8×10^{-6} mbar. The samples after deposition were kept under vacuum for next 24 hours and then were taken out of deposition chamber.

RESULTS AND DISCUSSIONS

Chapter 3, 4, 5

This section has been divided into three chapters explaining results & their discussions related to:

- Structural and Compositional Analysis (Chapter 3)
- Optical Studies (Chapter 4)
- Electrical Characterizations (Chapter 5)

This section has been divided into three parts first part is related to structural and compositional analysis of thin films (Chapter 3). Second part elaborates the optical characterization (Chapter 4) and the last chapter explains the electrical characterization of thin films in dark and light (chapter 5)

During the optimization part targets were fabricated and were characterized for their structural properties. Pure TiO_2 thin films deposited at low and high vacuum on N-type Si wafer were characterized for their structural properties through XRD and their surface morphology was also studied. Thin film adherence with substrate was tested through tape test for thin films deposited at low and high vacuum conditions.

In the second Phase thin films were deposited at optimized condition on N and P type substrate by varying target-substrate distance. The samples were characterized for their optoelectronic response in order to identify suitable substrate and target-substrate distance. Thin films deposited on Si wafers were characterized to analyze their optoelectronic response by studying their structural, morphological, compositional, optical and electrical properties.

Thin films deposited on n-type Si (100) wafer show better properties as compared to thin films deposited on P type Si (111) wafer. Among all the samples fabricated on n-type Si wafer it can be observed that NSi6-30 (details of sample in Table 2.3) shows better optoelectronic properties as mentioned in optical properties and electrical properties explained in detail in Chapter 5 & 6.

Therefore target-substrate distance i.e. 6 cm and n-type Si wafer as substrate was considered to grow thin films for the next batch of samples. Again in this batch thin films were grown on n-type polished and unpolished Si wafers (details of sample in Table 3.3) at the optimized distance as mono-, di- and tri- layers. For the sake of simplicity all the results are categorized into three sub sections

- Structural and compositional analysis
- Optical Characterizations
- Electrical Characterizations

Related results are discussed which are subdivided into two parts; (a), for thin films deposited on p & n-type polished substrates and (b) for thin films deposited as single,

di- and tri layers on n-type polished and un-polished substrates: Hence, this section presents the optimization phase results and comparison of properties of thin films deposited by the above two mentioned schemes.

Chapter 3

3 Structural and Compositional Analysis

Structural characterization and morphological analysis of thin films was carried out through XRD, EDX analysis and Raman spectroscopy. XRD was employed to identify the crystallinity of thin films. Crystallite size, dislocation density (DD) and strain was calculated through the analysis of XRD spectra. Ge concentration and distribution was calculated in all thin films through EDX. Raman spectroscopy was carried out to determine the composite nature of film.

3.1 X- Ray Diffraction (XRD)

X-ray diffraction spectra of composite TiO_2 –Ge films deposited on n-type Si is displayed in Fig. 3.1. TiO_2 and Ge in thin films were identified by various JCPDS cards. Three allotropes of TiO_2 were confirmed through JCPDS cards # 01-076-0320 (Rutile), 00-021-1272 (Anatase), 01-075-1582 (Brookite) and Ge was identified by JCPDS cards # 00-004-0545.

Rutile, anatase and brookite allotropes of TiO_2 are detected in various peaks as shown in Fig. 3.1(a)-(d) but Ge is only observed in films deposited at 8 cm from target (Fig 3.1 d). All the films deposited at various target-substrate seperation show different crystillinity . Crystillinity of thin films deposited at different target-substrate distance ‘X’ as multiple different crystalline peaks are observed in all samples, except one peak observed around $2\theta = 23°$ in all samples. Thin film deposited at X=8 cm shows poly-crystallinity which decreases in other thin films which is due to the fact that plasma temperature decreases at higher distance from point of ablation (focal point) so particulates and ions condensate as crystals in thin films [180] deposited at higher ‘X’.

A prominent peak related to ***(101)*** phase of Anatase TiO_2 is observed around ***2θ***=

23.66°, 23.62°, 23.80° and 24.13° in (a), (b), (c) and (d) which have been shifted to lower diffraction angle in comparison to standard value ***25.28°*** (Table 3.1). Maximum shifting is observed in thin film deposited at 6 cm from target. Shifting in peaks is associated to the increase in lattice parameters calculated through check cell and which then cause an increase in lattice strains [162].

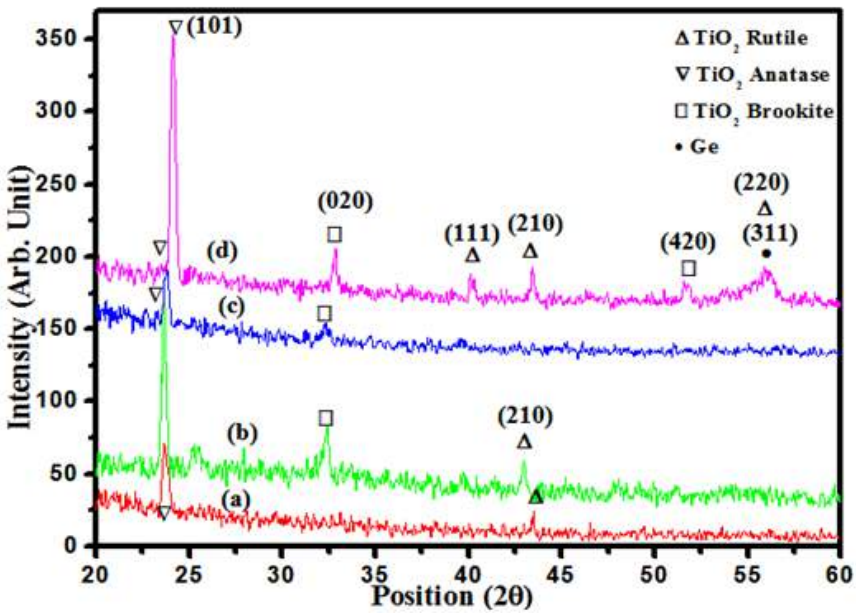

Figure 3.1: X-Ray Diffraction spectra of Thin films deposited at a target-substrate distance of 'X'= (a) 5 cm, (b) 6 cm, (c) 7 cm and (d)8 cm on n-type Si wafer.

Thin films show a mixed behavior of polycrystalline and amorphous nature. The average crystallite size computed from the first peak in Fig. 3.1 (a), (b), (c) and (d) through Scherrer formula was found to be ***15.45, 12.98, 11.30*** and ***13.58*** nm. Similar behavior is observed in other reflections observed around ***40°, 43°*** and ***56°*** related to ***(111), (210)*** and ***(220)*** phases for rutile TiO_2. ***(020)*** phase of brookite titania shows the reflection peak at a higher 2 θ value as compared to standard value in thin film deposited at 8 cm where as thin films deposited at 6 and 7 cm show shift to lower value related to increase in lattice parameters calculated through check cell.

A peak observed around ***56°*** in thin film deposited at 8 cm from target is related to TiO_2 and Ge both this peak is broadened which may be associated to micro strains produced in crystalline structure because of defects or dislocation density. Peak broadening is non symmetric which is due to uneven stresses i.e. tensile stress in TiO_2 and

compressive stress in Ge [181].

One important thing to be noted here is that only two XRD peaks observed in targets (Fig 2.18) related to anatase (101) and rutile (200) phase of TiO_2 can also be observed in thin films (Fig. 3.1). These diffraction peaks in targets appear around $2\theta = 25.25°$ and 44.86° in target which shift to lower 2θ in thin film resulting in an increase in lattice parameters [162]. Therefore it is clear that target material has undergone a structural change while ablating as well as it is clear that target and thin film structure is not the same as reported earlier [142, 182, 183].

Impurity peaks could also not be observed in the XRD spectra of thin films deposited on p-type (111) Si wafer (Fig. 3.2). It is clear that the films deposited at X=5, 6 and 8 cm show crystalline peaks related to rutile, anatase and brookite phase of TiO_2 and identified through JCPDS cards # 01-076-0320, 00-021-1272 and 01-075-1582. No significant diffraction peak related to Ge is observed in these films so Raman spectroscopy was performed to identify Ge content. Thin film deposited at X=7 cm are either amorphous or non- crystalline in nature as XRD pattern is devoid of peaks

Table 3.1 shows the crystallite size of the prominent peak in each spectrum and averaged strain and dislocation density for each sample. Crystallite size, strain and dislocation density were calculated by using Eq. 1.23, 1.21 and 1.22.

Table 3.1: Crystallite size, strain, dislocation density and lattice parameters calculated from the XRD data in thin films deposite on n-type polished Si wafer at different target-substrate distanes (X).

Ge in Thin film (at %)	**X**	**Crystallite size (nm) (D)**	**Strain (η)**	**Dislocation density (δ)**	**Average lattice parameters (A°)**					
					TiO_2 (Anatase)			**Ge**		
					a	b	c	a	b	c
25.3	5	15	0.0022	4.97×10^{15}	4.09	4.09	9.51	------	------	------
2.6	6	13	0.0023	5.94×10^{15}	4.1	4.1	9.51	------	------	------
1.9	7	11	0.0032	1.12×10^{16}	4.06	4.06	9.51	------	------	------
0.9	8	14	0.0022	1.19×10^{16}	3.99	3.99	9.51	5.66	5.66	5.66

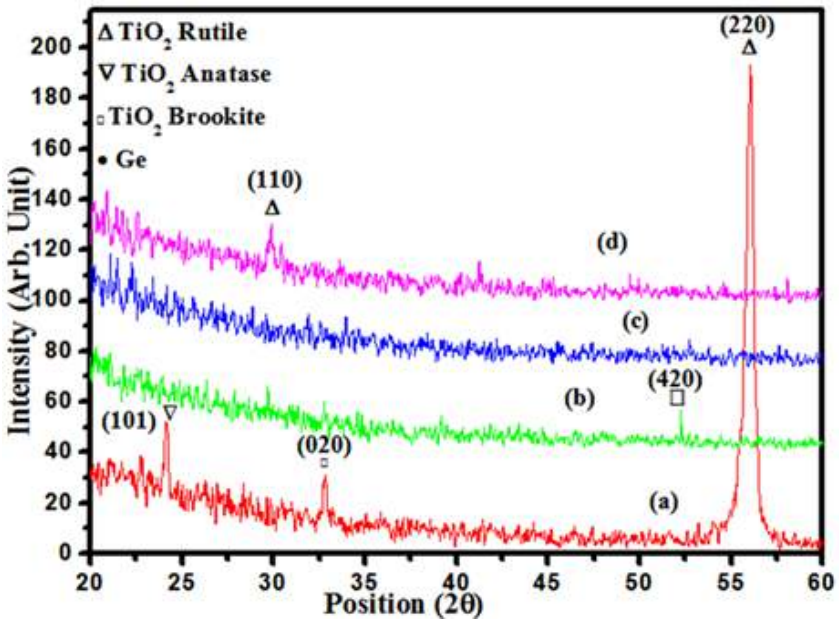

Figure 3.2: X-Ray Diffraction spectra of thin films deposited at a target-substrate distance 'X'= (a) 5 cm, (b) 6 cm, (c) 7 cm and (d)8 cm on p-type (100) Si wafer.

A sharp peak related to rutile TiO_2 ***(220)*** phase is observed around ***2θ = 56.054°*** in thin film deposited at X=5 cm. Brookite ***(020)*** and anatase ***(101)*** phase is also observed around ***32.82°*** and ***24.12°*** in this film respectively.

A single peak related to brookite phase of TiO_2 is observed around ***54.6°*** in thin film deposited at X=6 cm. Thin films deposited at X=7 cm show amorphous behavior i.e. no peaks are observed in related spectrums. Amorphous behavior in these films is due to the lattice mismatch between p-type Si (111) and TiO_2 matrix.

A single crystalline peak of ***(110)*** phase related to rutile TiO_2 is observed around ***29.89°*** in thin films deposited at X=8 cm. At smaller target-target separation more stable phases of TiO_2 are produced which is not observed in samples deposited at X > 5cm. This trend may be attributed to high plasma temperature at smaller target-substrate distance leading to the formation of stable phases.

Table 3.2 shows that there is a difference between the properties of thin films deposited on N and p-type Si wafer. Thin films on n-type (100) wafer have smaller crystallite size, larger strain and dislocation density as compared to the films on p-type (111) wafer. This is due to the fact that smaller lattice mismatch [129], atoms in thin films

were trying to arrange them in accordance to the substrate resulting in strained thin film as explained in Fig. 1.3.

Table 3.2: Comparison of thin films deposited on p-type Si wafer.

Target-Substrate Distance (cm)	**Crystallite size D (nm)**	**Strain (η)**	**Dislocation density (δ)**	**Allotrope of TiO_2**	**Average lattice parameters TiO_2**		
					a (A°)	b (A°)	c (A°)
5	28.72	0.00106	1.21×10^{15}	Rutile	4.635	4.64	2.98
6	70.15	0.00688	2.03×10^{14}	Brookite	9.184	5.4	5.14
7	---	---	---	---	---	---	---
8	24.49	0.00126	1.66×10^{15}	Rutile	4.223	4.22	2.98

The misfit factor between Si (100) and TiO_2 (100) Anatase and rutile calculated through Eq. 1.13 is found to be -0.4345 and -0.176 i.e. about 43% and 17%. But for (101) plane in anatase TiO_2 plane has interatomic spacing 10.23A° which is 1.88 times the interatomic spacing in Si (100) for reference see Annex II. Therefore TiO_2 (101) strained planes formation is favoured in thin films deposited on n-type Si (100) wafer with few planes of rutile TiO_2.

In comparison the misfit factor for rutile and anatase TiO_2 (100) with Si (111) is very high ~ -1.02 and -0.66 which is about 100% in anatase and 66% in rutile. Therefore some other planes are formed like (101) plane of anatase Titania and (220) of rutile titania which have a misfit factor of 0.2492 and 0.41 i.e. about 25% and 41% much lesser as compared to that found for (100) planes.

But the misfit factor in these films is much higher as compared to that on n-type Si (100) wafer. Therefore lesser crystalline peaks are observed in thin films deposited on p-type Si (111) wafers. Therefore, lattice mismatch has played a vital role in the development of various planes in thin films. This misfit factor resulting in strain in film gives rise to dislocations or dangling bonds which then effect the optical, electronic and electrical properties of material [129].

Single, di and tri layered thin films grown on polished and unpolished Si (100) wafers are also studies their XRD spectra are plotted in Fig. 3.3 and 3.4. Identification of TiO_2

and Ge was done through JCPD cards as used in earlier XRD spectra and no impurities could be detected.

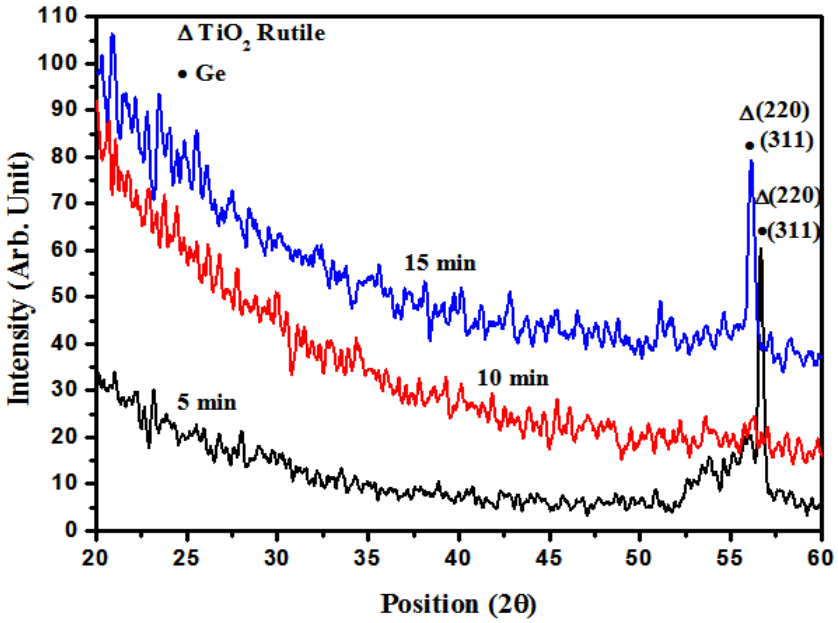

Figure 3.3: XRD of single layer (5 min), di-layer (10 min) and trilayer (15 min) TiO2-Ge composite thin film deposited on polished n-type Si wafer at X= 6cm.

An amorphous behaviour was observed in all the three samples except a peak around 2θ = 56.66° and 56.14° in single and tri-layered films. Rutile TiO_2 and cubic Ge coexistence is already identified in samples in chapter 2 (Fig. 2.18) and 3 (Fig 3.1) and also verified by Checkcell. Rutile (220) phase of TiO_2 and Ge (311) appears in single layer thin film deposited for 5 minutes but this peak vanishes in bi-layered film which may be due to hydrodynamic sputtering (but Raman spectra verifies the formation TiO_2 and Ge in this film).

Strains in thin films associated to lattice mismatch of film with substrate which increases with increase in film thickness therefore crystalline growth in thin film curtails. Anatase TiO_2 could not be detected through XRD but has been affirmed in Raman spectra. Tri-layer film again exhibits the peak related to (220) phase of rutile TiO_2 and (311) phase of Ge which is due to growth of thin film on the nucleation centers formed in bilayer film.

From here it is very clear that thin film crystallinity is also effected by the deposition time as initially crystalline film grows on Si wafer which after second layer formation becomes amorphous and same structures then regrow in third layer. Strains seem to

play a vital role on the crystallinity of thin film

Thin films deposited for 30 minutes on n-type (100) Si wafer show poly-crystallinity (Fig. 3.1 b) as compared to thin films deposited for 5 minutes (Fig 3.3). Multiple phase formation is favoured in thin film deposited for longer time because during condensation many particles may find time to nucleate and act as seeding centers which is not possible for short time deposition. As well as planes which are formed in thin films deposited for shorter time are not visible in thin films which are deposited for longer time. This may be due to higher plasma temperature in the vicinity of film which may have restructured the crystal formation in subsequent layers.

Another important aspect is the strain in thin films which is observed to be smaller for shorter time as compared to longer time (= 30 mins) deposition. Also thin films deposited for longer time are thicker as compared to that deposited for shorter time (Table 2.4). Therefore strain is likely to increase due to the formation of planes at different orientations and allotropes (rutile, anatase and brookite) [128].

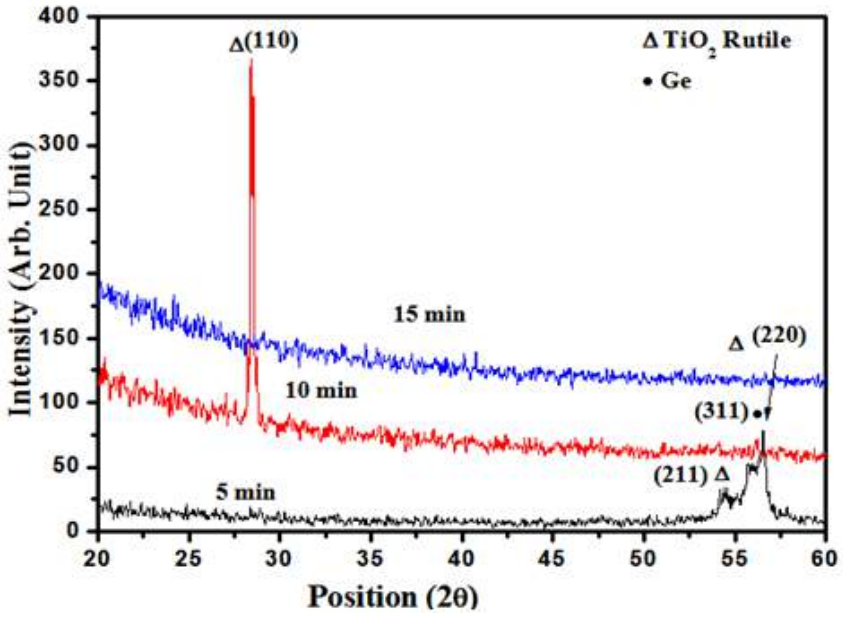

Figure 3.4: XRD of single layer (5 min), di-layer (10 min) and trilayer (15 min) TiO2-Ge composite film deposited on unpolished n-type Si wafer at X= 6cm..

Thin films deposited for 5, 10 and 15 minutes on n-type unpolished Si (100) wafer (Fig. 3.4) have a crystalline nature different as compared to those on polished Si (Fig. 3.3). It can be noted that the single layer film shows crystalline peaks of rutile TiO_2 and Ge around 54 and 56.5°. Double layer films show crystalline peak of rutile TiO_2 around

27°. An overall amorphous behavior is observed in XRD.

Also peak related to Ge is observed in single layer of TiO_2-Ge. No peak related to Ge is observed in bilayer and trilayer composite films. Trilayer film shows amorphous behavior of thin films as crystalline phases appearing in single and double layer may have vanished. Strains are developed in Ge crystals due to decrease in lattice parameters as calculated through check cell, therefore peak related to Ge (311) planes of cubic Ge has been shifted to higher 2θ value.

Table 3.3 shows the crystallite size, strain and dislocation density of the films deposited on n-type polished and unpolished Si wafer.

Table 3.3: Crystallite size, strain and dislocation density of thin films deposited on n-type substrate as single, double and trilayered.

Sample Code	**Substrate**	**Crystallite size (nm)**	**Strain**	**Dislocation Density (cm^{-2})**
2-NSi6-5	n-type polished (100) Si	28	0.000643	1.25748×10^{15}
NSi6-10		------	--------	---------
NSi6-15		24	0.00314	1.69351×10^{15}
N´Si6-5	n-type unpolished (100) Si	68	0.00027	2.16009×10^{14}
N´Si6-10		32	0.006756	1.00781×10^{15}
N´Si6-15		---------	----------	---------

It is clear that the crystallite size decreases as the number of layers is increased and hence strain and dislocation density increases. It is reported that as the strain decreases crystallinity is improved [184]. Therefore NSi6-10 and N´Si6-15 become amorphous due to increasing strain i.e. increase in strain favours amorphous behavior. Dislocation density is higher in thin films deposited on polished Si substrate.

Ge is least detected in XRD spectra but EDX (next section) and Raman (Section 3.3) confirms its presence in all the samples. As well as thin films showing Ge peaks confirm the composite formation which was also confirmed in all samples by Raman spectroscopy. Thin films composition was calculated through EDX and found that Ge content effects the optoelectronic properties of thin films[2]

3.2 Energy Dispersive X-Ray Spectroscopy

Compositional analysis of thin films was carried out to find the impact of target-substrate separation on the Ge concentration in thin films. EDX was employed to find the Ge and TiO_2 concentration in the composite films. These spectra show existence of TiO_2 and Ge without any impurity. An intense peak around 1.8 KeV is related to Si substrate while Ti and Ge are identified by various peaks which are labelled and oxygen is observed below 0.5 eV.

EDX spectra of thin films deposited on n-type Si (100) substrate are shown in Fig 3.5. Peaks related to Ge, Ti and O can be clearly observed in all the samples.

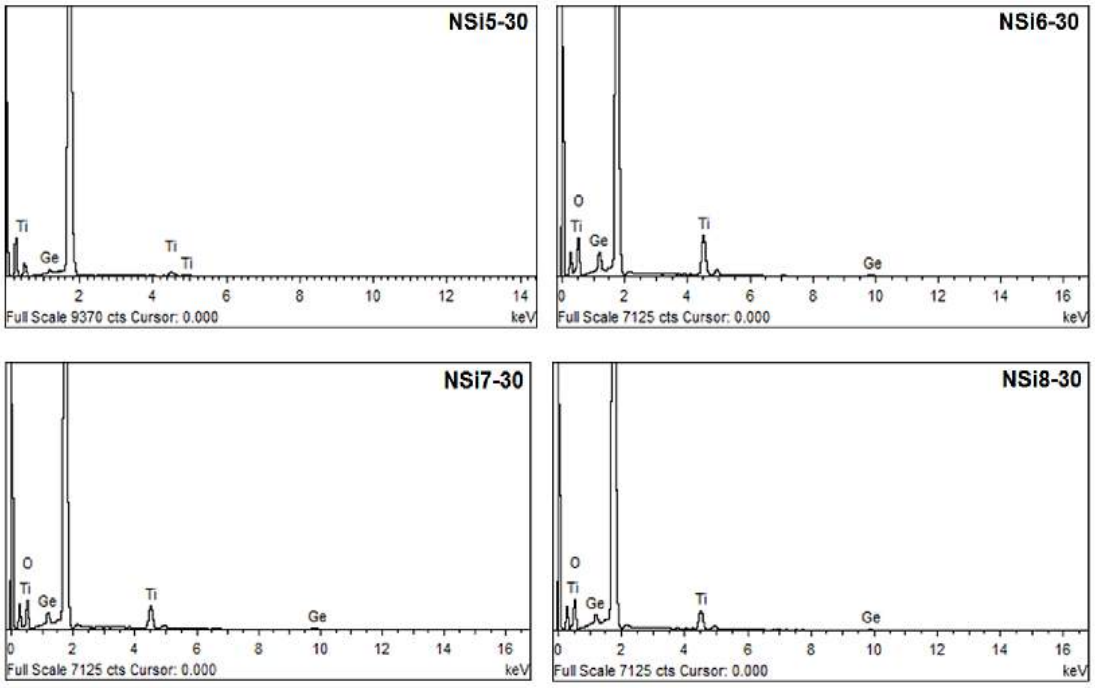

Figure 3.5: EDX spectra of thin films deposited on n-type Si substrate

EDX spectra of thin films deposited on p-type Si (111) substrate are shown in Fig 3.6. Peaks related to Ge, Ti and O can be clearly observed in all the samples.

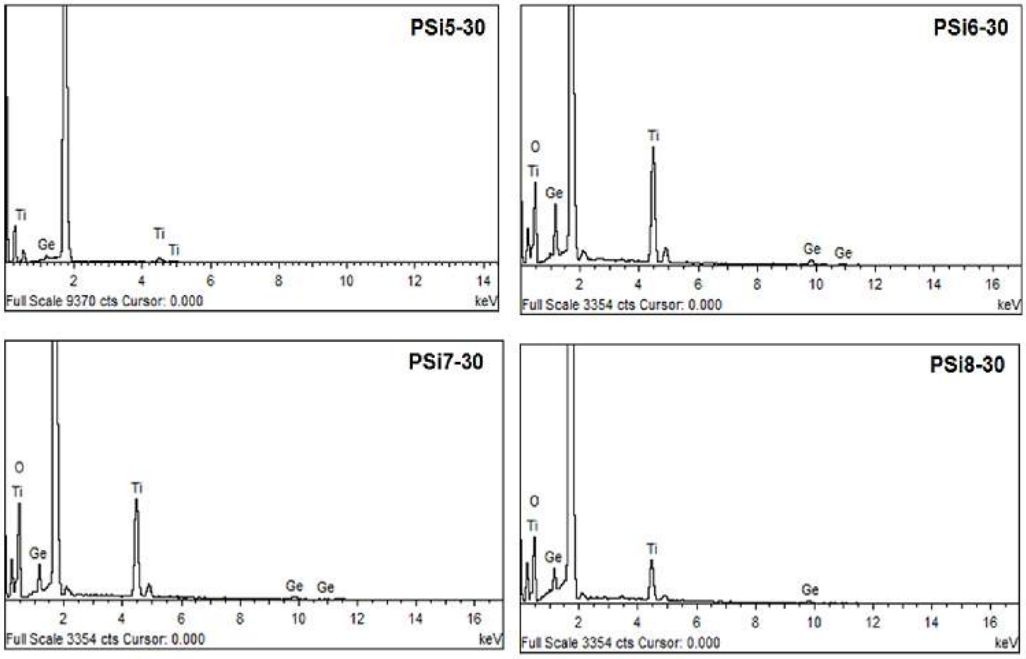

Figure 3.6: EDX spectra of thin films deposited on p-type Si substrate

Ge concentration goes on decreasing as target-substrate separation is increased for thin film growth (Table. 3.4). Atomic Percentage of Ge in thin films is described in the table below:

Table 3.4: Atomic % concentration of Ge in thin films on N and P -type substrate.

Sample Code	Target-substrate separation 'X' (cm)	Atomic Concentration (%)
NSi5-30	5	25.3
NSi6-30	6	2.6
NSi7-30	7	1.9
NSi8-30	8	0.9
PSi5-30	5	25.1
PSi6-30	6	2.9
PSi7-30	7	2.3
PSi8-30	8	0.89

It is clear that thin film deposited with same target-substrate separation on n-type and p-type Si wafer show similar Ge concentration. Which shows that constant stoichiometry for deposition at a specific target-substrate distance was achieved.

Although all the films were grown by using the target with 20% Ge (atomic %) and Ge concentration in thin films grown at a substrate placed at larger distance decreases which is due to the heavier ionic mass of Ge (Eq. 1.15).

Ge has a lower ablation threshold due to which it will be ejected with higher velocity as compared to TiO_2 ions but they decelerate at a higher rate due to heavy ionic mass. Another thing which is very important is that Ge concentration in thin films at X=5 is 25% which is 5% larger as compared to the Ge concentration in target. This is because Ge in this region is back scattered by multiple collisions with ionic species drifting away from target [144].

Composition of single, di and tri-layered thin films deposited on n-type Si (100) substrate at X=6 were also calculated through EDX. The EDX spectra of the films is shown in Fig. 3.7. Measured Ge concentrations are also tabulated (Table 3.5). Sharp peak related to Si wafer is observed around 1.8 KeV. Ge, Ti and oxygen are also identified in all the thin films.

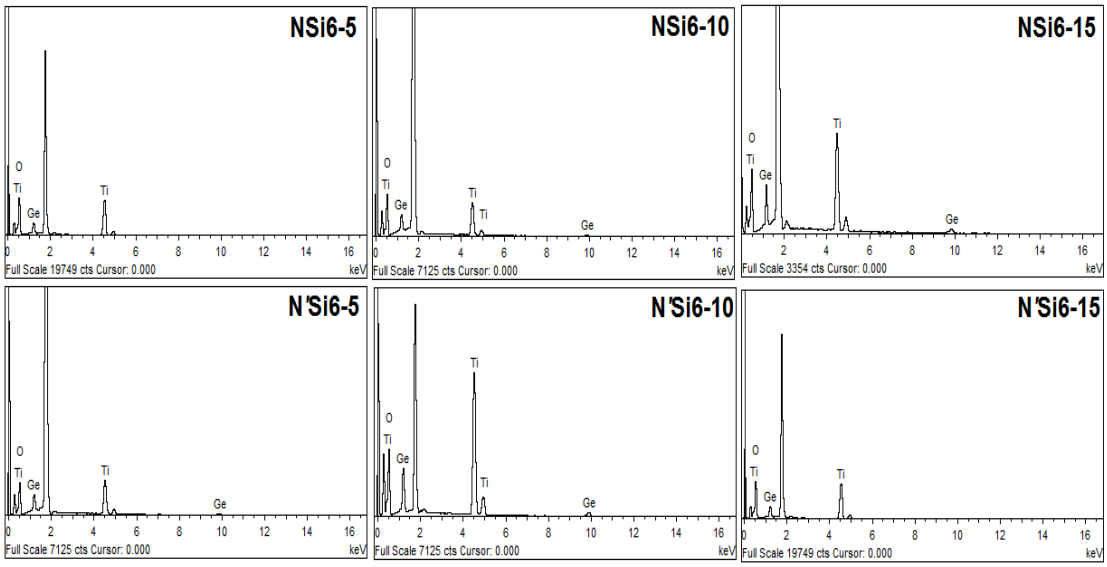

Figure 3.7: EDX spectra of thin films deposited on polished and unpolished Si wafers

Ge concentration is almost constant in all the thin films deposited at X= 6 for single, di and tri layered thin film, where each layer was deposited for 5 minutes (Table. 2.3 and Fig. 2.9). It is therefore clear stoichiometry control has been achieved in thin film deposition by pulsed laser deposition.

Table 3.5: Ge concentration in films deposited on n-type polished and unpolished Si wafer.

Sample Code	Ge concentration
NSi6-5	2.54
NSi6-10	2.53
NSi6-15	2.55
N´Si6-5	2.52
N´Si6-10	2.53
N´Si6-15	2.55

It is clear that all the samples contain Ge which is least visible in XRD therefore composite thin film formation could not be verified in all the films. Therefore all the samples were characterized through Raman spectroscopy.

Elemental distribution was observed in all samples to be uniform i.e. Ti, Ge and O were uniformly distributed during deposition as shown in Fig. 3.8.

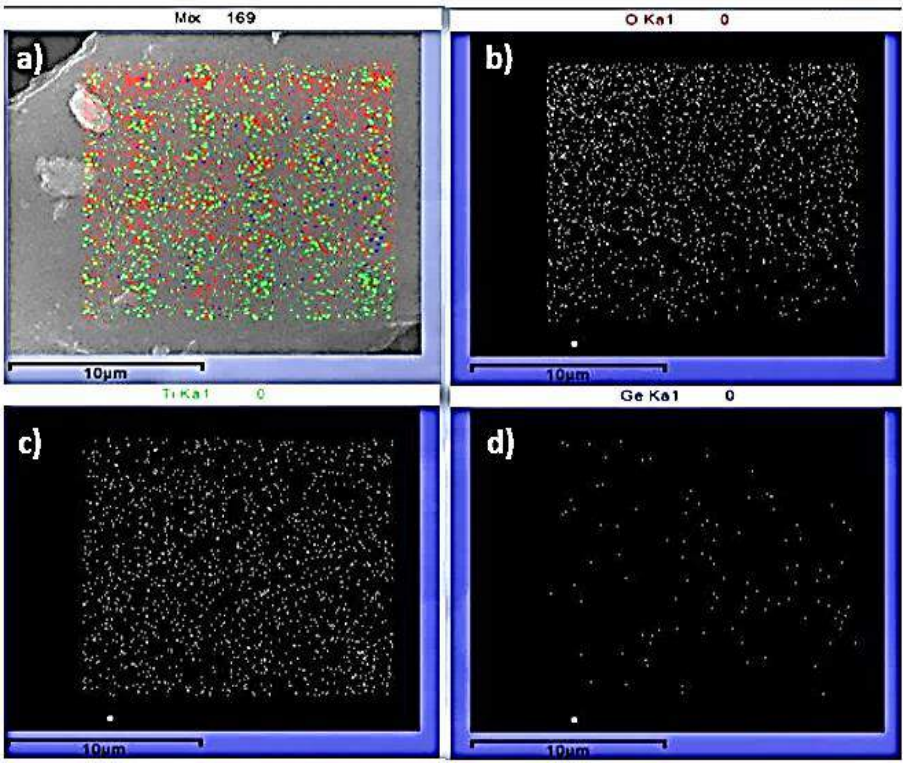

Figure 3.8: Elemental distribution as observed throuh SEM (EDX) analysis (a) distribution of all elements Oxygen (Red), Ti (Green) and Ge (blue) and Distribution of (b) oxygen (c) Ti and (d) Ge in films grown at X= 5 cm on polished n-type Si.

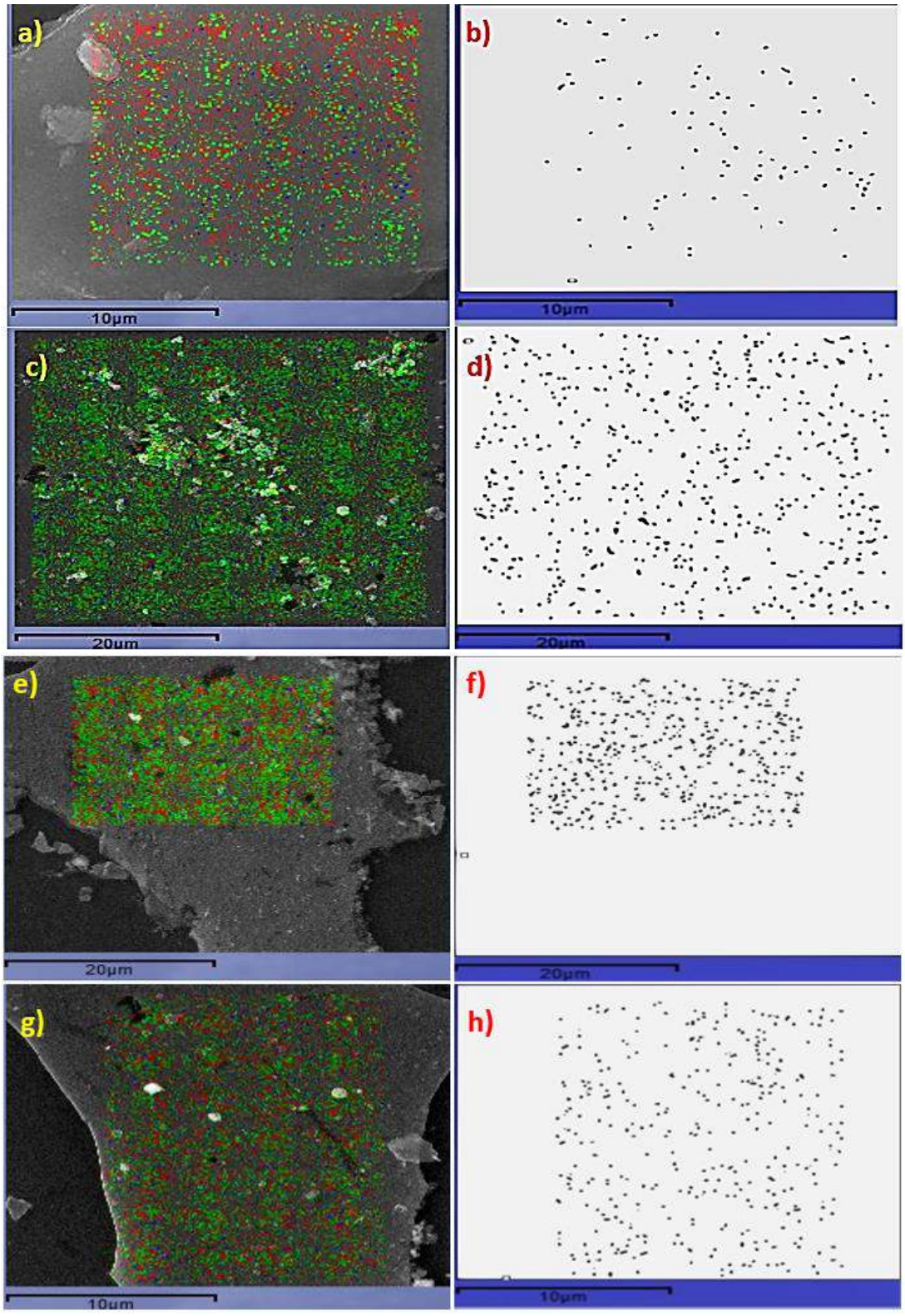

Figure 3.9:Distribution of all elements (on left) and Ge (on right) in thin films deposited on n-type polished Si substrate at a target-substrate distance (a&b)5, (c&d) 6 cm, (e&f) 7 and (g&h) 8 cm.

Ge distribution in thin films was also investigated through elemental mapping (area scan) in EDX is shown in films deposited on polished n-type Si as shown in Fig. 3.9

Thin films deposited on p-type substrate have shown similar behaviour EDX elemental maping of one of sample deposited at X=8 cm is shown in Fig. 3.10.

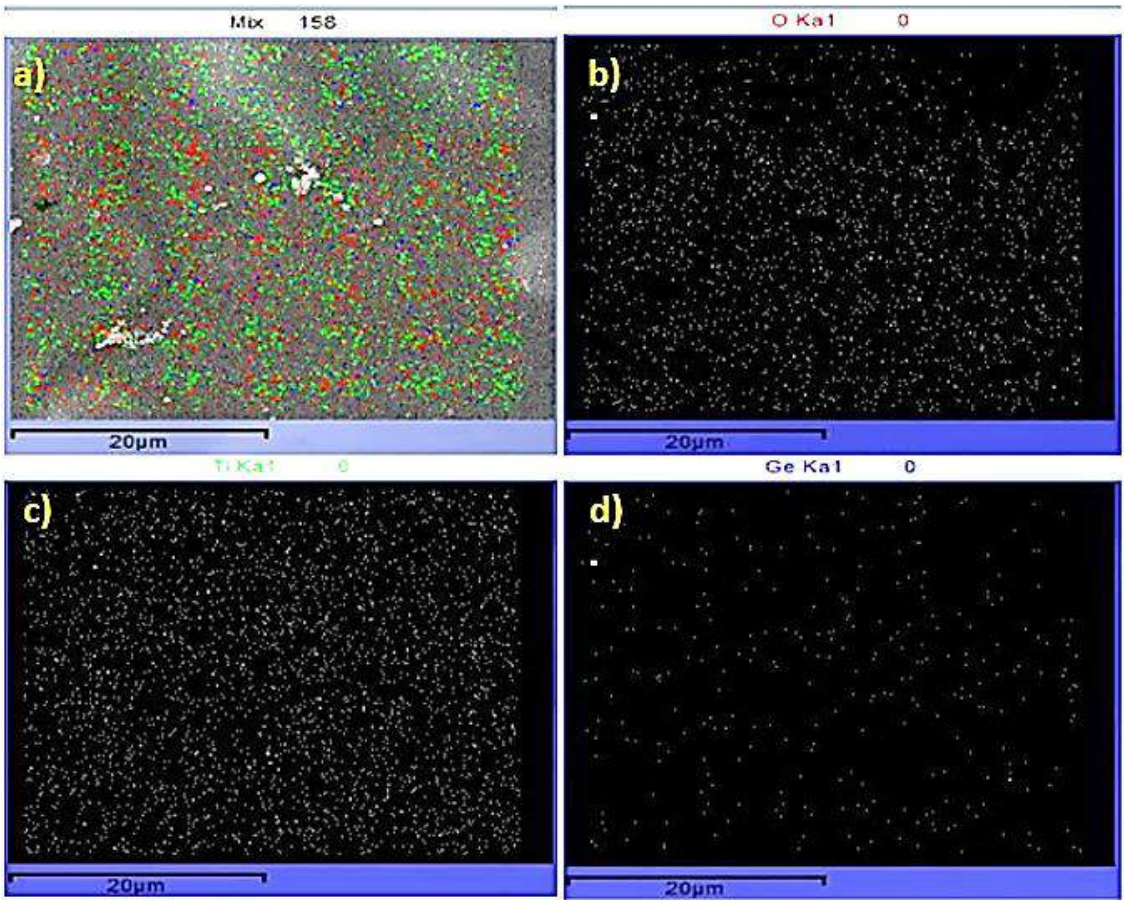

Figure 3.10: Elemental distribution as observed throuh SEM (EDX) analysis (a) distribution of all elements Oxygen (Red), Ti (Green) and Ge (blue) and Distribution of (b) oxygen (c) Ti and (d) Ge.

Single double and triple layered TiO_2-Ge thin films deposited on n-type polished and unpolished Si substrate were also studied for Ge distribution and it was observed that Ge was almost evenly distributed in thin films. SEM micrographs are shown in Fig. 3.11.

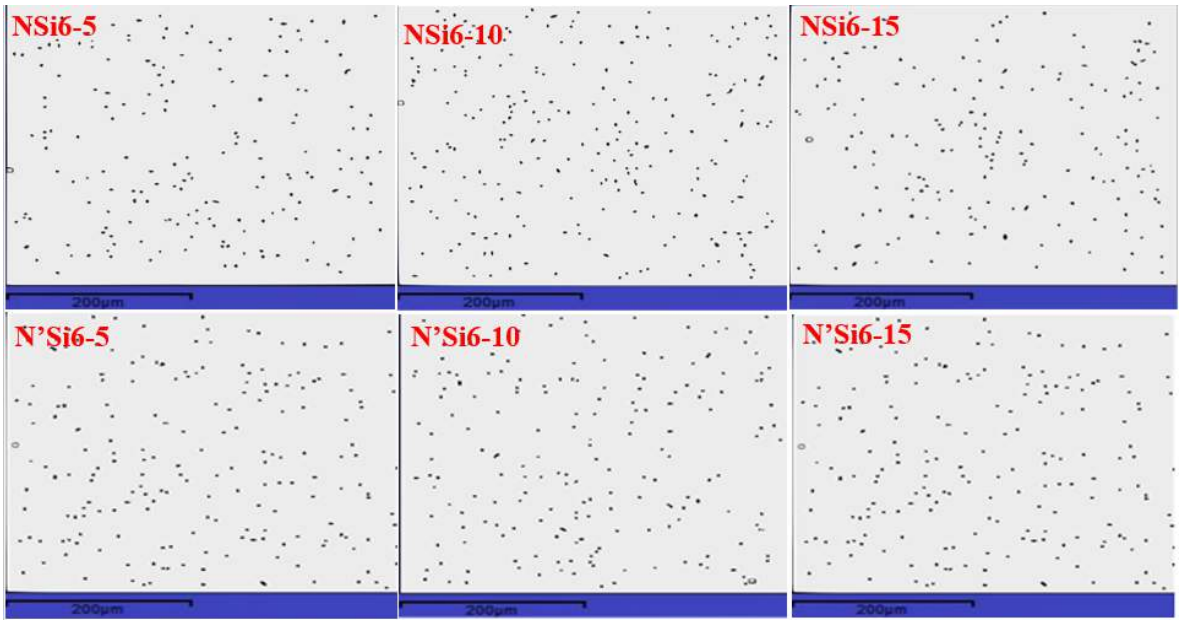

Figure 3.11: Distribution of Ge in single (N& N'Si6-5), doble (N& N'Si6-10) and tri-layered (N& N'Si6-15) films deposited on polished (first row) and unpolished Si substrate(second row).

3.3 Raman Spectroscopic Studies.

All the samples fabricated were studied optically to identify the molecules through their Raman vibrational studies. Especially Ge was the main concern to investigate whether it was doped (in tetragonal structure of TiO_2) or existing in composite form (in its cubic structure).

Raman spectra of the thin films shows Anatase, rutile and brookite crystalline forms of TiO_2 and Ge in its pure form, observed in various peaks in Fig. 3.12-3.15. Raman spectra is mass dependent, as substrate is quiet thick as compared to thin film. Therefore, a very sharp and intense peak is observed around 520 cm^{-1} related to Si substrate [185] as compared to TiO_2 and Ge vibrational peaks. Other peaks are visible when the spectra are rescaled/ zoomed while scaling out Si vibrational peaks as shown in all Raman spectra (Fig. 3.12-3.15)

Bulk rutile TiO_2 has four Raman active vibrational modes (B_{1g} + $2E_g$ + A_{1g}) at 143, 235, 447 & 612 cm^{-1}[183]. Similarly, six Raman active modes (A_1g + $2B_1g$ +3Eg) of anatase phase of TiO_2 appear at 144, 197, 399, 513, 519 and 639 cm^{-1} [183] whereas, Ge in its cubic structure shows Ge-Ge vibrations around 300 cm^{-1} [183] tetragonal Ge

vibrational peak is observed around 260 and 280 cm^{-1} [186]. Brookite has seven A_{1g} Raman active modes at 125, 152, 194, 246, 412, 492 and 640 cm^{-1}[187].

Peaks related to Ge in cubic structure are observed around 300 cm^{-1} in all the thin films whereas Ge was observed through XRD in few thin films which may be attributed to better signal to noise ratio in Raman spectroscopy as compared to XRD [188]. Ge has not been doped in TiO_2 i.e. Ge shows vibrational modes related to cubic structure (vibrational peaks observed around 300 cm^{-1}) not to tetragonal structure (vibrational peaks observed around 260 and 280 cm^{-1}) which would have been dominant in case of doping. Therefore composite nature of TiO_2-Ge thin films has been confirmed by Raman spectroscopy.

Thin films deposited on N and p-type Si substrate at target-substrate distance (X) 5, 6, 7 and 8 cm were analysed through Raman spectroscopy as shown in Fig. 3.12 and 3.13 Thin films deposited at X=5,6,7 and 8 are labelled as a,b,c and d in spectra respectively.

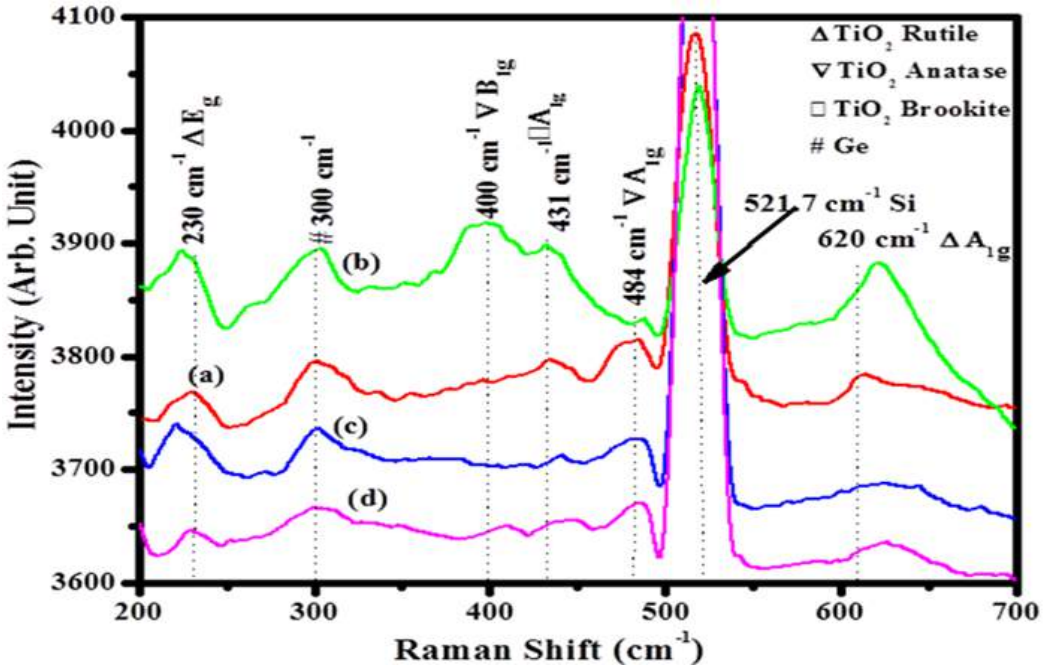

Figure 3.12: Raman Spectras of thin films deposited on n-type Si substrate at a target-substrate seperation i.e (a) 6 cm, (b) 6 cm, (c) 7 cm and (d) 8 cm.

Raman spectra of thin films deposited on n-type Si substrate (Fig. 3.12) reveals that peaks related to Ge in cubic structure are observed around 300 cm^{-1} in all the thin films whereas Ge was not observed through XRD of all thin films except the film deposited at X=8 cm which could be due to better signal to noise ratio in Raman spectroscopy as

compared to XRD [188].

Peaks related to E_g and A_{1g} Raman active modes of rutile TiO_2 can be observed around 230 and 620 cm^{-1} in all thin films. Peaks related to E_g active mode of rutile TiO_2 are shifted to lower wave number (Red shift) as compared to bulk Raman peaks in all thin films containing except thin film deposited at X=5cm, containing 25.3% Ge.

Blue shifted peaks, related to A_{1g} active modes of rutile TiO_2 are evident in all samples (Fig. 3.12 a-d) as compared to peak positions observed in bulk material. Raman peak related to B_{1g} and A_{1g} vibrational mode of anatase TiO_2 are observed around 400 (only in sample b) and 484 cm^{-1} (in all samples). Blue shift in Raman peaks related to B_{1g} Raman mode is observed in comparison to bulk Raman peaks in thin films containing 0.9 % Ge whereas no shifting is observed in thin films deposited with concentration of 25.3 % Ge. Blue shift in raman peaks is associated to the reduction in bond length depicting quantum confinement effect [189].

Red shift in Raman peaks related to A_{1g} active mode of anatase TiO_2 are observed as compared to peaks observed in bulk. Presence of brookite TiO_2 is confirmed by blue shifted peak around 431 cm^{-1} in sample a and b as compared to bulk brookite peak appearing at 412 cm^{-1}.

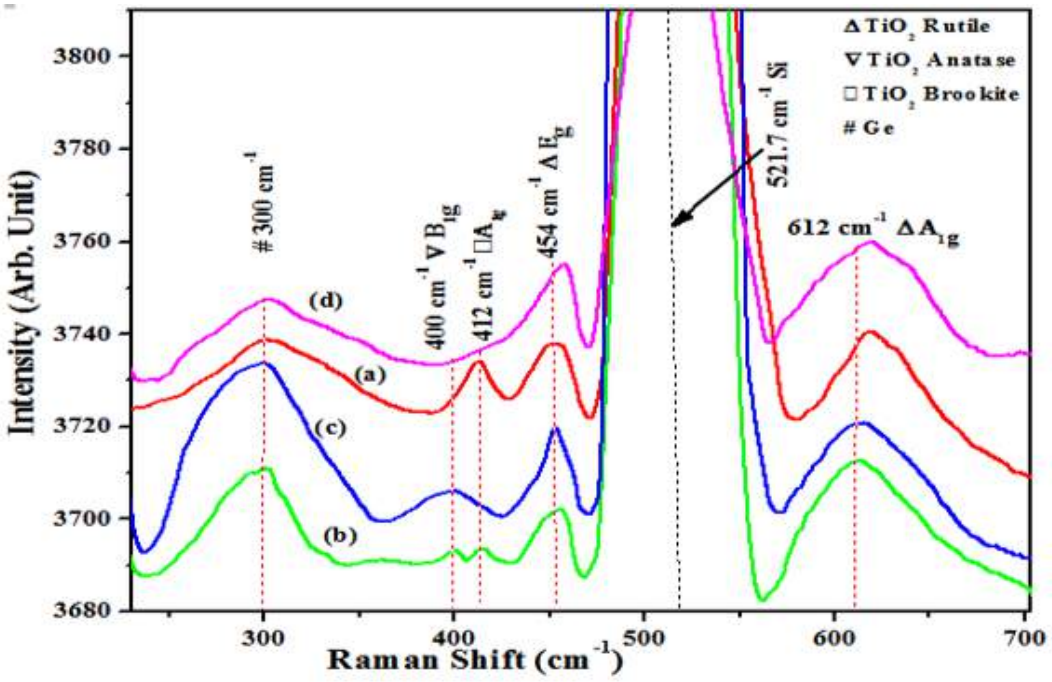

Figure 3.13: Raman Spectra of thin films deposited on p-type Si substrate at a target-substrate seperation i.e (a) 6 cm, (b) 6 cm, (c) 7 cm and (d) 8 cm.

Figure 3.13 shows the Raman active modes of rutile, Anatase TiO_2 and Ge. Among the four Raman active modes of rutile TiO_2 only two vibrational modes at 454 and 612 cm^{-1} are exhibited in all thin films. Peak related to Eg active mode of rutile TiO_2 is shifted to higher wave number 454 cm^{-1} (blue shift) as observed in bulk rutile at 447cm^{-1}.

Maximum blue shift is observed in this vibrational mode in thin films deposited at X=8cm (containing 0.9 Ge). Peak related to A_{1g} active Raman vibrational mode of rutile TiO_2 (appearing at 612 cm^{-1}) show no shift except thin film deposited at X=8 cm (Fig. 3.13d) which shows a blue shift.

Raman active mode related to anatase phase is identified by a peak around 400 cm^{-1} observed in thin film deposited at X= 6 and 7cm [183]. Raman active modes of brookite TiO_2 are observed in thin films deposited at X= 5 and 6 cm at 412 cm^{-1}. One Raman active mode related to rutile TiO_2 which appeared around 230 cm^{-1} in thin films deposited on n-type substrate is not present in thin films deposited on the p-type Si substrate. These structural changes are associated to the misfit factor present in thin film and substrates. So the different crystalline forms observed in thin films are not only dependent on target-substrate distance but also on substrate orientation. As n and p-type substrates are single crystals having (100) and (111) orientation which thus by results in the formation of different structures and strains (explained in detail in topic 3.1) resulting in peak shifting in Raman spectra.

Single (5 min), di (10 min) and tri-layered (15 min) TiO_2-Ge thin films deposited on polished and unpolished n-type Si (100) wafers were analyzed through Raman spectroscopy as shown in figures 3.14 and 3.15. Various Raman active modes have been observed related to Anatase, Rutile TiO_2 and Ge. Peak indexed as Si have been identified around **520** cm^{-1} **[185]** in all the samples as observed in previous samples (Fig. 3.12 and 3.13)**.**

Tri-layered thin films deposited on polished n-type Si substrate (Fig. 3.14 15 min) exhibit B_{1g} and E_g Raman active modes of vibration for rutile TiO_2 at 395 and 633 cm^{-1} [183]. Peaks related to these modes of vibrations show a mild red shift associated to increase in bond length. Raman vibrations related to cubic Ge are observed at 300 cm^{-1} [185] in all thin films.

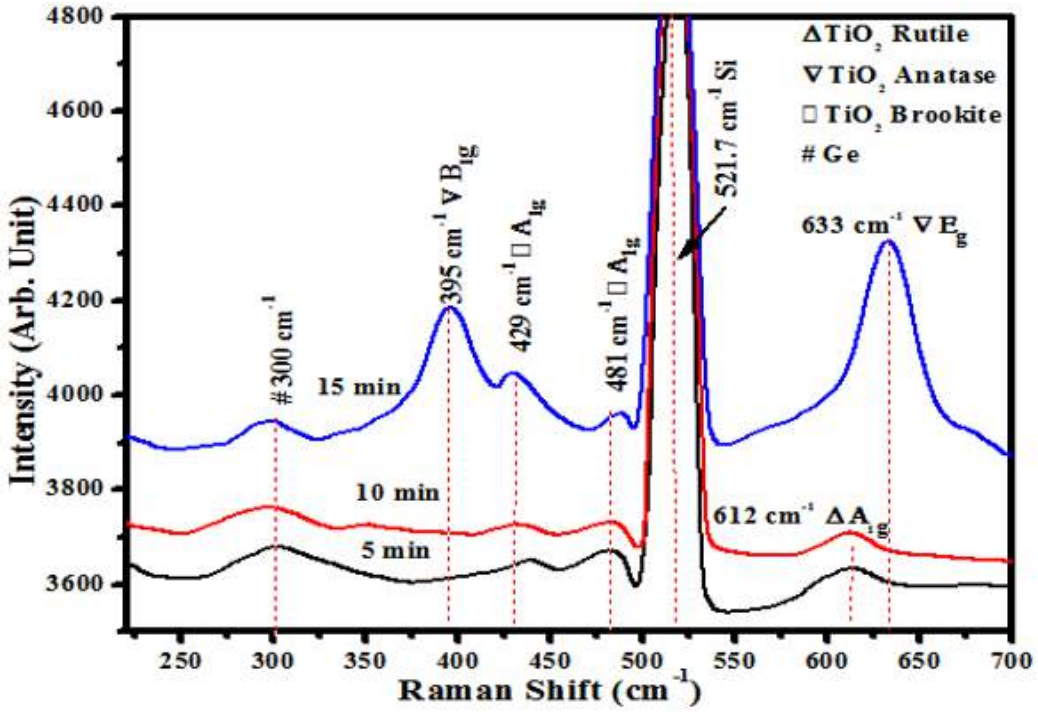

Figure 3.14: Raman spectra of TiO_2-Ge composite film deposited on polished n-type Si wafer as single layer (5 min), di-layer (10 min) and trilayer (15 min).

Peaks related to A_{1g} vibrational mode of brookite TiO_2 are observed at 429 and 481 cm^{-1} in all the samples. Peaks observed in all samples around 429 cm^{-1} are blue shifted as compared to the peak observed in bulk at 412 cm^{-1}. This blue shift is associated to the reduction in bond length formed in nanostructures exhibiting quantum confinement effect [189]. Whereas peak observed at 481 cm^{-1} is red shifted as compared to peaks observed in bulk brookite (499 cm^{-1}). Peak related to A_{1g} vibrational mode of Anatase TiO_2 phase is observed in single and di-layered thin films [188].

Single di and tri-layerd thin films deposited on unpolished Si wafers were studied for their properties through Raman spectroscopy (Fig. 3.15). Vibration related to cubic Ge has been identified at 300 cm^{-1} [185], which shows a mild blue shift as thin film thickness increases. Brookite and rutile TiO_2 is identified at 437 and 622 cm^{-1} related to A_{1g} mode of vibrations [183] in all samples. Peaks related to this mode are blue shifted as compared to bulk TiO_2 whereas maximum shifting is observed in tri-layered thin films

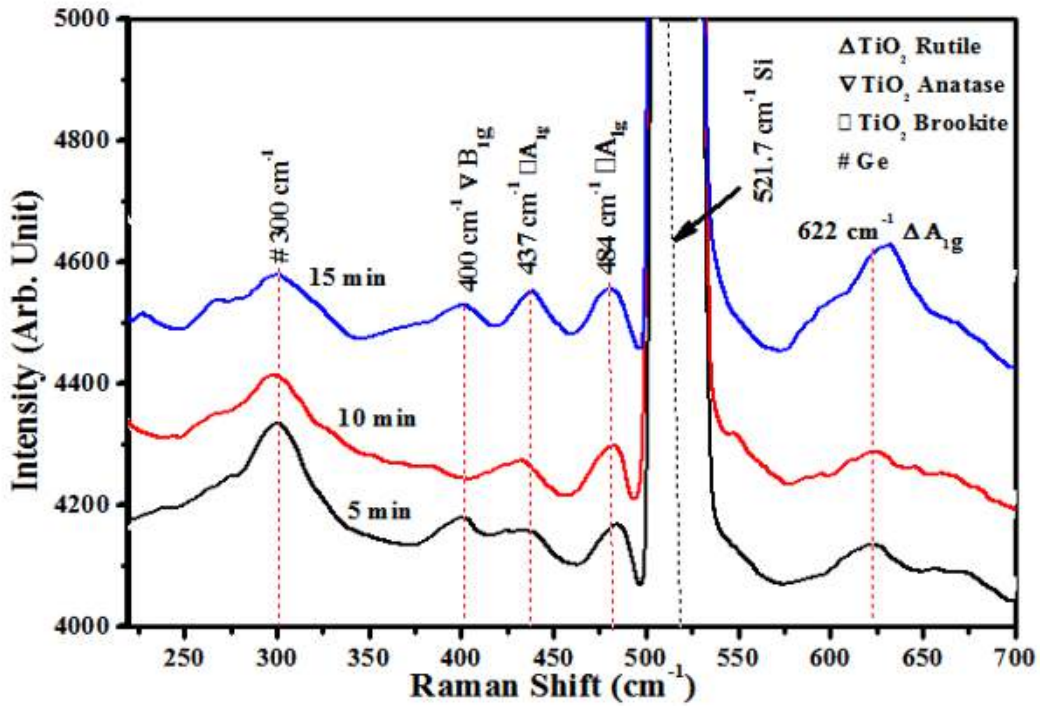

Figure 3.15: Raman spectra of TiO_2-Ge composite film deposited on unpolished n-type Si wafer as single layer (5 min), di-layer (10 min) and trilayer (15 min).

. Peak related to B_{1g} mode of anatase TiO_2 [183] has been observed around 400 cm^{-1} in tri-layered film only. An overall view shows three raman active peaks observed around 300, 440 and 620 cm^{-1} exhibit blue shift related to quantum confinement [189] whilst the peak observed around 400 shows no shift [188] respectively.

It is clear from the Raman spectroscopic studies that TiO_2-Ge thin films are composite in nature. As Ge vibrations have been observed in all the samples related to cubic Ge and vibrations related to TiO_2 are related to tetragonal structure respectively. Neither any vibrational modes related to other to compound of TiO_2 or Ge were found in Raman vibrations. Thin films deposited for a shorter time show development of less stable TiO_2 allotropes. As deposition time increases more stable phases of TiO_2 grow i.e. intense peaks related to rutile TiO_2 are observed. As well as blue shift in Raman vibrational mode is related to quantum confinement in composite films, which can then result in inter-band transitions from hyperfine structures in thin films. These transitions can be verified by multiple transitions in UV vis and photoluminescence analysis of thin films.

It is observed that deposition time, target-substrate distance and substrate orientation

also effect the crystallinity in thin films. In addition better crystallinity is seen for longer deposition time whereas Ge concentration decreases as target-substrate distance increases. Ge is distributed uniformly in all films as observed in SEM elemental mapping

Peaks related to Ge were least observed in XRD spectra but EDX scan confirms the presence of thin films, therefore it was difficult to conclude that whether Ge was doped or it makes a composite with TiO_2. Since Raman spectroscopy affirms the presence of cubic crystalline structure of Ge rather than tetragonal structure (related to TiO_2), it certifies the composite nature of thin films. Therefore depending on difference in crystallinity, optical and electrical response will also be effected as explained in the next chapters.

Chapter 4

4 Optical Studies

4.1 UV Reflectance Spectroscopy.

UV- Vis reflectance of thin films was carried out to find direct and indirect absorption transitions, which is further related to their electronic and electrical properties. Absolute reflectance spectra was recorded as obtained from thin films which was further processed through Kubelka Munk function to calculate the absorbance, direct transitions and indirect transitions using eq. 1.25 and 1.26 (For Ref see topic 1.5.4 in Chapter 1). Bandgap variation was studied for its dependence on the substrate. Growth of different allotropes of TiO_2 in thin films, lattice strain and defects/ dislocation density.

UV-Vis reflectance spectra and absorbance of TiO_2-Ge thin films deposited on n and p-type Si substrate at target-substrate distance (X); 5, 6, 7 and 8 cm are shown in the Fig. 4.1 and 4.4 respectively. Spectra and graphs related to thin films deposited at X= 5, 6, 7 and 8 cm are labelled as a, b, c and d.

Maximum reflectance can be observed in thin films deposited at X= 8 cm (Fig 4.1 A(d)) on n-type Si, whereas minimum reflectance observed in thin films deposited at X=6 cm (Fig 4.1 A(b)). Thin films deposited at X=5 and 7 cm show reflectance nearly in the same range. Each film shows different reflectance spectrum. Thin film having 25.3% Ge concentration (Fig. 4.1 A(a)) shows maximum reflectance around 458 nm, this reflectance decreases to a value of 10% at 800 nm. Thin film having 2.6% Ge concentration (Fig 4.1 A (b)) shows minimum reflectance and that with 1.9 % Ge concentration (Fig 4.1 A (c)) shows three prominent reflectance peaks around 382, 494 and 682 nm. Film with 0.9% Ge have maximum reflectance around 402 and 560 nm (Fig 4.1 A (d)).

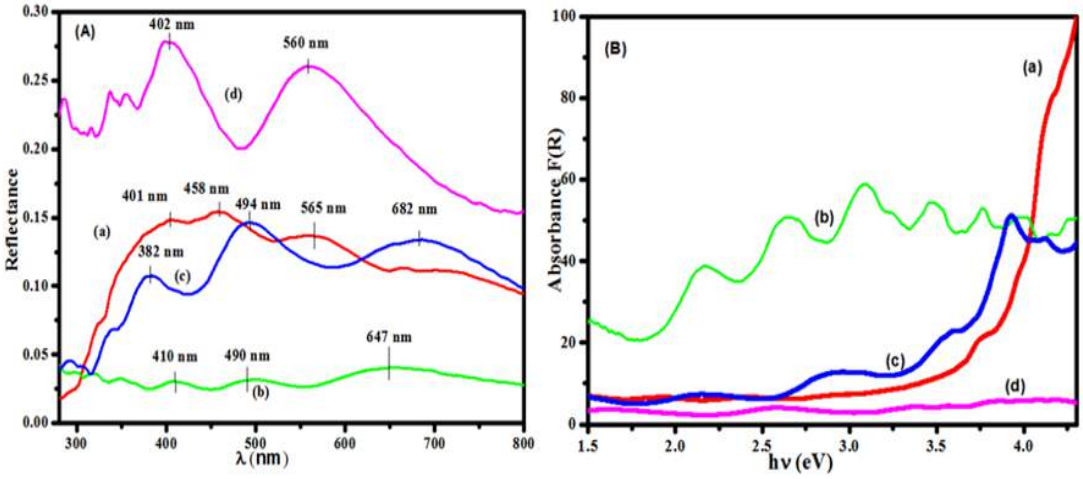

Figure 4.1: Reflectance (A)and absorbance spectra F(R)(B) of thin films deposited on n-type Si substrate at varius X= (a) 5 cm, (b) 6 cm, (c) 7 cm and (d) 8 cm.

If we look at the absorbance spectra of thin films deposited on n-type Si substrate (Fig 4.1 B), it is very clear that absorbance shows an inverse behaviour as compared to the reflectance. That is the samples with minimum reflectance shows maximum absorbance and vice versa. Minimum variation in absorbance is observed in spectral range from IR to UV region in thin film deposited at X=6 cm (Fig. 4.1 B(b)). Thin films deposited at X= 5 and 7 cm (Fig. 4.1 B(a and c)) shows similar absorbance below 4eV. Maximum absorbance to the electromagnetic radiation having energy greater than 4 eV is observed in thin film deposited at X=5 cm which is attributed to TiO_2 quantum dots (E_g ~ 3.3 eV) [190] although it has maximum Ge concentration as TiO_2 band gap lies in UV region.

All the thin films deposited on n-type polished Si wafer for 30 minutes at X=5, 6, 7 and 8 cm show multiple absorption transitions in the spectral range IR to UV region as shown in Fig. 4.2 (a-d). Multiple absorption peaks are visible in sample b (X=6) with a spread from visible to UV range. These transitions can be related to the energy levels introduced with in bandgap associated to strains and dislocations caused by lattice mismatch of TiO_2 with Ge and Si substrate [129, 191]. Presence of dislocations has been found through XRD measurements. So we have attained enhanced absorption efficiency for TiO_2-Ge composite film deposited at X=6 cm. Fig. 4.2 (a, c) show direct band gap transition in IR, visible and UV region for films with 25% and 1.9 % Ge concentration.

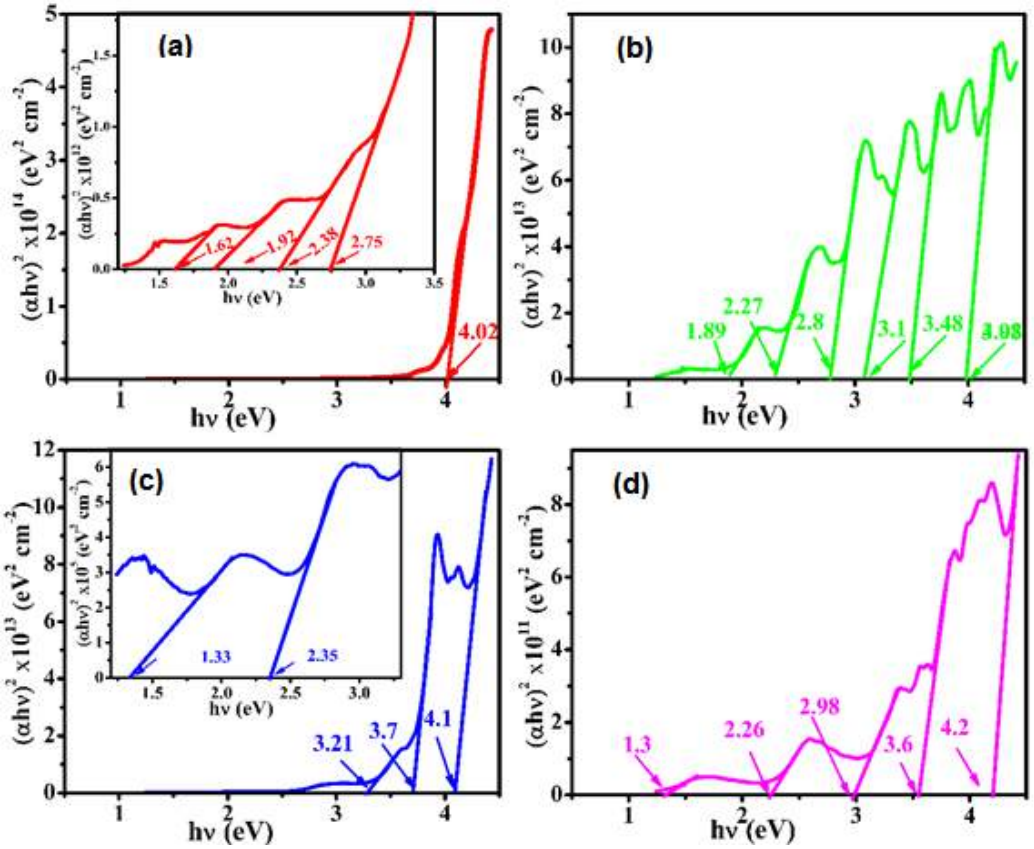

Figure 4.2: Direct transitions of thin films deposited on n-type Si wafers deposited at different target-substrate distance i.e (a) 5 cm, (b) 6 cm, (c) 7 cm and (d) 8 cm and the inset shows the expanded view of transitions in thin films deposited at 5 (a), 7 (b) and 8(d) cm from the target.

Sample (a) with 25% Ge shows a strong transition in the UV range with a band gap 4.02 eV. Thin films contain rutile, anatase and brookite phase of TiO_2 therefore thin films show multiple transitions. An enhancement in band gap cannot be associated to the defect levels. It can be attributed to formation of quantum dots (co-verified by PL spectra of these samples discussed in topic 1.5.6). It has also been reported that the bandgap of Ge lying in the range 2-3 eV is due to the quantum confinement in Ge [192] with crystallite size ranging from 8-14 nm. Samples (c,d) with 1.9 and 0.9% Ge also exhibit transitions varying in a large spectrum from IR to UV range. Though these transitions are weaker as compared to sample (a, b), we can see a systematic trend for direct transitions that as concentration decreases in composite films, their absorption decreases and transition becomes weaker.

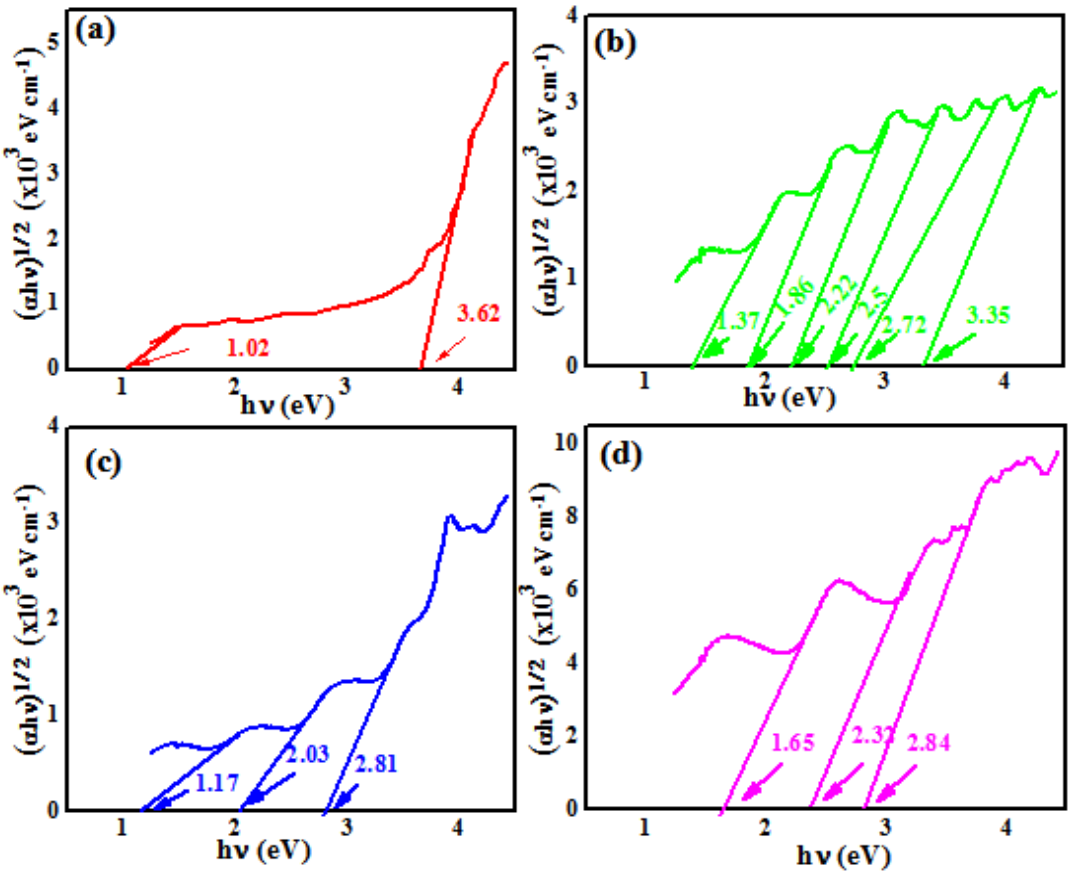

Figure 4.3: Indirect transitions in thin films deposited on n-type Si wafers deposited at different target-substrate distance i.e (a) 5 cm, (b) 6 cm, (c) 7 cm and (d) 8 cm.

Indirect transitions were investigated through the Tauc plot (Fig. 4.3). We noticed that the number of indirect transitions decreases as compared to direct transitions but the absorption transition in general still lies from IR to UV region. Samples (c, d) fabricated at X=7 and 8 cm show no transition in UV range. Again large number of transitions occurs in the sample (b) with 2.6 % Ge.

These multiple absorption transitions from visible to UV range could be associated to defect levels introduced with in the band gap due to heterojunctions created at the boundary of TiO_2 matrix and Ge quantum dots. As Ge has an indirect bandgap lying in IR region (0.6 eV) therefore increase in indirect transitions could be attributed to quantum confinement in Ge nano dots [192] in TiO_2 matrix. Band gap is known to increase quantum mechanically if particle radius reduces below Bohr exciton radius [193, 194]. It can also be estimated that Ge could not be identified in XRD but was identified in Raman spectroscopy, which indicates that Ge crystallites are so small that

they were not identified through XRD but were detected in Raman spectroscopy. Reduction in crystallite size results increases in strain [195] and hence dislocation density increases. Therefore, hetero-structure growth also leads to strains and thus lattice mismatch is observed which plays vital role in band gap warping. Lattice strains therefore lead to the formation of quantum dots by Stranski- Krastanov growth mechanism [191]. Large numbers of transition were observed in thin film (sample b) with 2.6% Ge concentration it can be stated that this sample shows better optical response. We have noticed that intensity of indirect transitions is much smaller as compared to direct transitions. Multiple transitions can also be attributed to the formation of anatase, rutile and brookite phases which have band gaps in visible and UV region. But the transitions in IR and visible region can be associated to Ge.

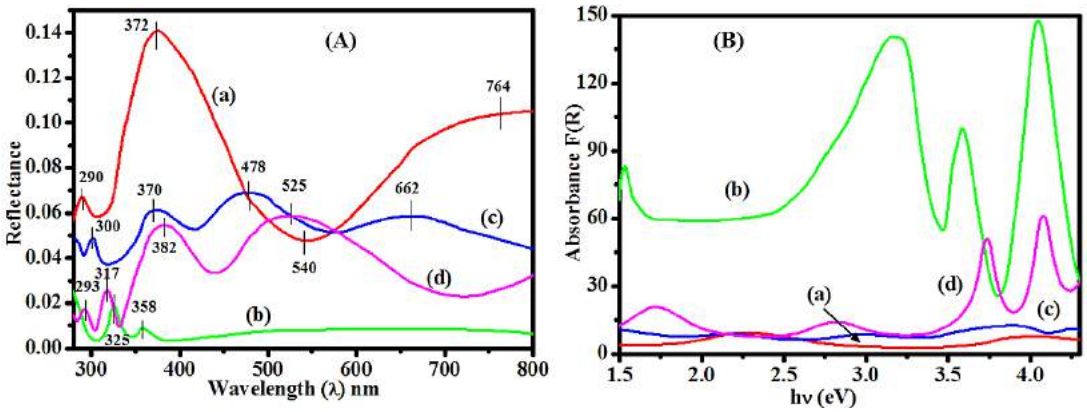

Figure 4.4: Reflectance spectra of thin films deposited on p-type Si substrate at a target-substrate seperation i.e (a) 6 cm, (b) 6 cm, (c) 7 cm and (d) 8 cm

Reflectance and absorbance spectra of thin films deposited on n-type Si substrate is shown in Fig 4.4 (A) and (B).Thin film having 25.6% Ge concentration (Fig. 4.4 A (a)) has 6% reflectance in the spectral region below 325 nm and maximum reflectance of 14% around 372 nm, this reflectance decreases to a minimum value of 5% at 540 nm. It then rises to a higher value of 10% at 764 nm. This film which has a highest reflectance has minimum absorbance i.e. F(R). Thin film having 2.9% Ge concentration shows minimum reflectance (Fig 4.4 A(b)) and maximum absorbance (Fig 4.4 B(b)). Thin film fabricated at X=7 cm, with 2.3 % Ge concentration (Fig 4.4 A(c)) shows reflectance higher than the thin film fabricated at X=6 and 8, containing 2.9 and 0.89% Ge concentration (Fig 4.4 A(b) & (d)) except in the wavelength range 525-575 nm.

Thin film containing 2.3% Ge (Fig 4.4 B(c)) shows higher absorbance as compared to thin films containing 2.9 and 0.89% Ge (4.4 B(b) & (d)).

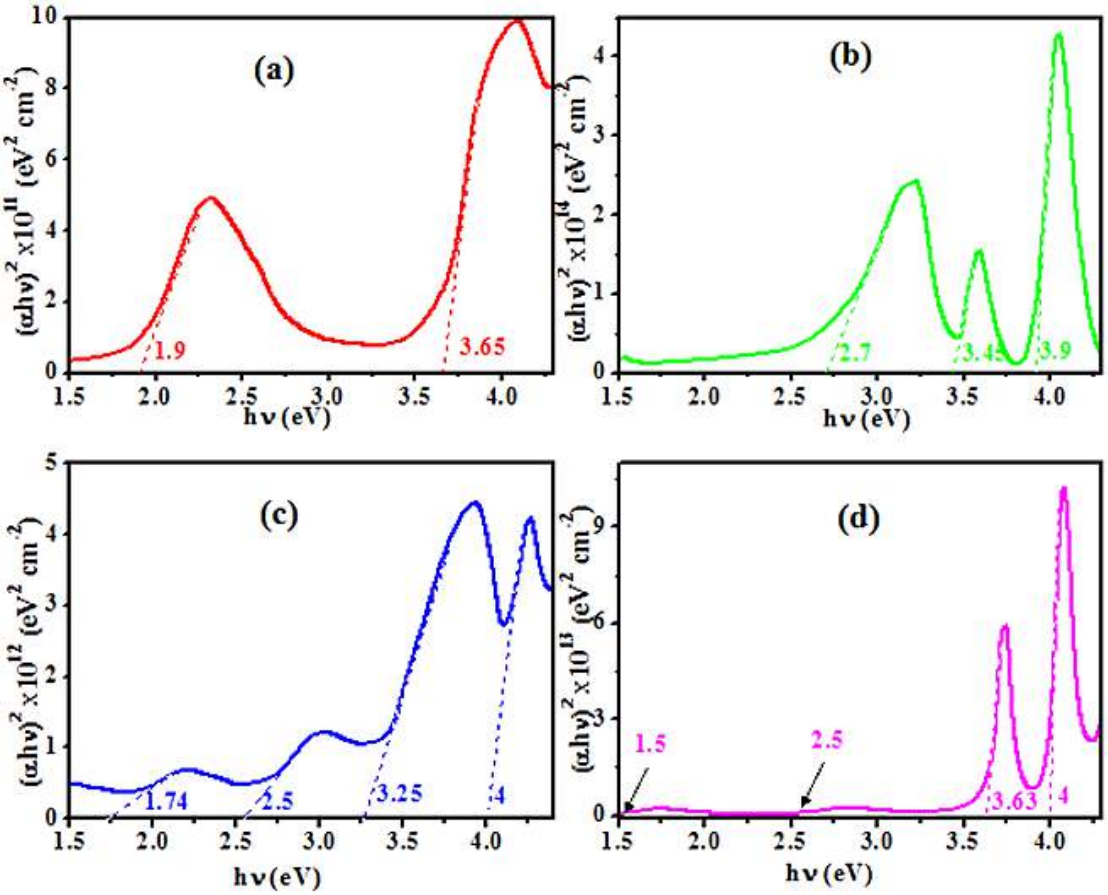

Figure 4.5: Direct transitions of thin films on p-type Si wafers deposited at different target-substrate distance i.e (a) 5 cm, (b) 6 cm, (c) 7 cm and (d) 8 cm. (i) Shows transitions in all the samples.(ii) shows expanded view of transitions in thin films deposited at 5 and 7 cm. (iii) shows the further zoomed image of transitions for samples fabricated at 8 cm.

Direct absorption transitions of thin films deposited on p-type Si substrate are at a target-substrate distance of X= 5, 6, 7 and 8 cm are shown in Fig. 4.5. It can be observed that maximum absorption transitions are observed in thin film deposited at X= 7 and 8 cm (Fig 4.5 c & d), which lie in IR, visible and UV region of electromagnetic spectrum. Rest of samples i.e. thin films fabricated at X=5 and 6 cm show transitions in UV and visible region.

Multiple transitions are also observed in the Tauc plot for indirect transitions of thin films deposited at X= 5, 6, 7 and 8 cm on p-type Si wafer (Fig. 4.6) but the intensity of

these transitions is less as compared to the direct transitions. Indirect transitions observed in IR and visible region are associated to the Ge provided the band gap in visible region is due to quantum confinement in Ge [192].

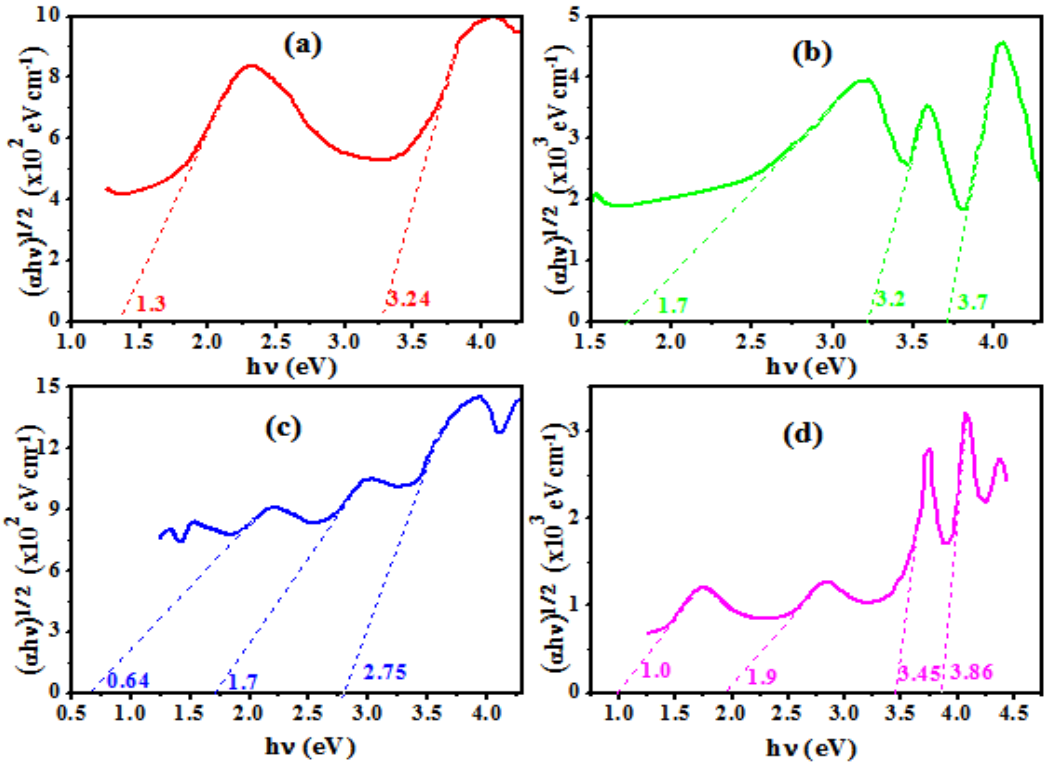

Figure 4.6: Indirect band gap for thin films deposited on p-type Si wafers deposited at different target-substrate distance i.e (a) 5 cm, (b) 6 cm, (c) 7 cm and (d) 8 cm. Image on right side shows expanded view of transitions in thin films deposited at 5, 7.

Direct and indirect transitions observed in thin films deposited on p-type Si wafer (Fig. 4.5 and 4.6) are less intense as compared to the transitions intensity observed in thin films deposited on n-type Si wafer (Fig. 4.5 and 4.6). It can be due the misfit factor present in thin film and the substrates (i.e. n-type 100 and p-type 111) which then results in thin films with different crystallinity. Misfit factor is smaller in thin films deposited on n-type Si substrate therefore strained films are grown on and hence more defects are present in the films. Strain is also attributed to form multi-sized Ge quantum dots which then lead to transitions invisible region. Thin films deposited on p-type Si substrate have a larger misfit factor which therefore curtails the crystalline growth of

nanostructures. Therefore transitions related to quantum confined Ge are least observed i.e in thin films deposited at X= 7 and 8 cm (Fig. 4.5 and 4.6, c & d).

Reflectance spectra and absorbance of single, di and tri-layered TiO_2-Ge composite thin films on n-type polished Si wafers have been shown in Fig. 4.7(a) and (b).

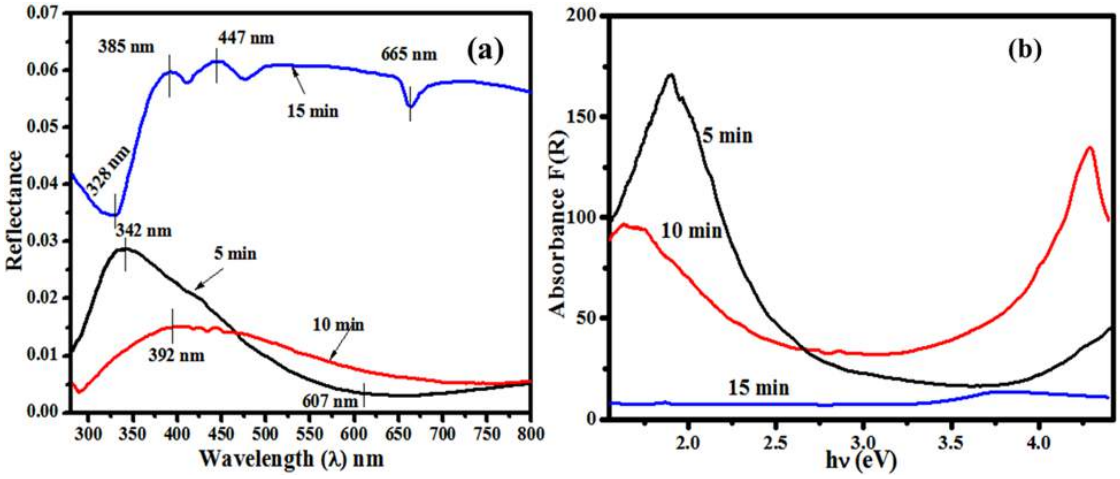

Figure 4.7: Reflectance spectra of TiO_2-Ge composite film deposited on polished n-type Si wafer as single layer (5 min), di-layer (10 min) and trilayer (15 min).

Reflection spectra of single, di and tri-layer of TiO_2-Ge thin film on n-type polished substrate have been shown in Fig. 4.7. The graph shows minimum reflection for the film deposited for ten min as compared to that film deposited for 5 and 15 minutes. Maximum reflectance is observed in tri-layer films. It is clear that maximum variation in reflectance is observed in the range of 300-450 nm in all the samples. It is obvious that the reflectance in thin film deposited for 5 minutes (single-layer) is greater than that for 10 minutes (di-layer) film in the wavelength range 300-470 nm. A reverse of this behavior is observed beyond 470 nm till 800 nm. Reason for minimum reflectance in bilayer film may be associated to amorphous nature of the film as mentioned in the explanation of its XRD. Thin films deposited in 3 layers shows a minimum absorption as compared to other samples which is due to smaller value of n for these samples as shown in fig. 4.15 under ellipsometry analysis.

Reflectance data was used to find direct and indirect transitions by Tauc plot through Kelbuka Munk relation for all the three films as shown in figures 4.8 & 4.9..

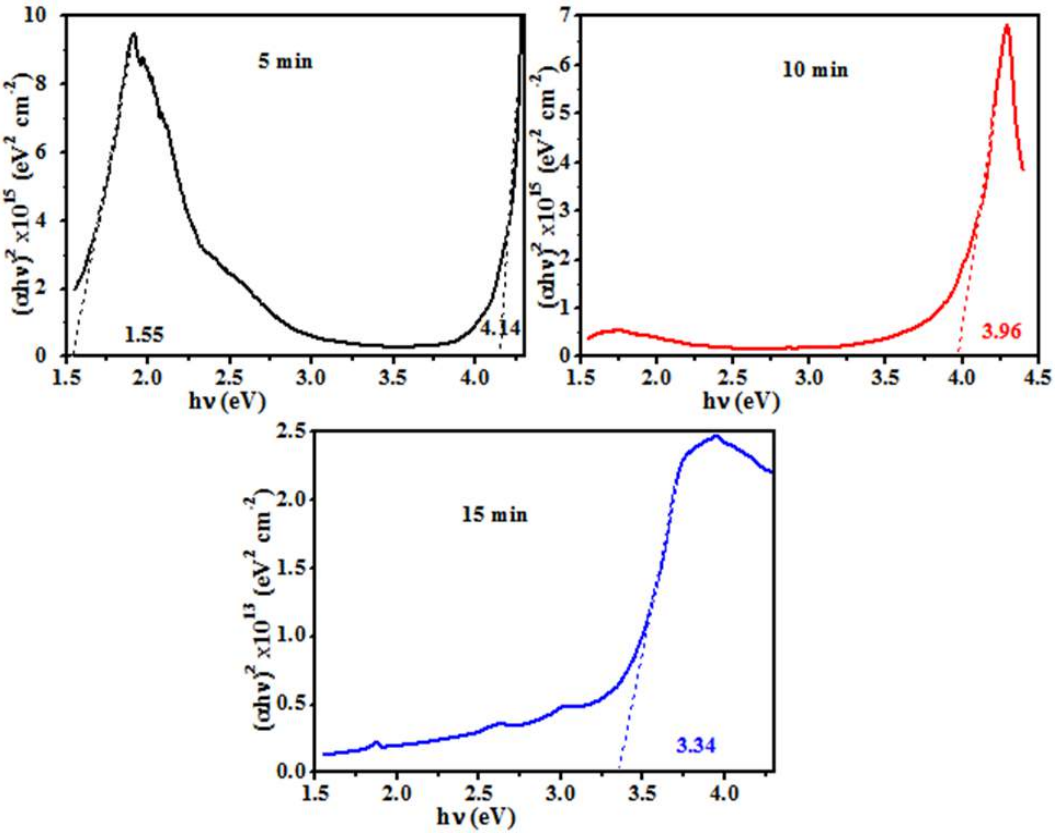

Figure 4.8 : Direct transitions of single layer (5 min), di-layer (10 min) and trilayer (15 min) TiO_2-Ge composite film deposited on polished n-type Si wafer.

Single layer film shows absorption transitions in the IR and UV range i.e. direct. Transitions around 1.55 and 4.14 eV and indirect transitions around 0.88 and 3.84 eV. Bilayer film shows direct transitions around 3.96 eV and indirect transition around 3.31 eV. Tri-layer also shows direct transitions in the UV range i.e. around 3.34 eV. But indirect transitions are observed in visible range around 2.45 eV which may be associated to defects in strained thin film as shown in Table 3.3.

Single layer of TiO_2-Ge composite shows the shifting of band gaps of Ge and TiO_2 to slightly higher values as compared to bulk. Which is an indicative of formation of TiO_2 and Ge nanostructures without quantum confinement.

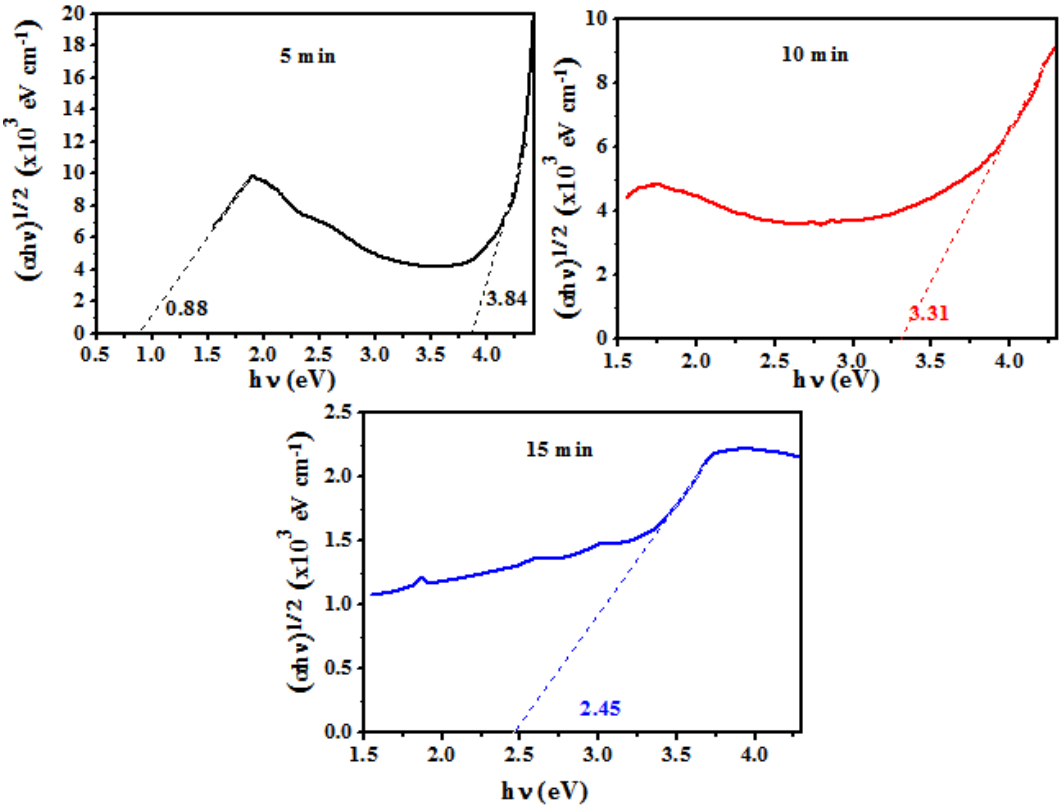

Figure 4.9: Indirect transitions of single layer (5 min), di-layer (10 min) and trilayer (15 min) TiO_2-Ge composite film deposited on polished n-type Si wafer.

Bilayer growth resulted in culmination the Ge crystalline structure as can be seen in the XRD too (Fig. 3.3) therefore the band gap associated to Ge can-not be observed in bilayer film. Tri-layer film has been observed to favour the crystalline growth of nanostructures again. The indirect band gap in tri-layered film around 2.45 eV can be associated to the strain but not to quantum confinement as photoluminescence spectra does not support it (Fig. 4.19 a).

Reflectance spectra for films deposited on n-type unpolished Si wafer were recorded as shown in Fig. 4.10 Maximum reflectance of 7.5% is observed in the di-layer around 375 nm which decreases linearly till 575 nm to a reflectance of 1%. it then slowly decreases for light of wavelength 637 nm and then gradually rises to 10% for light of wavelength 800 nm. Minimum reflectance is observed in tri-layered thin film (labelled as 15 min) in the reflectance range of 0.4-1%. Single-layered thin film shows an increasing trend in reflectance from 1.5-5% with a minima around 314 nm. An inverse relationship can be observed in reflectance and absorbance of thin films.

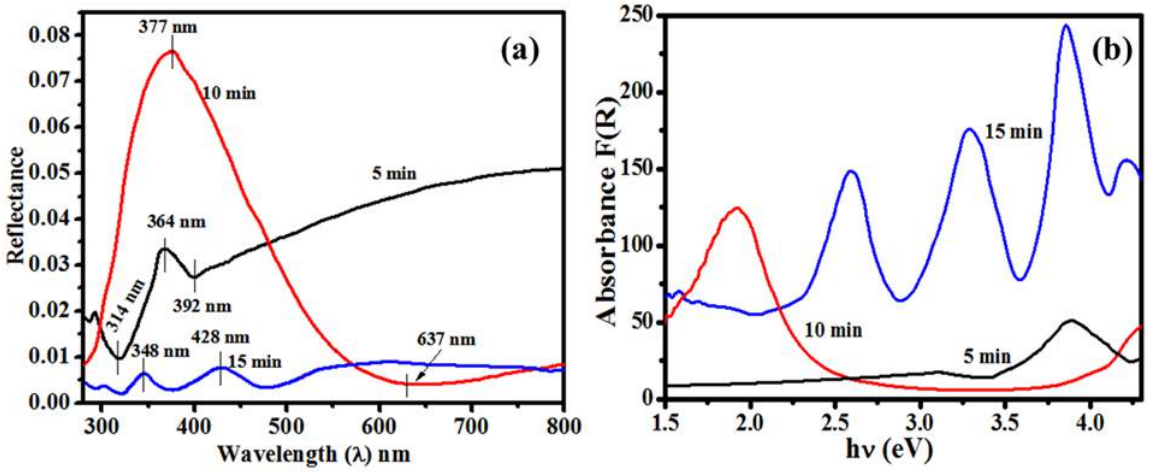

Figure 4.10: Reflectance spectra of TiO_2-Ge composite film deposited on unpolished n-type Si wafer as single layer (5 min), di-layer (10 min) and trilayer (15 min).

Tri-layer film which shows minimum reflectance in the wavelength range 280- 588 nm (i.e. 4.43-2.1 eV) has a maximum absorbance in this range. Also tri-layered film has minimum reflectance (4.10 a) beyond 588 nm (E= 2.1 eV) and maximum absorbance below 2.1 eV (Fig. 4.10 b).

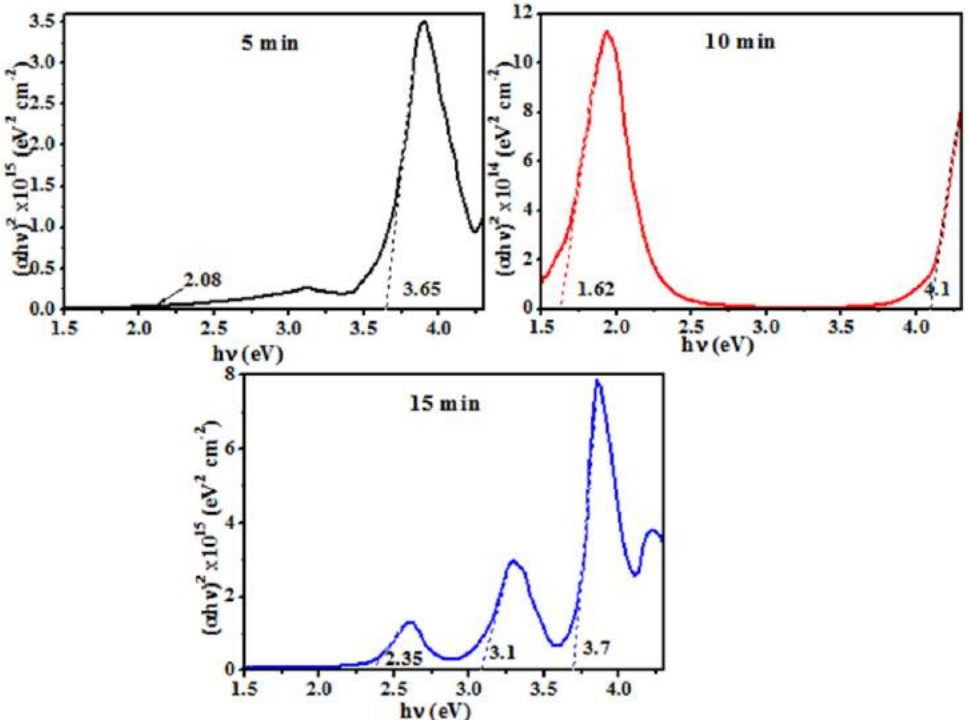

Figure 4.11: Direct transitions of single layer (5 min), di-layer (10 min) and trilayer (15 min) TiO_2-Ge composite film deposited on unpolished n-type Si wafer.

Direct and indirect transitions were also studied in thin films deposited on unpolished n-type Si substrate by Tauc plot through Kelbuka Munk relation as shown in figures 4.11 & 4.12. Single layer film shows direct transitions around 2.08 and 3.65 eV and one indirect transition at 3.7 eV.

Bilayer film has 2 direct transitions at 1.62 and 4.1 eV and an indirect transition at 3.7 eV. Tri-layer film as 3 direct and indirect transitions i.e. 2.35, 3.1, 3.7 eV and 1.98, 2,6 and 3.45 eV. Direct and indirect transitions.

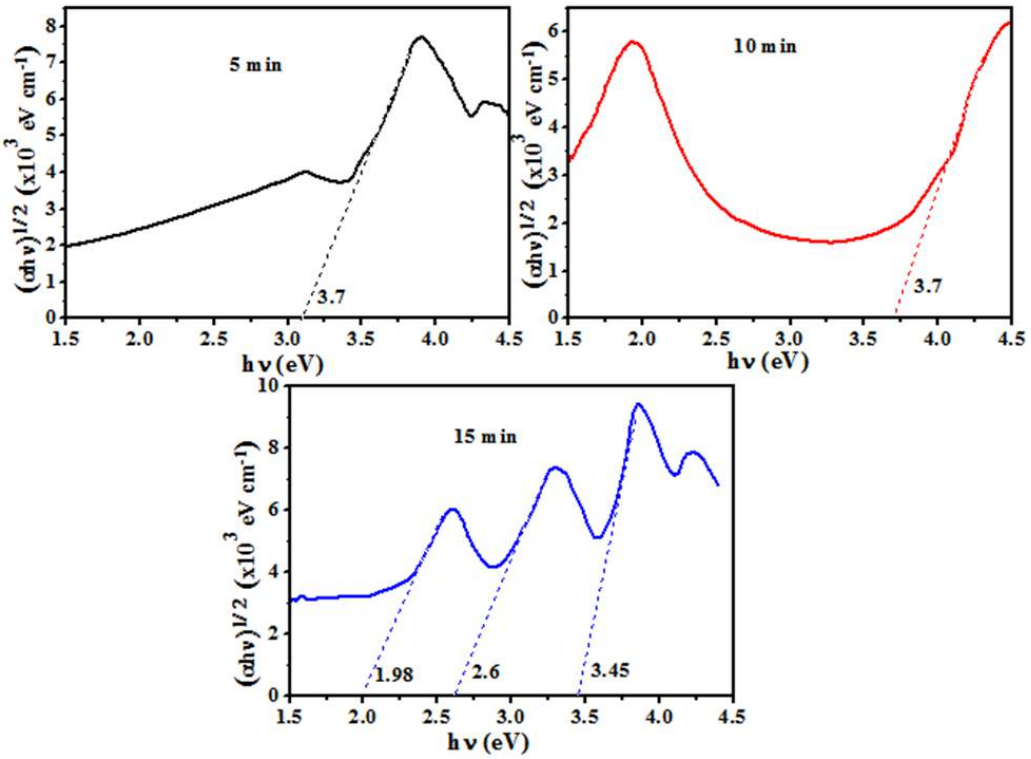

Figure 4.12: Indirect transitions of single layer (5 min), di-layer (10 min) and trilayer (15 min) TiO_2-Ge composite film deposited on unpolished n-type Si wafer.

Direct and indirect absorption transitions observed for thin films deposited on unpolished Si wafer (Fig 4.11 and 4.12 are higher in number than those measured for thin films deposited on polished Si substrate (Fig. 4.8 and 4.9). But the absorption is higher in single and bi-layered thin films deposited on polished Si substrate as compared to those deposited on unpolished Si substrate. But in tri-layered film absorption is higher in thin film deposited on unpolished Si substrate. XRD data (Table 3.3) shows that the crystallite size decreases as new layer is deposited on previous layer which is basically due to increase in thickness of thin film. Therefore nano-dots/

quantum dots of multiple sizes are produced in each layer and hence absorption transitions increase in tri-layered films. Transition occuring at or near 3.7 eV and within the range 2-3 eV are due to the quantum confinement in TiO_2 and Ge respectively. Nano sized Ge shows an increase in band gap from 0.6 eV (for bulk) to higher values. As well as each layer may play some role in modification of optical properties due to strains and defects. There may be internal back scattering in thick samples and K.M theory can not explain it whereas ellipsometry data confirms these results as double and triple layer films have higher refractive index as compared to single layer films (For reference see Fig. 4.16). Thin films grown on substrate by laser irradiation for a longer time i.e. 30 minutes show more transitions and higher absorption. One important reason for increased absorption for higher deposition time is thin film thickness and high refractive index.

4.2 Ellipsometric Studies

Ellipsometric analysis of the samples was carried out to find a link between optical and electrical response of material. Wavelength dependent refractive index **(*n*)**, dielectric constant **(ε_1)** and dielectric loss (ε_2) were then plotted for all samples. Thin film thickness was also measured through ellipsometric data.

Thin films deposited on N and p-type substrate were analyzed through ellipsometry as plotted in Fig. 4.12 and 4.13. In Fig. 4.12 (i), it can be observed that the thin film having 25.3% Ge concentration (labelled as a) has the maximum transparency to visible light with refractive index decreasing from 1.63-1.55 in the wavelength range 300-800 nm. Dielectric constant is minimum for this thin film (Fig. 4.12 ii (a)) which shows that a very small amount of electron- hole (e-h) pairs will be generated when the film will be exposed to light therefore it can have a low conductivity when exposed to light within wavelength range mentioned. Very small ε_2 in this film refers to minimum energy dissipations resulting in minimum heat losses due to recombination as a result of light exposed on to it.

Thin film having 2.6 % Ge (Fig. 4.12 i (b)) has a higher refractive index which decreases from 2.57-1.99 in the wavelength range from 314-394 nm, it then shows a minute rise till 800 nm. Absorbance of this material is highest in wavelength range 335-

800 nm as observed in UV/Vis spectroscopy (Fig. 4.1 B(b)). This film shows a stable dielectric loss ~ 5 (Fig. 4.12 iii (b)) and almost negligible dielectric loss in the wavelength range 300- 800 nm. Which indicates that the light absorbed in this material is utilized to produce e-h pairs with a minimum energy loss/ recombination.

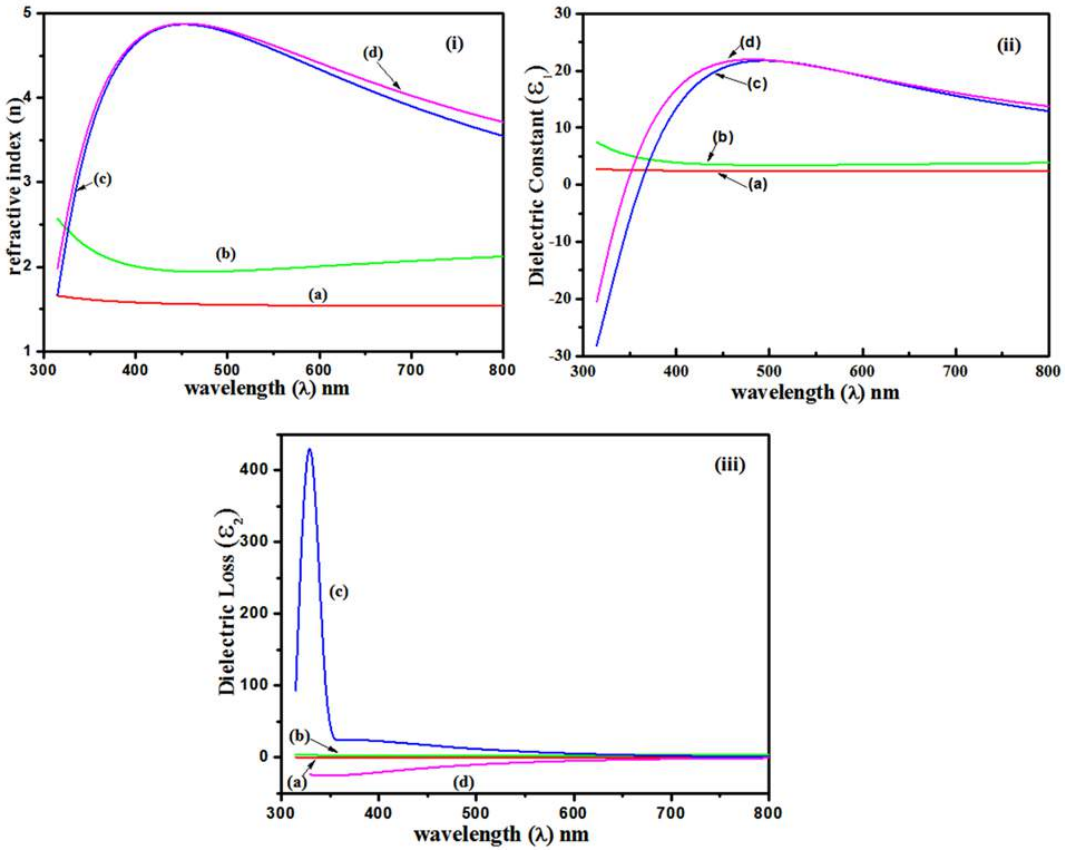

Figure 4.13: n, ε_1 and ε_2 of thin films deposited on n-type Si wafer at X= (a) 5cm, (b) 6 cm, (c) 7 cm and (d) 8 cm.

Thin films deposited at X= 7 and 8 cm (Fig. 4.12 i, (c &d)) show an increase in the refractive index (n) from 1.7 and 1.96 to a maximum value of 4.88 respectively in the wavelength range 300-460 nm. Refractive index then gradually decreases from maximum value to 3.5 (X = 7 cm) and 3.7 (X = 8 cm) in a wavelength range 460-800 nm. Dielectric constant of these films remains negative below wavelength 370 and 350 nm for thin film containing 1.9 and0.9 % Ge (i.e with X= 7 & 8 cm). It then increases to a maximum value of 20 around 480 nm. It then gradually decreases to almost half of its value at a wavelength of 800 nm. Dielectric loss of thin film deposited at X= 7 cm increases to a maximum value of 400 and then decreases to a value of 50 in the wavelength range 300-360 nm (Fig 4.12 iii (c)). Wavelength does not affect the

dielectric loss in the range 360-800 nm. Dielectric loss remains negative for thin film deposited at X=8 cm till 600 nm (Fig. 4.13 iii (d)) and then achieves a very small positive value with increase in wavelength to 800 nm. Looking upon UV-Vis absorption spectra of these films having high refractive index we come to know that although light is absorbed in these materials (Fig. 4.1 B(c.d)) which results e-h pair formation in opposite direction below 350 and 370 nm thin films deposited at X= 7 & 8 cm resulting in heat loss. e-h pair formation direction reverses beyond these wavelengths in both of these thin films (Fig. 4.13 ii and iii). An interesting phenomena is observed in the wavelength range below 360 nm and that is heavy e-h recombination or dielectric loss which means that less conductivity will be observed in this wavelength range and afterwards conductivity will increase with increase in wavelength. Thin film deposited at X=8 cm has negative ε_2 which means loss is negative i.e. there is a gain. The material will start producing more charge carriers on its own due to irradiated light. Therefore the current in thin film deposited at X=8 would be higher than the current in thin film deposited at X= 7 cm (which have been verified through their I-V measurements).

Thin films deposited on p-type silicon wafer show quiet different behavior as compared to thin films deposited on n-type Si wafer. It can be observed in Fig. 4.14 i (a) that the thin film having 25.1% Ge concentration as observed through EDX (Fig. 3.6) has the maximum transparency to visible light with refractive index decreasing from 1.67-1.59 (as compared to other samples). Minimum light is absorbed in it also which is indicated by very small absorbance in UV/ Vis spectroscopy (Fig 4.4 B(a)). Lesser e-h pairs will be generated as it has a very small dielectric constant (Fig. 4.14 ii (a)). It will show an almost very small stable current in the spectrum range from 300-800 nm as dielectric loss and dielectric constant is small and almost invariable in this range. Thin films deposited at X= 5 cm with a very small absorbance (Fig 4.4 B(a)) of light and can be utilized as good light propagation medium with decreased velocity of light. Such materials with minimum or no ε_1 and ε_2 (Fig. 4.23 ii & iii) will not show good optoelectronic behavior Therefore, such materials can be used as core material in optical signal delay devices. Thin film having 2.9 % Ge (X= 6 cm) has a higher refractive index (Fig. 4.14 i (b)), which decreases from 2.57-1.99 in the wavelength range from 314-800 nm. Absorbance of this material is highest as compared to other

thin films as shown in Fig. 4.4 B (b) provided more e-hole pairs will be formed in this film as compared to the film deposited at X= 5 cm. it has a negative ε_2 which means instead of loss charge will be multiplied. A good current will be established in these materials in the presence of light.

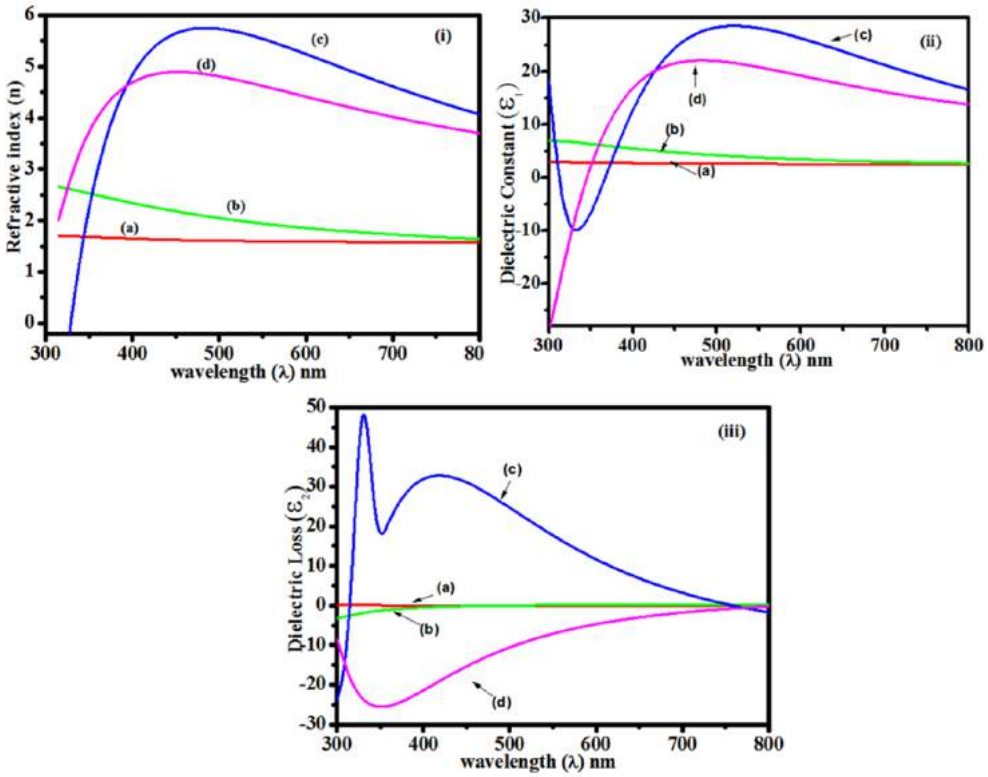

Figure 4.14: n, ε_1 and ε_2 of thin films deposited on p-type Si wafer at X= (a) 5cm, (b) 6 cm, (c) 7 cm and (d) 8 cm.

Thin film having 2.3 (X=7 cm) and 0.89 % Ge concentration (X= 8 cm) show an increase in refractive index from -0.5 and 2 to 5.6 and 5 respectively as shown in Fig 4.14 i, c & d. absorbance of thin film deposited at X= 8 cm (Fig. 4.4B (d)) is greater than that deposited at X=7 cm. (Fig. 4.4 B (c)). Relative permittivity (ε_1) of thin film deposited at X= 8 cm (Fig. 4.14 ii (d)) remains negative when electromagnetic waves of wavelength 300-345 nm are incident on it. It means e-h pairs will be generated in opposite direction, followed by multiplication of charges (having negative ε_2) for light of wavelength 320-345 nm (Fig 4.14 iii (d)). It means a heavier current will flow in reverse direction when a light of wavelength 300-345 nm is incident on it. Transition occurring in the range 300-345 nm (=4.13- 3.59 eV) correspond to the direct and indirect absorption transitions occurring at 3.45, 3.63, 3.86 and 4 eV related to

absorption in TiO_2 measured by Tauc plot (Fig 4.5 and 4.6 d). For this film ε_1 gains a maximum value of 20 at 475 nm (Fig 4.14 iii (d)) and then gradually decreases to a value of 13 for electromagnetic waves of wavelength 800 nm which means e-h pairs will be generated by incident light of $\lambda > 345$ nm. Charge multiplication will also occur in this wavelength range indicated by negative ε_1 (Fig 4.14 iii (d)) i.e in the energy range 1.55-3.45 eV. This charge multiplication is due to the inter-band electronic transitions occurring in Ge related to direct (2.5 eV) and indirect transition (1.9 eV) observed in Tauc plot (Fig 4.5 and 4.6 d).

Thin film deposited at X=7 cm shows a negative dielectric constant for light waves of wavelength less than 350 nm (Fig. 4.14 ii (c)) so e-h pairs will be generated in opposite direction i.e. it will behave as a negative capacitor. Recombination i.e dielectric loss (Fig. 4.14 iii (c)) will occur in this wavelength range it means few majority charge carries would then be available for the establishment of current for light waves incident in this wavelength range. This phenomena occurs due to direct absorption transition in TiO_2 calculated through Tauc plot at 4 eV (Fig. 4.5 (c). Dielectric constant achieves its maximum value at 500 nm (2.48 eV) and then gradually decreases. Whereas dielectric loss is maximum for the light of wavelength 400 nm (3.1 eV). More light is absorbed in the energy range > 3.2 eV (Fig. 4.4, 4.5, 4.6 c) whereas comparatively half intensity is absorbed in the sample for lower energies having $\lambda > 387$ nm. It means the direct and indirect transition occurring in these wavelength range 350-400 nm will result in a very small current but it will increase for any light of wavelength> 400 nm (< 3.1 eV) as ε_2 decreases. Therefore light of wavelength >400 nm will not be dissipated rather it will favour electronic transitions therefore direct transition occurring at 2.48 eV (Fig 4.5 c) and indirect transitions at 1.7 and 2.75 eV (Fig 4.6 c) either due to defects or presence of Ge will result in the increase in current.

Single, di and tri-layered thin films deposited on n-type polished and unpolished Si wafer were studied through ellipsometry are shown in Fig 4.15 and 4.16. Wavelength dependent curves n, ε_1 and ε_2 of single, di and tri-Iayer films is labelled as 5, 10 and 15 min. It was observed that the behavior of wavelength dependent refractive index, dielectric constant and dielectric loss was quiet different as compared to thin films already deposited (30 min).

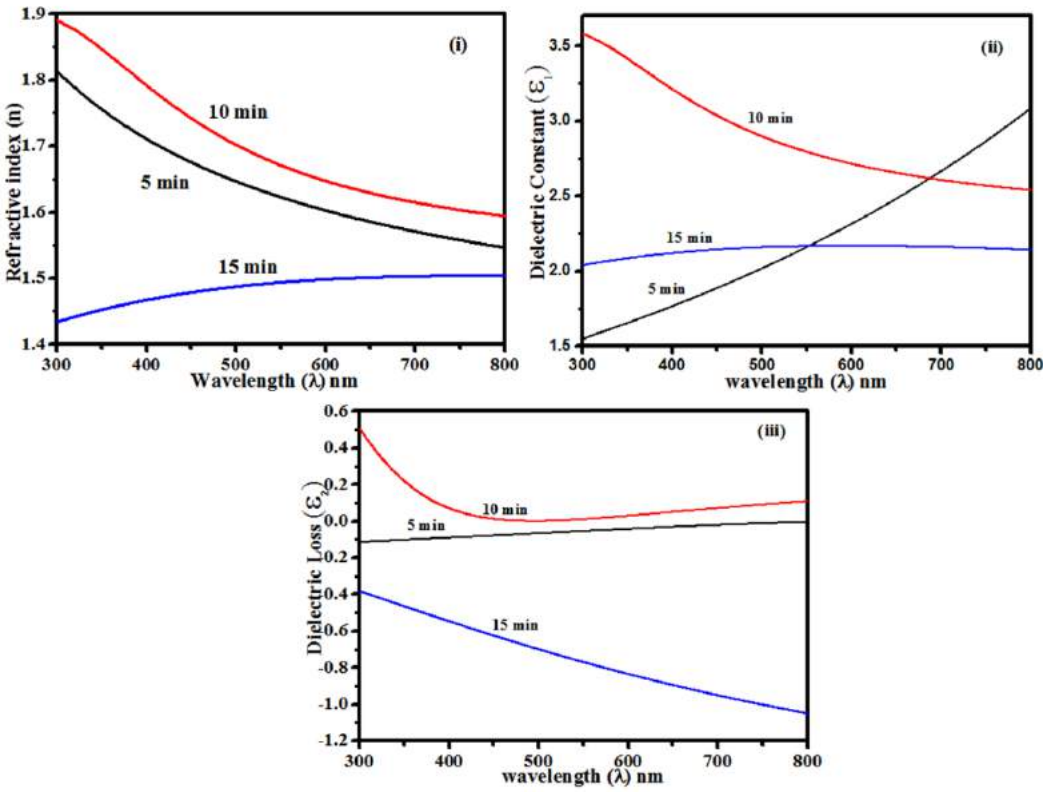

Figure 4.15 : n, $\mathcal{E}_1$ and $\mathcal{E}_2$ of TiO_2-Ge composite film deposited on polished n-type Si wafer as single layer (5 min), di-layer (10 min) and trilayer (15 min).

Refractive index and dielectric constant was found to be positive for all thin films deposited on polished Si substrate (Fig 4.15 i & ii). Bi layer film (Fig 4.15 i 10 min) shows a maximum refractive index which decrease with the wavelength from 1.9- 1.64 for light of wavelength 300-800 nm. Similar trend is observed in single layer film (Fig 4.15 i 5 min) which has a decrease in refractive index from 1.8-1.6 for λ = 300-800 nm. An opposite trend in refractive index is observed for tri-layered film (Fig 4.15 i 15 min) which shows an increase from 1.44-1.5 for the same spectral range. Thin film comprised of three layers shows enhanced reflection which may be due to inter-band transition in quantum dots (5.11 A). The relative permittivity of the films has been observed to be positive; showing charge carriers are formed as a result of light irradiance (Fig 4.15 ii). This trend is similar to refractive index of these films.

It can be observed that the single layer film has a negative **(ε_2)** which means that the thin film may cool down instead of heating as energy will be utilized in moving charges to conduction band (4.15 iii). Electron hole pair formation in two layer thin film

decreases in the wavelength range from 300-800 nm (Fig 4.15 ii). e-h recombination decreases for λ = 300-450 nm which becomes negligible beyond 450 nm to 800 nm. Therefore the current in di-layered film will be less as compared to that in tri-layered film. Tri-layered film is although transparent to light (n~ 1.5) in the wavelength range 300-800 nm (Fig. 4.15 i) and has almost invariant dielectric constant (~2.1) and negative dielectric loss (Fig 4.15 ii and iii). It means that charge density will increase as a result of absorbed light i.e charge will multiply instead of recombination in the presence of light. Dislocation density is higher in tri- layered film (Table. 4.3) therefore it is expected that the negative dielectric loss is due to the ejection of electrons from the defects/ dangling bonds.

Ellipsometry data for single, di and tri-layer films deposited on unpolished n-type Si substrate is plotted in Fig. 4.16.

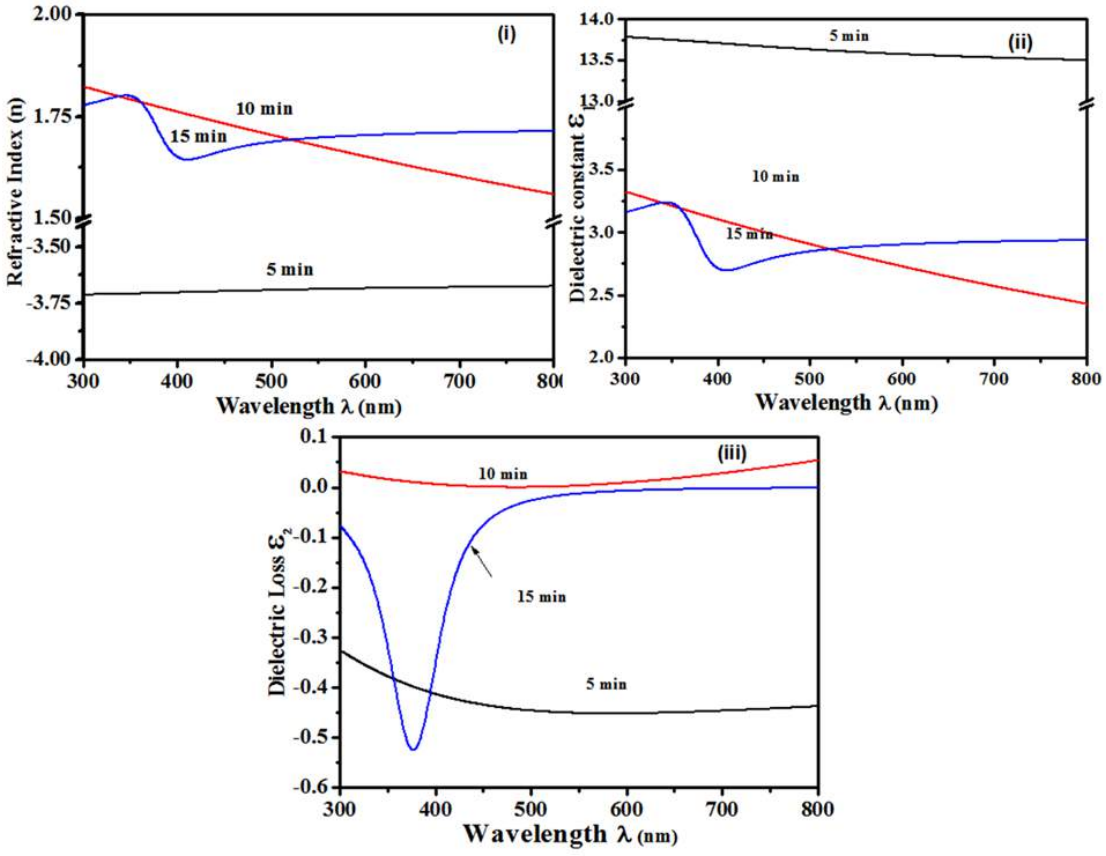

Figure 4.16 :n, $\mathcal{E}_1$ and $\mathcal{E}_2$ of TiO_2-Ge composite film deposited on unpolished n-type Si wafer as single layer (5 min), di-layer (10 min) and trilayer (15 min).

Refractive index of thin films has been found to be positive for two layer and three layer system deposited on unpolished Si wafer whereas it is negative for single layer film (Fig. 4.16 i). Negative refractive index may be associated to defects present in films as shown in Table 4.3. Dielectric constant of single layer film is found to be highest ~13.5 whereas di layer and tri-layer films have comparatively lower dielectric constant ε_1 (Fig. 4.16 ii). e-h pair generation will therefore be highest in single layer film. Energy loss or e-h recombination rate is although small but is highest in di-layered film amongst the three samples (Fig. 4.16 iii).

Single layer film although has comparatively less absorbance as compared to di and tri-layered film (Fig 4.10 b), and its effect in all three samples is different. In single layer film absorbed light rays produce electron hole pairs along with the dielectric gain, i.e. instead of recombination, charge multiplication will occur which possibly due to the charge is originating from defects. So a steady current will be established in this film and light will not increase the resistance, rather it will decrease the resistance of material. Di-layer film has a good absorbance in the energy range < 2.5 eV (i.e. $\lambda > 496$ nm) as shown by UV/ Vis spectroscopy (Fig 4.10 b). Amount of absorbed light does not seem to play any effect on the dielectric constant and dielectric loss of the film (Fig. 4.16 ii and iii); as both the quantities seem to decrease smoothly with increase in wavelength. Tri-layered film shows a small rise in n and Ɛ1 with increase in wavelength from 300-350 nm whereas dielectric loss is negative. Refractive index decreases for λ=350-400 nm dielectric loss still remains negative and achieves its minimum value of -0.53 at λ= 380 nm (3.26 eV) and becomes zero at 500 nm (2.48 eV). It means the light absorbed due to direct and indirect transitions (Fig. 4.11 and 4.12) at 3.1(400 nm) and 3.45 eV (359 nm) not only produce electron hole pairs but will eject out further electrons possibly from dangling bonds produced from dislocations and hence will result in an increase in current. Similarly direct and indirect absorption transitions at 2.35 (527 nm) and 2.6 eV (477 nm) will produce e-h pairs only i.e positive Ɛ1 (Fig. 4.16 ii) with no recombination as Ɛ2 ~ 0 in wavelength range from 500-800 nm (Fig. 4.16 iii). Therefore light incident on trilayered film will result in a current with minimum or no dielectric losses.

4.3 Photoluminescence spectroscopy

Photoluminescence spectra was recorded to find the inter-band transitions in thin films as well as to find a relation of these transitions to defect levels or quantum confinement effect.

Photoluminescence (PL) spectra of thin films on N and p-type Si wafers has been shown in Fig. 4.17 and 4.18. PL is not zero rather it has a minimum photoluminescence intensity greater than 5000 in all the samples. Peaks around 2.3 and 2.05 are observed in all the samples which is due to system error.

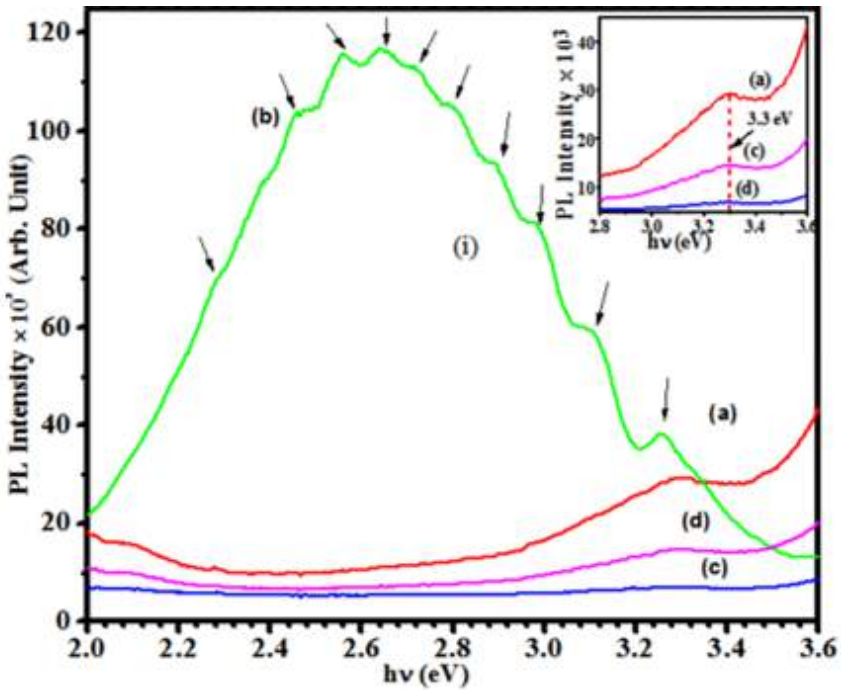

Figure 4.17: PL spectra of thin films deposited at a target-substrate distance of (a) 5 cm, (b) 6 cm, (c) 7 cm and (d)8 cm on n-type Si wafer.

To confirm the nature of broad spectrum transitions studied through UV-Visible spectroscopy we have also studied the PL spectra of composite TiO_2-Ge films deposited at X= 5, 6,7 and 8 cm. While inset shows the PL spectra of all the thin films in the energy range 2.8-3.6 eV except the film deposited at X= 6 cm. PL spectra are recorded at room temperature and thin film with 2.6% Ge concentration (Fig. 4.17 b) shows a broad emission spectrum with a tail in UV region. Apparently, PL intensity of all other samples is negligible. PL intensity in all the samples is non-zero, and PL intensity of

thin film deposited at X= 6 cm (Fig. 4.17 b) is six times the intensity observed for thin films deposited at X= 5, 7 and 8 (Fig 4.17 a,c,d). PL intensity is observed in thin films deposited at X= 5, 7 and 8 cm in the energy range 2.25- 2,8 eV. Thin film deposited at X= 5 cm (Fig. 4.17 a) also exhibits weak direct and indirect transition in IR and UV range (Fig. 4.2 and 4.3 (a)) which can also be associated to transitions related to TiO_2; having direct and indirect band gap in UV region. Thin film deposited at X= 6 cm (Fig. 4.17 b) exhibits maximum photoluminescence in visible and UV spectral rang. Direct and indirect transitions measured from Tauc plot from reflectance spectroscopy of this film lie in IR, UV and Visible region. These transitions can be related to strain associated to lattice mismatch between Ge, Si and TiO_2 hetero-structures [196-198]. Maximum PL in visible region could be attributed to the quantum confinement in Ge which is in confirmation with a previously reported work by E B Kaganovich et. al [199] They reported that PL peak observed in visible region is due to Ge crystals with an average size of less than 1.3 nm and for larger particles ~ 2.2 nm PL peak is observed in IR range. Therefore broad spectrum PL comprising of IR and Visible emissions can also be associated to the presence of multiple sized Ge QD's and transitions lying in UV region with energy > 3.7 eV can be associated to quantum confinement in TiO_2 [190]. Multiple transitions exhibited from IR-UV range through Tauc plot for reflection spectrum can be associated to band edge shifting, defects in crystals and quantum confinement in Ge. Dislocation densities have been tabulated in table 3.1 for these samples. It can be seen that the dislocation density is higher in thin films with minimum Ge concentration. As the Ge concentration increases the dislocation density decreases which can be associated to lattice mismatch between Ge and TiO_2 at grain boundaries due to composite nature of films. This can be due to the fact that thin film with 25% Ge concentration (X = 5 cm) has been fabricated closer to target when plasma temperature is high whereas plasma temperature goes on decreasing with increase in target-substrate distance due to which growth species nucleate by condensation. Therefore the crystallinity of growth species improves at higher target-substrate distance, so that lattice mismatch at grain boundaries may have resulted in higher dislocation density. Thin films deposited at X= 5, 7 and 8 cm show PL in UV region which is in confirmation to the UV/ Vis absorption transition (Fig. 4.2 & 4.3 a, c, d) in UV spectral range associated to quantum confinement in TiO_2. UV/Vis transitions in these samples

in visible region can-not be attributed to quantum confinement in Ge rather it can be associated to defects/ dislocations as no PL peak could be observed in visible region. Ellipsometric analysis reconfirms the role of defects in electronic properties as thin film deposited at X=7 and 8 have negative ε_2 which means charges will be multiplied at the expense of defects. So absorbed light will be used in ejecting charges from dangling bonds rather than the formation of electron hole pairs therefore no emission transitions could be observed in PL spectra of these samples.

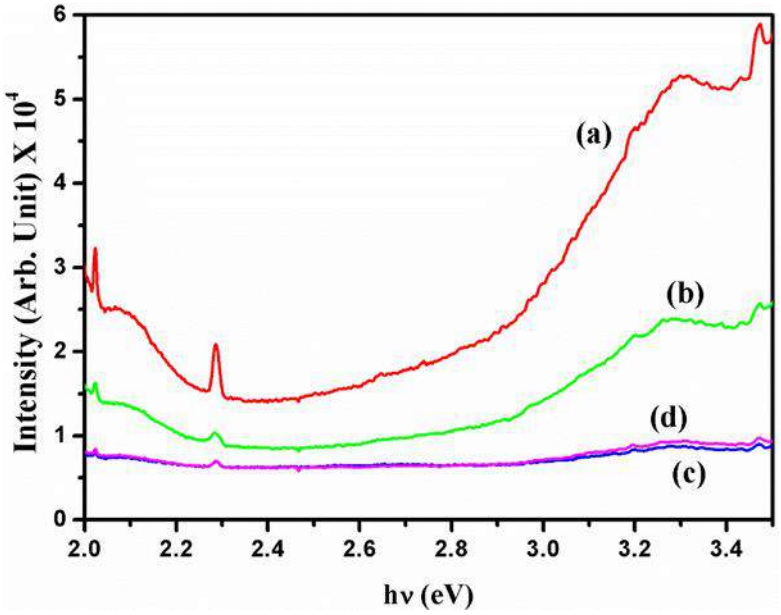

Figure 4.18: PL spectra of thin films deposited on p-type Si wafer at a target-substrate distance of (a) 5 cm, (b) 6 cm, (c) 7 cm and (d)8 cm.

PL spectra of films deposited on p-type Si substrate at X= 5, 6, 7 and 8 cm (Fig. 4.18) shows a visible peak around 3.3 eV (UV region). Thin film deposited at X= 5 cm shows Direct and indirect UV/ Vis absorption transitions at 1.9, 3.65 and 1.3 and 3.24 (Fig. 4.5 and 4.6 a). The absorption transitions 3.65 and 3.24 are related to TiO_2 and PL peak is also observed in this region which can be attributed quantum confinement in TiO_2 as reported earlier [190]. Similar behaviour is observed in thin film deposited at X= 7 cm which has direct and indirect transitions in UV region (Fig. 4.5 and 4.6 b). A comparatively small peak is observed at 2.1 eV in thin film deposited at X= 5 and 6 cm which show very small absorbance (Fig. 4.4 B a, b) in this region and are close to the absorption transitions found from the Tauc plot of these samples. These transitions can-not be associated to Ge rather they can be associated to the presence of brookite which

shows reduction in lattice parameters as confirmed through check cell. It means brookite TiO_2 also shows weak QCE exhibiting radiative transitions in the energy range 2-2.2 eV. Thin films deposited at X= 7 and 8 cm show similar comparatively small PL as compared to thin films deposited at X= 5 and 6 cm. A very small hump can be seen in PL spectra of these films in the energy range 3-3.6 eV. These films although dhow direct and indirect absorption transitions but they are small as compared to other films. Thin film deposited at X= 7 is non crystalline (Fig. 3.2 c) and the film deposited at X= 8 is although crystalline but it has a highest dislocation density as compared to other films (Table 3.2). Therefore it can be estimated that the absorbed light may not result in radiative emission in amorphous film deposited at X= 7 cm which may be associated to the absorption in defects as can be seen by a direct transition of 2.5 eV but no emission is observed in PL. Light absorbed in thin film deposited at X=8 cm not only generated e-h pairs but prohibits recombination (resulting in radiation) rather it additionally ejects electron from defects (i.e. it has $-\varepsilon_2$) as observed in Fig 4.14 iii (d) therefore the absorbed light is non emissive. Thin films deposited at X= 7 and 8 have a very high refractive index (Fig 4.14 iii c, d) therefore any emitted light may have also been absorbed in the material.

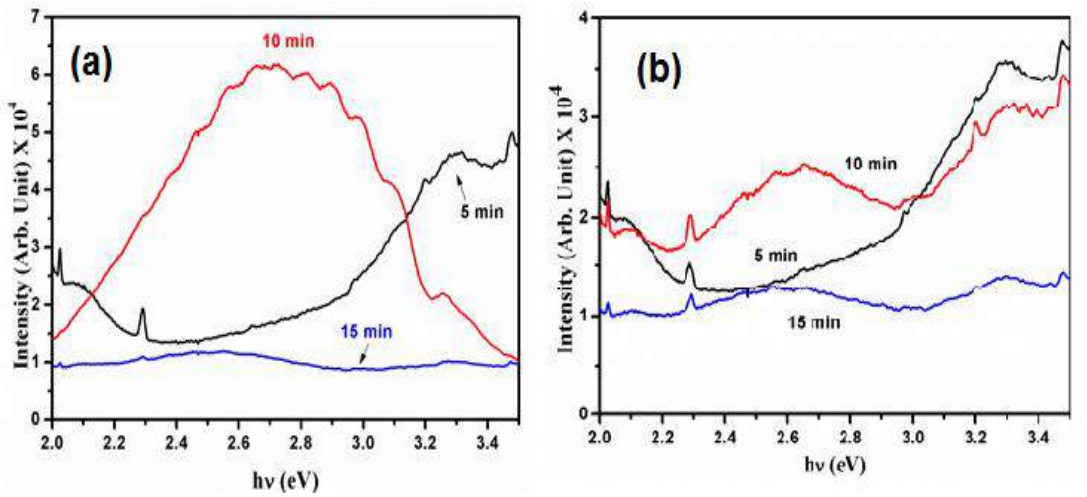

Figure 4.19: PL spectra of TiO2-Ge composite film deposited on n-type polished (a) and unpolished (b) Si wafer as single layer (5 min), di-layer (10 min) and trilayer (15 min).

Photoluminescence spectra of multilayer films on n-type (polished and un polished) substrate is shown in Fig. 4.19 (a &b) and single, di and tri-layered films are labelled

as 5, 10and 15 min. PL spectra of single, di and tri- layered thin film deposited on polished Si substrate is different from the films deposited on unpolished Si substrate. Almost similar behaviour is observed in the PL spectra of single and tri-layered film.

Single layer film shows PL in the energy range 3-3.6 eV and a small PL peak in in the energy range 2-2.3 eV. Absorbance is observed in the energy range 1.5-2.5 eV through UV/Vis spectroscopy of this sample (Fig. 4.7 b) but the absorption in the energy range 3-3.6 eV can-not be observed. These emissions observed in the UV region in PL may be associated to defects as they are not observed in UV/ Vis absorption [200].

PL spectra obtained for bi-layered film (10 min) is similar to the PL spectra obtained for thin films deposited on n-type Si wafer for 30 minutes at X= 6 cm (Fig 4.17 b). Whereas the bi-layered film has comparatively less thickness and is non crystalline. This film also shows less absorbance in the energy range 1.5-2.5 eV and highest absorption in the energy range >2.5 eV as measured through UV/Vis spectroscopy (Fig. 4.7 b) where most of energy is absorbed in TiO_2 confirmed by direct and indirect transitions at 3.96 and 3.31 eV (Fig. 4.8 and 4.9). Maximum photoluminescence is not associated to quantum confinement in Ge but it may be due to the multiple reflections due to defects [200].

Tri-layered film shows weak PL around 2.5 eV which is related to indirect transition observed in UV/ Vis spectroscopy (Fig 4.9). This transition can be attributed to quantum confinement in Ge reported earlier [199]. As the refractive index of this material is ~ 1.5 therefore light rays can pass through it and the absorbed light can produce electron hole pairs (i.e. $\varepsilon_1>1$) and can eject out further electrons from the defects (i.e. negative ε_2). Luminiscence observed as a result of relaxation in the absence of light confirms the presence of Ge QD's.

If we look at the photoluminiscence of single, di and tri-layered films deposited on unpolished Si wafer (Fig. 4.19 b) we come to know di and trilayered films show luminiscence peaks in energy range 2.3-3 eV and 3-3.4 eV.A small luminiscence peak is observed in these 3 samples around2-2.2 eV. Single layered films also shows luminicence in th energy range 3-3.4 eV. All the luminiscence peaks in single and tri-layered films are in confirmation with the absorption transitions observed through their

UV/Vis spevtroscopy (Fig. 4.11 and 4.12). Single layer film shows absorption transitions around 2.08 and 3.65 eV, transition at 2.08 eV is in fact due to quantum confinement in Ge as maximum electron holes are produced in this material as a result of light irradiance because it has a very high dielectric constant (Fig. 4.16 ii). These improved electronic properties may be associated to the QCE. But the absorbance is small in this film as compared to trilayered film (Fig. 4.10). Therfore, this material may show a small current as compared to trilayered film. Trilayered film shows absorbance in IR, IV and visible region with direct absorption transitions lying in visible and UV region, whereas indirect transitions in all regions. PL emission spectra also lies in the same range where these transitions occur. Absorbance is very high in tri-layered film as compared to other films except bi-layered film in the energy range 1.5-2.2V (Fig. 4.10). But the PL spectra of single-layered film has high intensity as compared to that of tri-layered film which may be due to high refractive index of single-layed film (Fig. 4.16 i) which can absorb light but allows less light to pass through it to show emission. Bi-layered film shows direct transitions in IR and UV region and indirect transition only in UV region as measured through UV/Vis spectroscopy (Fig.4.11 and 4.12). PL shows emission in visible region too and no absorption transition by UV/Vis spectroscopy are observed in this region (Fig.4.11 and 4.12). PL in visible region may be due to defects as dislocation density in dilayer is greater as compared to that in single layer film (Table. 3.3).

Sinusoidal humps in regular intervals observed in thin film deposited at X= 6 cm are due to the uniform film surface. It is also found that thin films deposited on unpolished Si substrate for 15 mins show a better absorption in visible solar region as compared to those on polished Si substrate. UV-Visible spectroscopy of the films depicts that incorporation of Ge in thin films has resulted in the absorption transitions in visible region which is attributed to defects/ quantum confinement in Ge as explained earlier. Increase in target-substrate distance has resulted in an increase the refractive index and hence extinction coefficient. Which is mainly the contribution of Ge nano-domains having higher refractive index formed by condensation of Ge at higher target-substrate distance. Thin films deposited at X=6 cm are expected to show better electrical response in light due to the fact having dielectric loss ≈ 0. There is a difference in optical and

dielectric properties of thin films deposited on polished and unpolished Si substrate. Single, double and tri-layer films exhibit a dielectric constant below 2 and a better dielectric constant, whereas negative dielectric loss is observed in single and tri-layered films deposited on unpolished Si substrate. Thin films deposited at X=6 cm on n-type polished Si (100) substrate for 10 and 30 mins exhibit a good photoluminescence in visible region which is attributed to quantum confinement in Ge as discussed earlier in detail. Quantum confinement effect has been observed to increase the PL and UV-Vis absorption in thin films and likely to result in a good electrical response in dark and light.

Chapter 5

5 Electrical Characterization

Electrical properties of thin films was studied through their I-V responses (dark & light) under vacuum. Response in light was measured under halogen lamp. As well as hall measurement as carried out to find various factors like charge carrier concentration, resistance and mobility to find the possible connection of these quantities with the photo-response of thin films.

I-V response of thin films deposited for 30 minutes on n-type polished Si substrate at various target-substrate distances (X = 5,6,7 and 8 cm) were recorded at room temperature as shown below (Fig. 5.1).

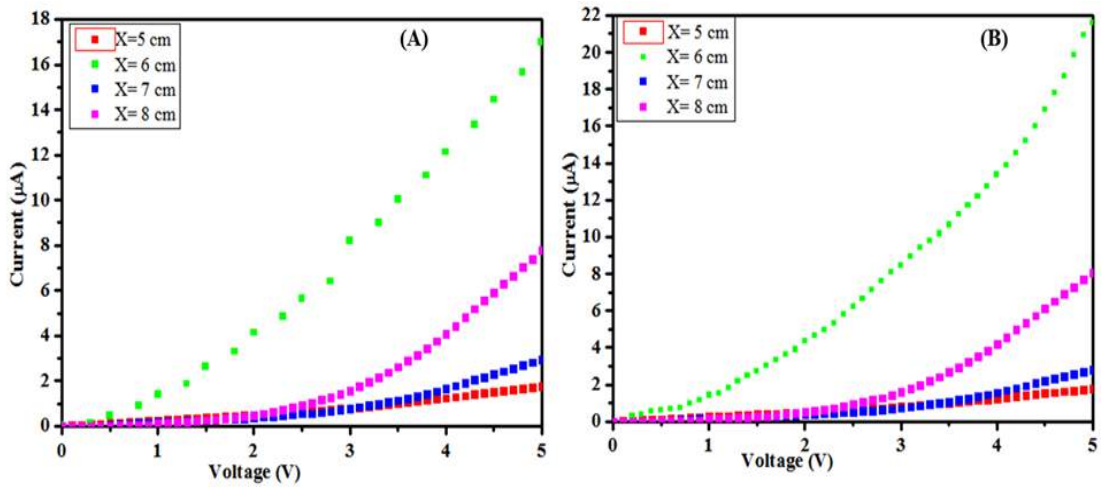

Figure 5.1: I-V response of films on n-type Si at target-substrate distance X = 5, 6, 7 and 8 cm where (A) shows I-V response in dark and (B) shows I-V response under light.

I-V responses (dark) of films show that films grown at X= 6 show good electrical response as compared to other films. Better electrical response can be related to the crystallinity of the film (Fig. 3.1) as thin film deposited at X=5 shows poor crystallinity as compared to other thin films although it contains 25.6% Ge. Thin film deposited at X= 5 cm shows minimum current in dark and under light too.

If we look on the absorbance of this film we come to know that it has a very small light absorbance (Fig. 4.1 B(a)) and a very small dielectric constant when light is incident on it which is the reason for small I-V response in dark and light. Thin film deposited at X= 6 cm shows a better I-V response and UV/ Vis spectroscopy reveals that the thin film exhibits direct and indirect transitions in visible region (Fig. 4.2 and 4.3) which may possibly be due to the formation of Ge quantum dots. Quantum confinement in Ge improves the optical and electrical response of materials [189], therefore it has improved I-V response in light too.

Another reason for a good I-V response in light is that it has maximum absorption and better electron hole generation in light without any dielectric loss (Fig. 4.13 ii, iii (b)). Thin films deposited at X= 7 and 8 and show I-V response better as compared to thin film deposited at X=5 cm. but no difference is observed in their electrical response in dark and light which is possibly due to their higher refractive index (Fig. 4.13 I c,d).

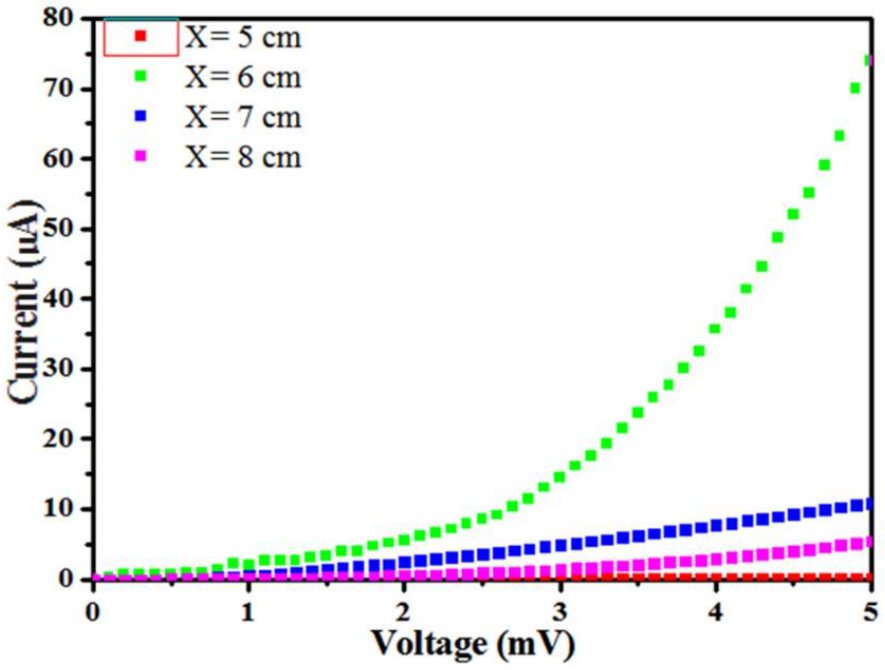

Figure 5.2: I-V response in dark of films on p-type Si at a target-substrate distance X= 5, 6, 7 and 8 cm.

Films on p-type Si were characterized for their I-V response at various target-substrate distance (X= 5, 6, `7 and 8 cm). No difference in their I-V response in dark and light was observed so only I-V response in dark has been shown in Fig 5.2.

Ge concentration decreases with increase in target-substrate distance. Variation in Ge concentration has been observed to effect the electrical response and it has been found that the films deposited at X= 6 cm show a better electrical response (Fig. 5.2 X=6 cm) as compared to films grown at X≠ 6 cm. Better electrical response can be due to a positive dielectric constant and a negative dielectric loss (Fig. 4.14 ii,iii (b)). The negative dielectric loss occurs due to defects which produce excessive charge from the dangling bonds [129]. Thin film deposited at X=5 although contains 25.1% Ge exhibits a poor I-V response which is due to negligible dielectric constant (Fig 4.14 ii a).

Thin films deposited at X= 7 and 8 cm show a better I-V response as compared to thin films deposited at X= 5 cm. Effect of substrate can also be observed on the structural properties of thin film and hence its optical properties. Thin films deposited at X= 7 cm is non crystalline but contains 2.3 % Ge. Amorphous nature of film is responsible to show direct absorption transitions at 2.5 eV (Fig. 4.5) which is attributed to defects ad PL spectra shows no emission peak at this energy range. Therefore the defects may act as trap centers and hence could not contribute to increase the current.

Thin film deposited at X= 8 cm shows I-V response which is better than thin film deposited at X=5 cm and poor as compared to thin film deposited at X= 7 cm. Thin film deposited at X=8 cm is although crystalline but it has maximum defects as it has highest dislocation density (Table 3.2) which may be responsible for smaller current.PL shows that no nanostructures or quantum dots have been established in thin films deposited at X=7 and 8 cm therefore they show poor conductivity.

Thin films deposited at X=6 cm had a better electrical and optical response. Although films on p-type Si have shown remarkably high current as compared to those on n-type Si substrate but they have not shown any photo-response therefore rest of samples were fabricated at X=6 cm.

Single, di and trilayered films deposited at X=6 cm on n-type polished and un-polished Si substrate were studied for their electrical response in dark and light as shown in Fig. 5.4 and 5.5. Trilayered films show a better electrical signal as compared to other films.

I-V response in dark and light of films on polished Si have been shown in Fig 5.3.

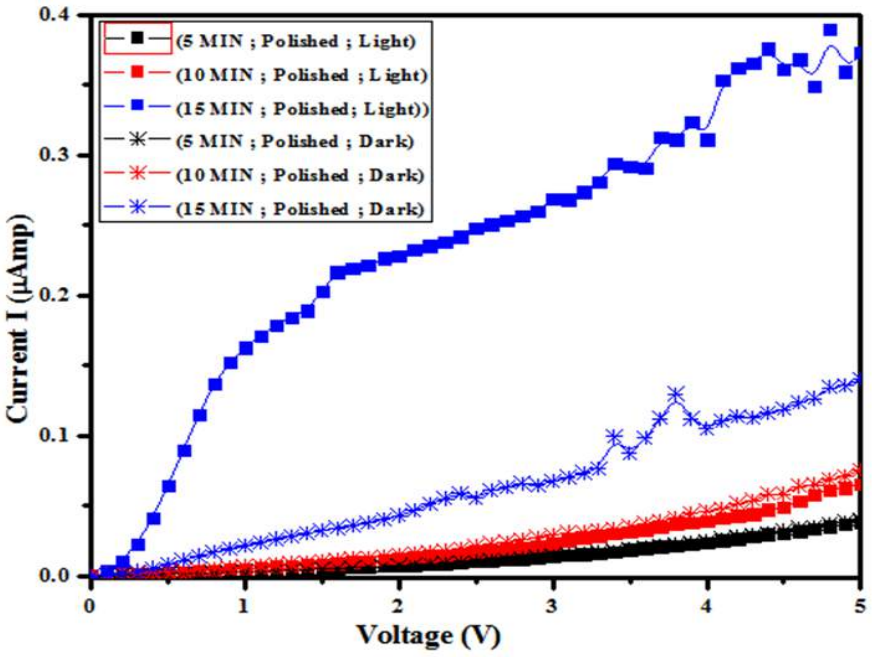

Figure 5.3: I-V response of TiO_2-Ge composite film deposited on polished n-type Si wafer of single layer (5 min), di-layer (10 min) and trilayer (15 min) where response in light is represented by line joinig ■ and in light is represented by line joining∗.

It is clear that tri-layered film exhibits best electrical response in dark and light. I-V response is improved in light in tri-layered film. Tri-layered film shows weak PL around 2.5 eV which is related to indirect transition observed in UV/ Vis spectroscopy (Fig 4.9). This transition can be attributed to quantum confinement in Ge reported earlier [199]. Luminiscence observed as a result of relaxation in the absence of light confirms the presence of Ge QD's therefore these quantum dots will contribute to the conduction in material.QD's may increase the dislocation density (Table 3.3) by introducing more defects which will improve the conductivity in dark and light too. Light rays can pass through this material as it has n ~ 1.5 also it has $\varepsilon_1>1$ for light having λ= 300-800 nm means absorbed light will produce electron hole pairs along with charge multiplication as it has negative ε_2 (Fig. 4.15). Therefore current in light is increased as compared to current in dark.

Di layer film shows a better I-V response as compared to single-layer film (Fig. 5.3). Thin film thickness increases as another layer is added therefore thickness is also effecting the conductivity. Di-layer film is although non- crystalline and anatase a less stable crystalline form of TiO_2 is observed in Raman spectroscopy (Fig. 3.14) showing

an absorption in UV region as observed in UV/Vis spectroscopy (Fig. 4.11). This film shows a PL peak in visible region which is attributed to defects present in the film, so small I-V signal may be attributed to the defects acting as trap centers although this film has a high dielectric constant (Fig. 4.15 ii).

Single-layered film is although crystalline in nature and Ge exists in crystalline form but it cannot show a better I-V response as it has brookite and anatase structures of TiO_2 incorporated as a result of deposition (Fig. 3.14). It shows direct and indirect absorption transitions related to Ge and TiO_2 (Fig. 4.8 and 4.9), but no significant PL emission showing quantum confinement in Ge is observed (Fig. 3.14 A). Therefore no appreciable current could be established.

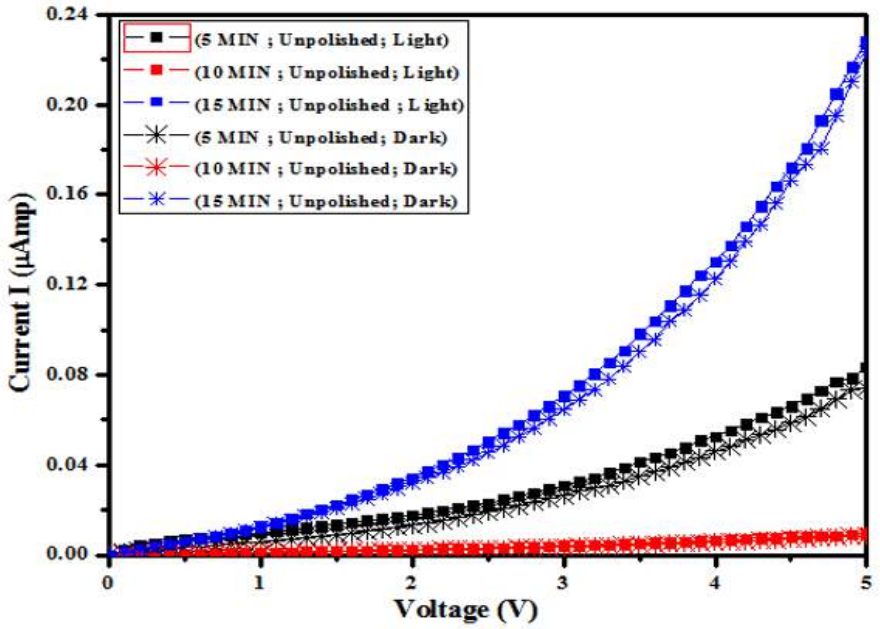

Figure 5.4: I-V response of TiO_2-Ge composite film deposited on unpolished n-type Si wafer of single layer (5 min), di-layer (10 min) and trilayer (15 min) where response in light is represented by line joinig ■ and in light is represented by line joining∗.

Single, di and tri-layered thin films deposited on unpolished Si substrate were studied for their electrical response in light and dark. It was observed that tri-layered film showed a highest response and the response of tri-layered film on polished substrate is similar to the response of tri-layer films on unpolished Si (Fig. 5.4) in dark. Direct absorption transition in single layer film at 2.08 eV is found to be due to quantum confinement in Ge as confirmed by PL emission spectra. Large number of e-h pairs

(Fig. 4.16 ii) are generated as a result of QCE, therefore a steady current will be established in this film. But defects present in this film not only seem to produce a negative extinction coefficient which can reduce its conductivity.

Bi-layered film which has rutile TiO_2 occurring in it also has brookite as observed in Raman spectroscopy. It therefore seems to effect the electrical response of material, also PL emission confirms major contribution of defects in emission. Small current below 2 μA is infact due to the defects as measured in XRD (Table 3.3) which act as trap centres.

Trilayer film deposited on unpolished Si substrate shows the highest I-V response which may is due to the fact that it has a negative dielectric loss (Fig. 4.16) in the wavelength below 600 nm. And for rest of spectrum it has no di-electric loss. As well as quantum confinement in Ge is observed , which will increase the electrical response of material. Therefore trilayered thin film which is although no crystalline shows a better I-V response as compared to single layer thin film.

If we compare the I-V response of thin films deposited in different batches we come to know that all films show current in μA. No difference in light and dark, I-V response of films deposited on p-type Si is observed reson for such response is different in each sample, Films grown at X= 5 and 6 cm have a very low refractive index ($1< n < 3$) and those at X= 7 and 8 cm have a very high n ($0 < n <6$) . Generation of e-h pairs in light and dark would be similar in films deposited at X= 5 cm as dielectric constant remains same in IR, visible and UV range (Fig. 4.14). Films grown at X = 6 cm show negative ε_2 i.e. carrier concentration will increase. But a small $\varepsilon_1 <5$ in UV range and very small $\varepsilon_1 \approx 0$ in visible and infra red region is the reason for not being photoresponsive. Films which are grown at X=7 and 8 cm are less transparent to light (very high n) therefore small amount of absorbed light could not result in e-h pair generation so they show a weak photoresponse. Also PL spectra of films on p-type Si substrate shows liminiscence in UV region only which means light is absorbed by defects resulting in non-radiative absorption. A weak photoresponse of these films therefore shows that defects act as trap centres and hence restrict current in these films.

Current in single, di and trilayered films on polished Si is less as compared to those polished Si. The interface between the layers may also be responsible to decrease the current in trilayered film as compared to thin film deposited for a single run.

5.1 Hall measurements

Various factors like sheet resistance, resistivity, bulk & sheet carrier concentration and mobility were calculated for films characterized through hall measurement. Data for films grown at target-substrate distance; X= 5, 6, 7 and 8cm on N and p-type Si is shown in Table 5.1. Also Data related to single, di and tri-layered films is shown in table 5.2

Table 5.1: Sheet resistance, resistivity, carrier concentration and mobility measurements calculated through hall effect measurement.

Sample code	Target-substrate distance X (cm)	Sheet resistance (Ω/cm^2)	Resistivity (Ω/cm^1)	Type	Sheet carrier concentration (cm^{-2})	Bulk carrier concentration (cm^{-3})	Mobility (cm^2/Vs)
NSi5-30	5	2.75×10^5	6.45	p-type	1.37×10^{11}	5.48×10^{15}	216
NSi6-30	6	8.12×10^5	20.3	p-type	6.27×10^{10}	2.16×10^{15}	156
NSi7-30	7	6.53×10^6	138	p-type	3.87×10^{10}	1.83×10^{15}	76
NSi8-30	8	8.27×10^5	22.5	p-type	5.39×10^{10}	1.98×10^{15}	167
PSi5-30	5	8.80×10^5	56.3	p-type	5.46×10^{10}	8.54×10^{14}	212
PSi6-30	6	4.68×10^5	11.7	p-type	2.80×10^{11}	1.12×10^{16}	67.7
PSi7-30	7	9.07×10^4	2.09	p-type	2.35×10^{12}	1.02×10^{17}	113
PSi8-30	8	6.24×10^5	15.4	p-type	1.99×10^{10}	8.06×10^{14}	808

It can be observed that the concentration of Ge has an inverse relationship with target-substrate distance (Table 3.4). For films grown on n-type Si substrate, mobility and charge carrier concentration decreases with increasing target-substrate separation (X = 5,6 and 7 cm) but it suddenly rises in thin films deposited at X= 8 cm. an inverse trend is observed in resistivity. Therefore it can be concluded that films grown on polished n-type Si show a direct relationship between Ge and charge carrier concentration in films having Ge concentration in the range 26.6- 1.9%. But below this concentration charge carrier concentration decreases. A possible reason is the negative dielectric loss

(Fig. 4.13 iii (d)) in which charge instead of recombination start increasing, which is provided by the defects. Thin films deposited at X=8 have maximum defects as indicated by maximum dislocation density in Table 3.1. Thin film deposited at X=5 although has minimum resistivity, maximum carrier concentration and mobility but the current observed in I-V curve is minimum (Fig. 5.1) which is due to the fact that this material has a very small dielectric constant (Fig. 4.13 ii (a)). As thin film is p-type in nature therefore it will need electrons from e-h pairs and small dielectric constant therefore prohibits charges to move across the band gap to constitute a current. Thin film deposited at X= 6 cm although has a higher resistivity but it has higher ε_1 which enables it to achieve a better I-V response.

If we carefully observe the results obtained for films on p-type Si grown at target-substrate distances (X = 5,6,7 and 8 cm) we come to know that resistivity decreases at target-substrate distance increases from X= 5-7 but it again increases for thin films deposited at X=8 cm. Similarly sheet carrier concentration is higher in thin films deposited at a higher separation between target and substrate except thin film deposited at X=8 cm. Thin film at X= 8 shows highest mobility among all the films. Thin film deposited at X= 6 m although has minimum mobility but its I-V response is better as compared to other thin films deposited in this batch (i.e. deposited at X= 5, 7 and 8 cm). It happens because of its p-type nature, thin film has higher number of positive charge carriers (i.e. holes) in order to conduct electrons are needed which are produced as it has a positive dielectric constant (ε_1) (Fig. 4.14 ii (b)) and negative dielectric loss ($-\varepsilon_2$) (Fig. 4.14 iii (b)); which enables electrons from the unpaired bonds generated as a result of defects. Minimum current established in thin film deposited at X = 5 cm is due to a very high resistivity and a very small dielectric constant (Fig. 4.14 ii(a)). If we compare thin films deposited at X=7 and 8 we come to know that resistivity of films grown at X=8 is higher as compared to tin film deposited at X=7 and reverse is the case with carrier concentration. But thin film deposited at X=8 shows a better I-V response which is due to high charge mobility and its negative dielectric loss (Fig. 4.14 iii(d)).

If we look at the Hall measurement results for single, di and tri-layer films on Si substrate we come to know that the mobility increases as number of layers are increased. It means each layers contributes to increase the mobility. Single, di and tri-

layer films grown on polished Si also show behaviour different as compared to films grown on unpolished Si.

Table 5.2: Sheet resistance, resistivity, carrier concentration and mobility measurements calculated through hall effect measurement.

Sample code	Sheet resistance (Ω/cm^2)	Resistivity (Ω/cm)	Film Type	Sheet carrier concentration (cm^{-2})	Bulk carrier concentration (cm^{-3})	Mobility (cm^2/Vs)
NSi6-5	4.03×10^5	123	p-type	2.73×10^{10}	1.76×10^{15}	90
NSi6-10	3.23×10^5	9.74	p-type	4.28×10^{10}	1.81×10^{15}	200
NSi6-15	8×10^4	15	p-type	5.27×10^{10}	2.04×10^{15}	215
N´Si6-5	1.57×10^5	22.5	p-type	1.77×10^{10}	7.99×10^{14}	700
N´Si6-10	2.56×10^5	56.3	p-type	2.30×10^{10}	1.35×10^{15}	150
N´Si6-15	5.1×10^4	11.7	p-type	1.89×10^{12}	1.09×10^{16}	257

Di-layer film deposited on polished Si substrate has maximum resistance & resistivity and minimum carrier concentration & mobility therefore the current is minimum in this film (Fig. 5.4). also the defects present in this film seem to play a role in increasing the resistance and resistivity although it shows quantum confinement in Ge as confirmed through PL spectra (Fig. 4.19 b). Tri-layer film deposited on polished Si substrate shows minimum resistance, resistivity and maximum carrier concentration. Emission peaks in PL spectra of this film is the indication of Ge quantum dots formation resulting in enhanced charge carrier concentration and I-V response as compared to di and single layer films. Better I-V response can also be due to the amorphous nature of film in which defects would have contributed to increase the carrier concentration. Di-layer film has comparatively high resistance as compared to tri-layer film. PL spectrum of delayer film shows presence of defects which contribute to increase the resistance of film.

Thin films deposited on unpolished Si substrate also show that the charge carrier concentration increases with the addition of each multilayer Table 5.2). Resistivity of the tri-layer film is minimum and it has highest charge carrier concentration. Tri-layer

film has been confirmed to show quantum confinement as confirmed through PL therefore it has higher charge carrier concentration which leads to heavy current as compared to di and single-layer films. Di-layer film deposited on unpolished Si substrate has maximum resistance & resistivity and minimum carrier concentration & mobility therefore the current is minimum in this film (Fig. 5.4). Also the defects present in this film seem to play a role in increasing the resistance and resistivity although it shows quantum confinement in Ge as confirmed through PL spectra (Fig. 4.19 b). Single layer film has carrier concentration and mobility high as compared to double layer film and smaller than the tri-layer film. The film has a highest dielectric constant (Fig. 4.16 ii) therefore will produce highest amount of e-h pairs. As well as it has a negative dielectric loss (Fig. 4.16 iii) due to which defects seem to increase charge carrier concentration in this film as compared to di-layer film which is responsible for a better I-V response also.

Substrate has been observed to effect the electrical response in light and dark. Films which are grown on n-type Si are photo responsive and those deposited at X=6 cm show 22% increase in current under light as compared to that in dark. Whereas electrical response is same in dark and light in films on p-type Si substrate. Also films on polished n-type Si in three layers show a good electrical response in dark and it increases 3 times in the presence of light. Although the charge carrier concentration in dark is very high in these films (Table. 5.2) and it increases in light. It is confirmed by the ellipsometric data as these films have low n, high ε_1 and negative ε_2 which may be due to high defects/ dislocation density (Table. 3.3) contributing to increase in charge carrier concentration and a good photo response.

Chapter 6

This chapter gives the detailed conclusions of the experimental results and their outcomes.

CONCLUSIONS

Chapter 6

6 Conclusions

In this study TiO_2-Ge composite thin films were initially deposited by PLD on n-type Si (100) and p-type Si (111) substrate with a variation in target-substrate distance (X) for 30 minutes. Thin films were deposited at a target-substrate distance X= 5,6,7 and 8 cm. Which were further studied to find an appropriate distance and substrate for which thin film will show better optoelectronic response. It was found that thin films deposited on n-type Si substrate at X= 6 cm showed a better optoelectronic response as compares to thin films deposited at X= 5,7 and 8 cm. In the second phase single, di and tri-layer films were deposited on polished and unpolished n-type Si (100) substrate at a target-substrate distance of 6 cm.

Optical and electrical properties of thin films depend on deposition parameters (target-substrate seperation) that rely on ionic mass of ablated material. Since Ge is a heavier atom (Z= 72.64 u), it rapidly loseses energy resulting in decrease in Ge concentration at a higher distance during plasma expansion. As ionic mass of TiO_2 is smaller as compared to that of Ge therefore more concentration of TiO_2 ions is present in the thin films. Laser ablation is a complex process undergoing ionic sputtering, melting and hydrodynamic sputtering. Also plasma undergoes through multiple physical phenomenas as it drifts away like ionic species go through multiple collisions, condensation etc. At different distances plasma is in different states, therefore target-substrate distance highly effects thin film morphology, crystalline structure and concentration of constituent species (in case if multicomponent target).

This study shows that the crystallinity of thin films depends on the substrate orientation as films on n-type Si (100) have shown better crystallinity. Main reason for this effect depends on the misfit factor observed between thin film and the substrate. Misfit factor observed for films on Si (100) was smaller as compared to those on Si (111). Smaller misfit factor is responsible for the formation of strained crystalline films which follow S-K growth mechanism, leading to the formation of Ge quantum dots in the films.

Ge is least identified in XRD but is clearly observed in Raman spectroscopy showing peaks related to cubic crystalline form which confirmed the formation of TiO_2- Ge composite. Raman spectroscopy which has a better signal to noise ratio identified Ge whereas no peak related to Ge were observed in XRD, which shows that Ge structures were so small that their size was small below the detection threshold of XRD.

Ge concentration has an inverse relation with target-substrate distance as confirmed through EDX spectra. Thin films deposited at X= 5 cm had a higher Ge concentration ~ 25 % as compared to the target (Ge concentration = 20%). This higher concentration in thin film is due to the backscattering of Ge by the species in plume. Thin film deposited at X=5 showed a poor light absorbance and PL spectrum. It also shows a poor I-V response although Ge concentration is very high in it ~ 25% ; which is due to the small dielectric constant as found through ellipsometry data.

Among all the samples fabricated on n-type Si wafer it can be observed that thin film deposited at X=6 (Sample code NSi6-30) shows better optoelectronic properties. This film was crystalline in nature and UV/ Vis spectroscopy showed that it has absorbance in UV, Vis and IR region of spectrum. Direct and indirect absorption transitions measured through Tauc plot show that the transitions lying in visible region are in fact due to QCE in Ge, reconfirmed through PL spectrum. Multiple transition lying in visible region showed that multi-sized Ge quantum dots were present in TiO_2 matrix. Ellipsometry data shows almost stable dielectric loss & dielectric constant in response to electromagnetic waves (λ= 300-800 nm) incident on it. This film also shows a good I-V response in dark and an improved I-V response in light. The I-V response of this film was higher as compared to thin films deposited at X= 5. 7 and 8 cm. Thus it can be concluded that thin film deposited at X=6 cm shows better optoelectronic properties therefore it can be used as a potential candidate for optoelectronic applications like light sensor, photovoltaics, photo switches etc.

Thin films deposited at X=6 cm on p-type Si substrate also exhibited a good I-V response in dark but no change in I-V response was observed when recorded in light. A good I-V response in dark was due to the fact that this sample has a positive dielectric constant and negative dielectric loss. Therefore the defects will add additional charge in the material for conduction. As the light absorbance for this material is very low

therefore a large part of light incident on it will either reflect back or will transmit through it. So absorbed light will not produce any change in the electronic and electrical response.

Therefore thin film deposited at X= 6 cm show a good I-V response in dark and light on polished n-type Si (100). It means that thin films deposited at X= 6 cm on n-type Si substrates show better optoelectronic properties as compared to films on p-type Si (111). So n-type Si can be considered as suitable substrate to produce thin films having good optoelectronic properties. As well as X=6 is found to be optimum distance to produce Ge quantum dots. Therefore next batch of samples was fabricated at X=6 on polished and unpolished n-type Si substrate (100).

Single, di and tri-layer films on n-type unpolished and polished Si substrate were studied for optoelectronic response. Tri-layer films deposited on polished and unpolished Si substrate show a good I-V response in dark as compared to single and di-layer films. Trilayer film on polished Si substrate shows an improved I-V response in light also. Which is due to the fact that this film has shown QCE in Ge as observed through PL spectrum in visible region and UV/Vis absorption transition in visible region. Negative dielectric loss also shows the contribution of electrons from defects to the tri-layer film.

Dilayer film deposited on polished Si wafer does not show good optoelectronic properties as defects present in thin film absorb most of light, therefore cannot contribute to the current. As well as larger number if e-h pairs (i.e. higher dielectric constant) will be generated when light of shorter wavelength is incident on these films and small number of e-h pairs (i.e. smaller dielectric constant) will be generated if light of higher wavelength is used. Dielectric loss is higher for the light source of smaller wavelength and becomes zero at higher wavelength. Over all we can say when higher number of e-h pairs are generated recombination also occurs and when recombination rate becomes zero, e-h pair production rate is small. Therefore current for whole spectrum remains small. Single layer film on polished Si substrate although shows quantum confinement but the presence of brookite and anatase structure makes it less conductive.

Thin films deposited on unpolished Si substrate show a different behaviour as compared to those on polished Si substrate. Single and tri-layer film deposited on unpolished Si substrate although show quantum confinement effect but the I-V response in dark and light of tri-layer film is better as compared to the single-layer film. As the absorption of light is less in single-layer film therefore I-V response in light will also be smaller.

Poor I-V response in di-layer film deposited on n-type unpolished Si substrate can be attributed to the presence of defects which show PL in visible region. Negligibly small dielectric

REFERENCES

References

[1] S. Chatterjee, A. Goyal and S. I. Shah, *"Inorganic Nanocomposites for the Next Generation Photovoltaics,"* Mater. Lett. **60,** 3541-3543, 2006.

[2] A. Slav, *"Optical Characterization Of TiO_2-Ge Nanocomposite Films Obtained By Reactive Magnetron Sputtering,"* Dig. J. Nanomater. Biostruct. **6,** 915-920, 2011.

[3] G. D. Jaffery, "*Introduction to Electrodynamics"*. New Jersey, USA: Prentice Hall International Ltd, 1999.

[4] S. Das, D. Liu, J. B. Park and Y.-B. Hahn, *"Metal-ion Doped p-type TiO_2 Thin Films and Their Applications for Heterojunction Devices,"* J. Alloys Compd. **553,** 188-193, 2013.

[5] D. Yandong, F. Nianqing, L. Qiuping, F. Yanyan, Z. Xiaowen, Z. Jingbo and L. Yuan, *"Sn-Doped TiO_2 Photoanode for Dye-Sensitized Solar Cells,"* J. Phys. Chem. C **116,** 8888-8893, 2016.

[6] D. M. King, X. Du, A. S. Cavanagh and A. W. Weimer, *"Quantum Confinement in Amorphous TiO_2 Films Studied Via Atomic Layer Deposition,"* Nanotech. **19,** 445401, 2008.

[7] P. Henrique Cury Camargo, K. Gundappa Satyanarayana and F. Wypych, *"Nanocomposites: synthesis, structure, properties and new application opportunities,"* Mater. Res. **12,** 1-39, 2009.

[8] K. L. Chopra, "*Thin film phenomena"*: McGraw-Hill, New York., 1969.

[9] J. K. Hirvonen, *"Ion Beam Assisted Thin Film Deposition,"* Mater. Sci. Rep. **6,** 215-274, 1991.

[10] S. Kukushkin and A. V. Osipov, *"New Phase Formation on Solid Surfaces and Thin Film Condensation,"* Prog. Surf. Sci. **51,** 1-107, 1996.

[11] J. Lloyd, *"Electromigration in Thin Film Conductors,"* Semicond. Sci. Technol. **12,** 1177, 1997.

[12] L. Kronik and Y. Shapira, *"Surface Photovoltage Phenomena: Theory, Experiment, and Applications,"* Surf. Sci. Rep. **37,** 1-206, 1999.

[13] M. J. McCann, K. R. Catchpole, K. J. Weber and A. W. Blakers, *"A Review of Thin-Film Crystalline Silicon for Solar Cell Applications. Part 1: Native Substrates,"* Sol. Energy Mater. Sol. Cells **68,** 135-171, 2001.

[14] O. R. Monteiro, *"Thin Film Synthesis by Energetic Condensation 1,"* Annu. Rev. Mater. Res, **31,** 111-137, 2001.

[15] C. Ratsch and J. Venables, *"Nucleation Theory and the Early Stages of Thin Film Growth,"* J. Vac. Sci. Technol., A **21,** S96-S109, 2003.

[16] M. Kemell, M. Ritala and M. Leskelä, *"Thin Film Deposition Methods for $CuInSe_2$ Solar Cells,"* Crit. Rev. Solid State Mater. Sci. **30,** 1-31, 2005.

[17] I. Aleksandrov, G. M. Melchor, D. Vinogradov and M. Petrov, *"Correlation between the Dopant Concentration and the Anharmonicity Of Bending Vibrations in Silica Optical Fibers,"* Tech. Phys. Lett. **32,** 442-444, 2006.

[18] M. V. Ganduglia-Pirovano, A. Hofmann and J. Sauer, *"Oxygen Vacancies in Transition Metal And Rare Earth Oxides: Current State of Understanding and Remaining Challenges,"* Surf. Sci. Rep. **62,** 219-270, 2007.

[19] N. S. Rao, S. Dhamodaran, A. Pathak, P. Kulriya, Y. Mishra, F. Singh, D. Kabiraj, J. Pivin and D. Avasthi, *"Structural Studies of Ge Nanocrystals Embedded in SiO_2 Matrix,"* Nucl. Instrum. Methods Phys. Res. Sect. B: Beam Interact. Mater. At. **264,** 249-253, 2007.

[20] A. Boyd, H. Duffy, R. McCann and B. Meenan, *"Sputter Deposition of Calcium Phosphate/Titanium Dioxide Hybrid Thin Films,"* Mater. Sci. Eng., C **28,** 228-236, 2008.

[21] B. H. Lee, M. Y. Song, S.-Y. Jang, S. M. Jo, S.-Y. Kwak and D. Y. Kim, *"Charge Transport Characteristics of High Efficiency Dye-Sensitized Solar Cells Based on Electrospun TiO_2 Nanorod Photoelectrodes,"* J. Phys. Chem. C **113,** 21453-21457, 2009.

[22] A. Elshabini, A. A. Elshabini-Riad and F. D. Barlow, "*Thin Film Technology Handbook"*: McGraw-Hill Professional, 1998.

[23] L.I. Maissel and R. Glang, "*Handbook of Thin Film Technology "*. New York, USA: McGraw-Hill, 1970.

[24] J.L. Vossen and W. Kern, "*Thin Film Processes"*: Academic Press, New York, 1978.

[25] S. L. Chuang, "*Physics of Optoelectronic Devices"*. USA: John Wiley & Sons. Inc. , 1995.

[26] D. A. B. Miller., "*Semiconductor Optoelectronic Devices* ", S. University, Ed. Stanford University, 248, 1997.

[27] E. A. Muljarov, E. A. Zhukov, V. S. Dneprovskii and Y. Masumoto, *"Dielectrically Enhanced Excitons in Semiconductor-Insulator Quantum Wires: Theory and Experiment,"* Phys. Rev. B **62,** 13, 2000.

[28] N. A. Gippius, A. L. Yablonskii, A. B. Dzyubenko, S. G. Tikhodeev, L. V. Kulik, V. D. Kulakovskii and A. Forchel, *"Excitons in Near-Surface Quantum*

Wells in Magnetic Fields: Experiment and Theory," J. Appl. Phys. **83,** 5410-5417, 1998.

[29] A. W. Achtstein, A. V. Prudnikau, M. V. Ermolenko, L. I. Gurinovich, S. V. Gaponenko, U. Woggon, A. V. Baranov, M. Y. Leonov, I. D. Rukhlenko, A. V. Fedorov and M. V. Artemyev, *"Electroabsorption by 0D, 1D and 2D Nanocrystals: A Comparative Study of CdSe Colloidal Quantum Dots, Nanorods and Nanoplatelets,"* ACSNano **8,** 9, 2014.

[30] S. C. Ghosh, C. Thanachayanont and J. Dutta, *"Studies on Zinc sulphide Nanoparticles for Field Emission Devices,"* in 2004 1st International Conference on Electrical Engineering/ Electronics, Computer, Telecommunications and Information Technology, Thailand, 1-4, 2004.

[31] M. Zavelani-Rossi, R. Krahne, G. D. Valle, S. Longhi, I. R. Franchini, S. Girardo, F. Scotognella, D. Pisignano, L. Manna, G. Lanzani and F. Tassone, *"Self-Assembled CdSe/CdS Nanorod Micro-Lasers Fabricated from Solution by Capillary Jet Deposition,"* Laser Photonic Rev. 6, 2012.

[32] M. Allione, A. Ballester, H. Li, A. Comin, J. L. Movilla, J. I. Climente, L. Manna and I. Moreels, *"Two-Photon-Induced Blue Shift of Core and Shell Optical Transitions in Colloidal CdSe/CdS Quasi-Type II Quantum Rods,"* ACSNano **7,** 10, 2013.

[33] G. A. Muller, J. B. Cook, H.-S. Kim, S. H. Tolbert and B. Dunn, *"High Performance Pseudocapacitor Based on 2D Layered Metal Chalcogenide Nanocrystals,"* Nano Lett. **15,** 7, 2015.

[34] H. Nishimura, K. Ritchie, R. S. Kasai, M. Goto, N. Morone, H. Sugimura, K. Tanaka, I. Sase, A. Yoshimura, Y. Nakano, T. K. Fujiwara and A. Kusumi, *"Biocompatible Fluorescent Silicon Nanocrystals for Single-Molecule Tracking and Fluorescence Imaging,"* J. Cell Biol. **202,** 23, 2013.

[35] S. Ithurria, M. D. Tessier, B. Mahler, R. P. S. M. Lobo, B. Dubertret and A. L. Efros, *"Colloidal Nanoplatelets with Two-Dimensional Electronic Structure,"* Nat. Mater. **10,** 936-941, 2011.

[36] A. G. Vitukhnovsky, V. S. Lebedev, A. S. Selyukov, A. A. Vashchenko, R. B. Vasiliev and M. S. Sokolikova, *"Electroluminescence from Colloidal Semiconductor CdSe Nanoplatelets in Hybrid Organic-Inorganic Light Emitting Diode,"* Chem. Phys. Lett. **619,** 4, 2015.

[37] F. D. Stasio, J. Q. Grim, V. Lesnyak, P. Rastogi, L. Manna, I. Moreels and R. Krahne, *"Single-Mode Lasing from Colloidal Water-Soluble CdSe/CdS Quantum Dot-in-Rods,"* Small 7, 2014.

[38] S. Jeong, D. Yoo, J.-t. Jang, M. Kim and J. Cheon, *"Well-Defined Colloidal 2D Layered Transition-Metal Chalcogenide Nanocrystals Via Generalized Synthetic Protocols,"* J. Am. Chem. Soc. **134,** 4, 2012.

[39] J. William D. Callister, "*Fundamentals of Materials Science and Engineering"*, 5th ed. New York, USA: John Wiley & Sons, Inc., 2001.

[40] C.-X. Tian, J.-Q. Du, X.-H. Chen, W.-P. Ma, Z.-Q. Luo, X.-Z. Cheng, H.-F. Hu and D.-J. Liu, *"Influence of Hydrolysis in Sulfate Process on Titania Pigment Producing,"* Trans. Nonferrous Matal. Soc. China **19, Supplement 3,** s829-s833, 2009.

[41] T. Viseu, B. Almeida, M. Stchakovsky, B. Drevillon, M. Ferreira and J. Sousa, *"Optical Characterisation of Anatase: A Comparative Study of the Bulk Crystal and the Polycrystalline Thin Film,"* Thin Solid Films **401,** 216-224, 2001.

[42] D. Tsiulyanua, S. Mariana, H. Liessb and I. Eiseleb, *"Chalcogenide Based Gas Sensors,"* J. Optoelectro. Adv. Mater. **5,** 1349-1354, 2003.

[43] E. Sardella, F. D. Liuzzi, R. Comparelli, N. Depalo, M. Striccoli, M. L. Curri, A. Agostiano, P. Favia and R. d'Agostino, *"Chemically Directed Assembling of Functionalized Luminescent Nanocrystals onto Plasma Modified Substrates Towards Sensing and Optoelectronic Applications,"* Plasma Process. Polym. **6,** S870-S875, 2009.

[44] J. Liu, H. Kim, O. Hul'Ko, Y. Xie, S. Sahni, P. Bandaru and E. Yablonovitch, *"Ge Films Grown on Si Substrates by Molecular-Beam Epitaxy Below 450 C,"* J. Appl. Phys. **96,** 916-918, 2004.

[45] T. Berger, T. Lana-Villarreal, D. Monllor-Satoca and R. Gomez, *"The Electrochemistry of Transparent Quantum Size Rutile Nanowire Thin Films Prepared by One-Step Low Temperature Chemical Bath Deposition,"* Chem. Phys. Lett. **447,** 91-95, 2007.

[46] E. Zumelzu, F. Rull and C. Ortega, *"Titanium Dioxide Performance in Polyethylene Teraphthalate Protective Coatings on Electrolytic Chromium Coated Steels,"* Surf. Eng. **25,** 111-115, 2009.

[47] J. Carneiro, V. Teixeira, A. Portinha, A. Magalhaes, P. Coutinho, C. Tavares and R. Newton, *"Iron-doped Photocatalytic TiO_2 Sputtered Coatings on Plastics for Self-Cleaning Applications,"* Mater. Sci. Eng: B **138,** 144-150, 2007.

[48] H.-S. Bang, H.-S. Bang and Y.-K. Lee, *"The Functional TiO_2-Biodegradable Plastic Composite Material Produced by HVOF Spraying Process,"* J. Nanosc. Nanotech. **7,** 3830-3833, 2007.

[49] J. Kaldellis, P. Kostas and A. Filios, *"Minimization of the Energy Storage Requirements of a Stand Alone Wind Power Installation by means of Photovoltaic Panels,"* Wind Energy **9,** 383-397, 2006.

[50] Kociolek-Balawejder, Elzbieta Szymczyk and Marta, *"Titanium Dioxide as Pigment and Photocatalyst,"* Przem. Chem. **86,** 1179-1188, 2007.

[51] N. Badea, M. Giurginca and A. Meghea, *"Complex Effects of Sunscreen Agents and Flavonoid Antioxidants Devoted to Enhance Photoprotection of Dermal Tissues,"* Mol. Cryst. Liq. Cryst. **486,** 183/[1225]-192/[1234], 2008.

[52] S. Boisnic, M. C. Branchet-Gumila, C. Merial-Kieny and T. Nocera, *"Efficacy of Sunscreens Containing Pre-Tocopheryl in a Surviving Human Skin Model Submitted to UV A and B radiation,"* Skin pharmacology and physiology **18,** 201-8, 2005.

[53] R. Capote, J. L. Alonso-Lebrero, F. Garcia, A. Brieva, J. P. Pivel and S. Gonzalez, *"Polypodium Leucotomos Extract Inhibits Ttransurocanic Acid Photoisomerization and Photodecomposition,"* J. Photochem. Photobiol. B: Biol. **82,** 173-9, 2006.

[54] M. E. Carlotti, E. Ugazio, S. Sapino, I. Fenoglio, G. Greco and B. Fubini, *"Role of Particle Coating in Controlling Skin Damage Photoinduced by Titania Nanoparticles,"* Free Radical Res. **43,** 312-322, 2009.

[55] M. E. Carlotti, E. Ugazio, L. Gastaldi, S. Sapino, D. Vione, I. Fenoglio and B. Fubini, *"Specific Effects of Single Antioxidants in the Lipid Peroxidation Caused by Nano-Titania Used in Sunscreen Lotions,"* J. Photochem. Photobiol. B: Biol. **96,** 130-135, 2009.

[56] D. Dondi, A. Albini and N. Serpone, *"Interactions Between Different Solar UVB/UVA Filters Contained in Commercial Suncreams and Consequent Loss of Uv Protection,"* Photochemical & Photobiological Sciences **5,** 835-843, 2006.

[57] R. Dunford, A. Salinaro, L. Cai, N. Serpone, S. Horikoshi, H. Hidaka and J. Knowland, *"Chemical Oxidation and DNA Damage Catalysed by Inorganic Sunscreen Ingredients,"* FEBS Lett. **418,** 87-90, 1997.

[58] M. Carlotti, S. Sapino, D. Vione, C. Minero, E. Peira and M. Trotta, *"Study on the Photodegradation of Salicylic Acid in Different Vehicles in the Absence and in the Presence of TiO_2,"* J. Dispersion Sci. Technol. **28,** 805-818, 2007.

[59] P. Lansåker, J. Backholm, G. Niklasson and C.-G. Granqvist, *"TiO_2/Au/TiO_2 Multilayer Thin Films: Novel Metal-Based Transparent Conductors for Electrochromic Devices,"* Thin Solid Films **518,** 1225-1229, 2009.

[60] E. Zelazowska and E. Rysiakiewicz-Pasek, *"Thin TiO_2 Films for an Electrochromic System,"* Opt. Mater. **31,** 1802-1804, 2009.

[61] S. Balaji, A.-S. Albert, Y. Djaoued and R. Brüning, *"Micro-Raman Spectroscopic Characterization of a Tunable Electrochromic Device for Application in Smart Windows,"* J. Raman Spectrosc. **40,** 92-100, 2009.

[62] A. Nattestad, A. J. Mozer, M. K. Fischer, Y.-B. Cheng, A. Mishra, P. Bäuerle and U. Bach, *"Highly Efficient Photocathodes for Dye-Sensitized Tandem Solar Cells,"* Nat. Mater. **9,** 31-35, 2010.

[63] S.-H. Kang, C. K. Kumar, Z. Lee, K.-H. Kim, C. Huh and E.-T. Kim, *"Quantum-Dot Light-Emitting Diodes Utilizing CdSe/ZnS Nanocrystals Embedded in TiO_2 Thin Film,"* Appl. Phys. Lett. **93,** 191116, 2008.

[64] G. Mincuzzi, L. Vesce, A. Reale, A. Di Carlo and T. M. Brown, *"Efficient Sintering of Nanocrystalline Titanium Dioxide Films for Dye Solar Cells Via Raster Scanning Laser,"* Appl. Phys. Lett. **95,** 103312, 2009.

[65] N. Alexaki, T. Stergiopoulos, A. Kontos, D. Tsoukleris, A. Katsoulidis, P. Pomonis, D. LeClere, P. Skeldon, G. Thompson and P. Falaras, *"Mesoporous Titania Nanocrystals Prepared Using Hexadecylamine Surfactant Template: Crystallization Progress Monitoring, Morphological Characterization and Application In Dye-Sensitized Solar Cells,"* Microporous Mesoporous Mater. **124,** 52-58, 2009.

[66] A. Patrocinio, L. Paterno and N. M. Iha, *"Layer-by-layer TiO_2 Films as Efficient Blocking Layers in Dye-sensitized Solar Cells,"* J. Photochem. Photobiol. A: Chem. **205,** 23-27, 2009.

[67] J.-H. Yum, P. Chen, M. Grätzel and M. K. Nazeeruddin, *"Recent Developments in Solid-State Dye-Sensitized Solar Cells,"* ChemSusChem. **1,** 699-707, 2008.

[68] M. Hossain, S. Biswas and T. Takahashi, *"The Effect of Sputter-Deposited TiO_2 Passivating Layer on The Performance of Dye-Sensitized Solar Cells Based on Sol–Gel Derived Photoelectrode,"* Thin Solid Films **517,** 1294-1300, 2008.

[69] G. Notton, V. Lazarov and L. Stoyanov, *"Optimal Sizing of a Grid-Connected Pv System for Various Pv Module Technologies and Inclinations, Inverter Efficiency Characteristics and Locations,"* Renewable Energy **35,** 541-554, 2010.

[70] J. Sambrano, L. Vasconcellos, J. Martins, M. Santos, E. Longo and A. Beltran, *"A Theoretical Analysis on Electronic Structure of the (110) Surface of TiO_2–SnO_2 Mixed Oxide,"* J. Mol. Struct. **629,** 307-314, 2003.

[71] V. Palkar, S. Purandare, P. Apte, R. Pinto and M. Multani, *"$PbTiO_3$ Thin Films on Si (100) as Potential Varistor Material,"* Appl. Phys. Lett. **71,** 3637-3639, 1997.

[72] L. Castaneda, *"Influence of Colloidal Silver Nanoparticles on the Performance of Novel Flower-Like Titanium Dioxide Oxygen Sensor,"* Sens. Mater **21,** 25-36, 2009.

[73] L. Castaneda, A. Maldonado and M. d. l. L. Olvera, *"Sensing Properties of Chemically Sprayed TiO_2 Thin Films Using Ni, Ir, and Rh as Catalysts,"* Sensors Actuators B: Chem. **133,** 687-693, 2008.

[74] Z. Seeley, Y. J. Choi and S. Bose, *"Citrate–Nitrate Synthesis of Nano-Structured Titanium Doxide Ceramics for Gas Sensors,"* Sensors Actuators B: Chem. **140,** 98-103, 2009.

[75] M. Mohammadi and D. Fray, *"Development of nanocrystalline TiO_2–Er_2O_3 and TiO_2–Ta_2O_5 Thin Film Gas Sensors: Controlling the Physical and Sensing Properties,"* Sensors Actuators B: Chem. **141,** 76-84, 2009.

[76] B. Mecheri, A. D'Epifanio, E. Traversa and S. Licoccia, *"Sulfonated Polyether Ether Ketone and Hydrated Tin Oxide Proton Conducting Composites for Direct Methanol Fuel Cell Applications,"* J. Power Sources **178,** 554-560, 2008.

[77] I. Fasaki, I. Hotovy, A. Rehakova, J. Hotovy, V. Rehacek, M. Kompitsas and F. Roubani-Kalantzopoulou, *"Effects of Post-Deposition Surface Treatment on the Optical, Structural And Hydrogen Sensing Properties of TiO_2 Thin Films,"* Thin Solid Films **518,** 1103-1108, 2009.

[78] R.-H. Lee and Y.-W. Huang, *"Enhancing the Photovoltaic Performances of Dye-Sensitized Solar-Cells by Modifying the TiO_2 Electrode-Sensitized Dye Interface,"* Thin Solid Films **517,** 5903-5908, 2009.

[79] T. Brown, F. De Rossi, F. Di Giacomo, G. Mincuzzi, V. Zardetto, A. Reale and A. Di Carlo, *"Progress in Flexible Dye Solar Cell Materials, Processes and Devices,"* J. Mater. Chem. A **2,** 10788-10817, 2014.

[80] W. Loh, J. Wang, J. Ye, R. Yang, H. Nguyen, K. Chua, J. Song, T. Loh, Y. Xiong and S. Lee, *"Impact of Local Strain From Selective Epitaxial Germanium with Thin Si/SiGe Buffer on high-Performance Pin Photodetectors With a Low Thermal Budget,"* IEEE Electron Device Lett. **28,** 984-986, 2007.

[81] M. Okada, K. Tajima, Y. Yamada and K. Yoshimura, *"Photocatalytic Performance of Very Thin TiO_2/SnO_2 Stacked-Film Prepared by Magnetron Sputtering,"* Vacuum **83,** 688-690, 2008.

[82] Y. Nakamura, K. Watanabe, Y. Fukuzawa and M. Ichikawa, *"Observation of the Quantum-Confinement Effect in Individual Ge Nanocrystals on Oxidized Si Substrates Using Scanning Tunneling Spectroscopy,"* Appl. Phys. Lett. **87,** 3119, 2005.

[83] Y. Nakamura, M. Ichikawa, K. Watanabe and Y. Hatsugai, *"Quantum Fluctuation Of Tunneling Current in Individual Ge Quantum Dots Induced by a Single-Electron Transfer,"* Appl. Phys. Lett. **90,** 153104, 2007.

[84] P. Caldelas, A. G. Rolo, A. Chahboun, S. Foss, S. Levichev, T. Finstad, M. Gomes and O. Conde, *"Structural and Optical Properties of Ge Nanocrystals Embedded in Al_2O_3,"* J. Nanosc. Nanotech. **8,** 572-576, 2008.

[85] L. J. Lauhon, M. S. Gudiksen, D. Wang and C. M. Lieber, *"Epitaxial Core–Shell and Core–Multishell Nanowire Heterostructures,"* Nature **420,** 57-61, 2002.

[86] A. Khakifirooz and D. A. Antoniadis, *"On the Electron Mobility in Ultrathin SOI and GOI,"* IEEE Electron Device Lett. **25,** 80-82, 2004.

[87] X. An, R. Huang, X. Zhang and Y. Wang, *"Comparison of Device Performance and Scaling Capability of Thin-Body GOI and SOI MOSFETs,"* Semicond. Sci. Technol. **20,** 1034, 2005.

[88] M. Deshmukh and J. Nagaraju, *"Measurement of Silicon and GaAs/Ge Solar Cell Device Parameters,"* Sol. Energy Mater. Sol. Cells **89,** 403-408, 2005.

[89] R. Wang, Z. Guo and G. Wang, *"Low-Energy Proton Irradiation Effects on GaAs/Ge Solar Cells,"* Sol. Energy Mater. Sol. Cells **90,** 1052-1057, 2006.

[90] A. Du Pasquier, D. D. Mastrogiovanni, L. A. Klein, T. Wang and E. Garfunkel, *"Photoinduced Charge Transfer Between Poly (3-Hexylthiophene) and Germanium Nanowires,"* Appl. Phys. Lett. **91,** 183501-183501, 2007.

[91] H. Gerung, Y. Zhao, L. Wang, R. K. Jain, T. J. Boyle, C. J. Brinker and S. M. Han, *"Two-Photon Absorption of Matrix-Free Ge Nanocrystals,"* Appl. Phys. Lett. **89,** 111107, 2006.

[92] B. A. Hernandez-Sanchez, T. J. Boyle, T. N. Lambert, S. D. Daniel-Taylor, J. M. Oliver, B. S. Wilson, D. S. Lidke and N. L. Andrews, *"Synthesizing Biofunctionalized Nanoparticles to Image Cell Signaling Pathways,"* IEEE Trans Nanobioscience **5,** 222-30, 2006.

[93] T. N. Lambert, N. L. Andrews, H. Gerung, T. J. Boyle, J. M. Oliver, B. S. Wilson and S. M. Han, *"Water Soluble Germanium Nanocrystals: Cell Recognition and Near Infrared Photothermal Conversion Properties,"* Small **3,** 691-699, 2007.

[94] M. Kanoun, C. Busseret, A. Poncet, A. Souifi, T. Baron and E. Gautier, *"Electronic Properties of Ge Nanocrystals for Non Volatile Memory Applications,"* Solid·State Electron. **50,** 1310-1314, 2006.

[95] K. Gacem, A. E. Hdiy, M. Troyon, I. Berbezier, P. D. Szkutnik, A. Karmous and A. Ronda, *"Memory and Coulomb Blockade Effects in Germanium Nanocrystals Embedded in Amorphous Silicon on Silicon Dioxide,"* J. Appl. Phys. **102,** 093704, 2007.

[96] C.-H. Tu, T.-C. Chang, P.-T. Liu, C.-F. Weng, H.-C. Liu, L.-T. Chang, S.-K. Lee, W.-R. Chen, S. M. Sze and C.-Y. Chang, *"Formation of Germanium Nanocrystals Embedded in a Silicon-Oxygen-Nitride Layer,"* J. Electrochem. Soc. **154,** H435-H439, 2007.

[97] G. Gu, M. Burghard, G.-T. Kim, G. Düsberg, P. Chiu, V. Krstic, S. Roth and W. Han, *"Growth and Electrical Transport of Germanium Nanowires,"* J. Appl. Phys. **90,** 5747-5751, 2001.

[98] D. Carder and A. Markwitz, *"Field Emission Measured from Nanostructured Germanium and Silicon Thin Films,"* Appl. Surf. Sci. **256,** 1003-1005, 2009.

[99] C. Bostedt, T. Van Buuren, T. Willey, N. Franco, L. Terminello, C. Heske and T. Möller, *"Strong Quantum-Confinement Effects in the Conduction Band of Germanium Nanocrystals,"* Appl. Phys. Lett. **84,** 4056-4058, 2004.

[100] S. Tripathi, R. Brajpuriya, A. Sharma, A. Soni, G. Okram, S. Chaudhari and T. Shripathi, *"Thickness Dependent Structural, Electronic and Optical Properties of Ge Nanostructures,"* J. Nanosc. Nanotech. **8,** 2955-2963, 2008.

[101] G. Kartopu, A. Sapelkin, V. Karavanskii, U. Serincan and R. Turan, *"Structural and Optical Properties of Porous Nanocrystalline Ge,"* J. Appl. Phys. **103,** 113518, 2008.

[102] M. Kumar, H. Mavi, S. Rath, A. Shukla and V. Vankar, *"Fabrication of Nanopatterned Germanium Surface by Laser-Induced Etching: AFM, Raman and PL Studies,"* Physica. E: Low Dim. Sys. NanoStruct. **40,** 2904-2910, 2008.

[103] M. T. Bohr, *"Interconnect Scaling the Real Limiter to High Performance ULSI,"* International Electron Devices Meeting (IEDM) 241-244, 1995.

[104] S.-L. Cheng, J. Lu, G. Shambat, H.-Y. Yu, K. Saraswat, J. Vuckovic and Y. Nishi, *"Room Temperature 1.6 μm Electroluminescence from Ge Light Emitting Diode on Si Substrate,"* Opt. Express **17,** 10019-10024, 2009.

[105] J. Xia, Y. Takeda, N. Usami, T. Maruizumi and Y. Shiraki, *"Room-Temperature Electroluminescence from Si Microdisks with Ge Quantum Dots,"* Opt. Express **18,** 13945-13950, 2010.

[106] P. Chaisakul, D. Marris-Morini, G. Isella, D. Chrastina, N. Izard, X. Le Roux, S. Edmond, J.-R. Coudevylle and L. Vivien, *"Room Temperature Direct Gap Electroluminescence from Ge/$Si_{0.15}Ge_{0.85}$ Multiple Quantum Well Waveguide,"* Appl. Phys. Lett. **99,** 141106, 2011.

[107] E. Gorokhov, V. Volodin, D. Marin, D. Orekhov, A. Cherkov, A. Gutakovskii, V. Shvets, A. Borisov and M. Efremov, *"Effect of Quantum Confinement on Optical Properties of Ge Nanocrystals in GeO_2 Films,"* Semiconductors **39,** 1168-1175, 2005.

[108] S. Chatterjee, *"Titania-germanium Nanocomposite as a Photovoltaic Material,"* Solar Energy **82,** 95-99, 2008.

[109] S. Chatterjee, *"Titania–germanium Nanocomposite as a Thermoelectric Material,"* Mater. Lett. **62,** 707-710, 2008.

[110] S. Kentarou, K. Yugo, S. Yuu, T. Kiyohiko, A. Keisuke, O. Toru, U. Noritaka, N. Kiyokazu and S. Yasuhiro, *"On Effects of Gate Bias on Hole Effective Mass and Mobility in Strained-Ge Channel Structures,"* Appl. Phys. Express **1,** 011401, 2008.

[111] T. H. Wu, P. C. Kuo, S. L. Ou, J.-P. Chen, P.-F. Yen, T.-R. Jeng, C.-Y. Wu and D.-R. Huang, *"Diffusion and Crystallization Mechanisms of Ge/Au Bilayer Media for Write-Once Optical Disk,"* Appl. Phys. Lett. **92,** 011126, 2008.

[112] V. Tombelaine, A. Labruyère, J. Kobelke, K. Schuster, V. Reichel, P. Leproux, V. Couderc, R. Jamier and H. Bartelt, *"Nonlinear Photonic Crystal Fiber with a Structured Multi-Component Glass Core for Four-Wave Mixing and Supercontinuum Generation,"* Opt. Express **17,** 15392-15401, 2009.

[113] G. Origlio, M. Cannas, S. Girard, R. Boscaino, A. Boukenter and Y. Ouerdane, *"Influence of the Drawing Process on the Defect Generation in Multistep-Index Germanium-Doped Optical Fibers,"* Opt. Lett. **34,** 2282-2284, 2009.

[114] J. Liu, X. Sun, Y. Bai, K. E. Lee, E. A. Fitzgerald, L. C. Kimerling and J. Michel, *"Efficient above Band Gap Light Emission in Germanium,"* Chin. Opt. Lett. **7,** 271-273, 2009.

[115] A. Alessi, D. Di Francesca, S. Agnello, S. Girard, M. Cannas, N. Richard, A. Boukenter and Y. Ouerdane, *"Evidence of Different Red Emissions in Irradiated Germanosilicate Materials,"* J. Lumin. **177,** 127-132, 2016.

[116] A. Alessi, S. Agnello, S. Grandi, A. Parlato and F. Gelardi, *"Refractive Index Change Dependence on Ge Defects in γ-Irradiated Ge Doped Silica,"* Phys. Rev. B **80,** 014103, 2009.

[117] S. Firstov, I. Bufetov, V. Khopin, A. Umnikov, A. Guryanov and E. Dianov, *"Time-resolved Spectroscopy and Optical Gain of Silica-Based Fibers Co-Doped with Bi, Al and/or Ge, P, and Ti,"* Laser physics **19,** 894-901, 2009.

[118] T. K. Thrivikraman, P. Cheng, S. D. Phillips, J. P. Comeau, M. A. Morton, J. D. Cressler, J. Papapolymerou and P. W. Marshall, *"On the Radiation Tolerance of SiGe HBT and CMOS Based Phase Shifters for Space-Based, Phased-Array Antenna Systems,"* IEEE Trans. Nucl. Sci. **55,** 3246-3252, 2008.

[119] A. Hajimiri, H. Hashemi, A. Natarajan, G. Xiang and A. Komijani, *"Integrated Phased Array Systems in Silicon,"* in Proceedings of the IEEE, 1637-1655, 2005.

[120] P. Russer and L. Vietzorreck, *"Neue Millimeterwellentechnologien für Kommunikation und Sensorik,"* Frequenz **57,** 38-44, 2003.

[121] Xiaoqing Li , Fang He, Guigao Liu, Yuan Huang, Chengfu Pan and C. Guo, *"Fabrication of Ge Quantum Dots Doped TiO_2 Films with High Optical Absorption Properties Via Layer-by-layer Ion-Beam Sputtering,"* Mater. Lett. **67,** 369-372, 2012.

[122] Abdul Faheem Khan, Mazhar Mehmood, Turab Ali and H. Fayaz, *"Structural and Optical Studies of Nanostructured TiO_2–Ge Multi-layer Thin Films,"* Thin Solid Films **536,** 220-228, 2013.

[123] A. Slav, G. E. Stan and A. C. Galea, *"Influence of Deposition Conditions on the Properties of TiO_2 -Ge Nanocomposites,"* IEEE 337-340, 2010.

[124] J.-H. K. Soumen Das, Han Seok Choi, Yong-Kyu Park and Yoon-Bong Hahn, *"Interfacial and Electrical Properties of Solution Processed p-TiO_2 in Heterojunction Devices,"* Electrochem. Commun. **13,** 350-354, 2011.

[125] H.-C. Lin, H.-S. Chen, C.-Y. Su and C. Su, *"Enhanced Efficiency Of TiO_2 Photoanodes Modified With WO_{3-X} Nanomaterials In Dye-Sensitized Solar Cells,"* IEEE 000907-000910, 2009.

[126] T. H. Yongqiang Cao, Yongmei Chen and Yaan Cao, *"Fabrication of Rutile TiO_2-Sn/Anatase TiO_2-N Heterostructure and Its Application in Visible-Light Photocatalysis,"* J. Phys. Chem. C **114,** 3627–3633, 2010.

[127] M. Ohring, "*Materials Science of Thin Films"*, **2**. New York, USA.: Academic Press, 2002.

[128] G. Cao, "*Nanostructures & Nanomaterials-Synthesis , Properties and Applications"*. London: Imperial College Press, 2004.

[129] S. M. Sze and K. K. Ng, "*Physics of Semiconductor Devices"*. New Jersy, USA.: John Wiley & Sons, 2006.

[130] F. C. Frank and J. H. V. Merwe, *"One-dimensional Dislocations. I. Static Theory,"* in Proceedings of the Royal Society of London. Series A. Mathematical and Physical Sciences, 205-216, 1949.

[131] S. N. Santalla, C. K. Malu and R. M. D. l. Cruz, *"Substrate orientation effects on the stranski-krastanov growth mode,"* Nanotechnology **15,** S215-S219, 2004.

[132] R. Eason, "*Pulsed Laser Deposition of Thin Films"*. Hoboken, New Jersey: John Wiley & Sons, Inc, 2007.

[133] G. H. Gilmer and M. H. Grabiw, *"Models of Thin Film Growth Modes,"* J. Met. **39,** 19-23, 1987.

[134] S. Ithurria, M. D. Tessier, B. Mahler, R. P. S. M. Lobo, B. Dubertret and A. L. Efros, *"Colloidal Nanoplatelets with Two-dimensional Electronic Structure,"* Nat. Mater. **10,** 936-941, 2011.

[135] J. A. Venables, "*Introduction to Surface and Thin Film Processes"*. New York, USA.: Cambridge University Press, 2003.

[136] U. Diebold, *"The Surface Science of Titanium Dioxide,"* Surface Science Reports **48,** 53-229, 2003.

[137] Z. Othaman, L. K. Boo, S. Sakrani and R. Muhammad, *"The Stranski-Krastanov Three Dimensional Island Growth Prediction on Sinite Size Model,"* unpublished 2004.

[138] D. K. Schroder, "*Semiconductor Material and Device Characterization"*, 2nd ed. USA: John Wiley & Sons, 2006.

[139] Y. Li, X. Yao and K. Tanabe, *"Improved Surface Morphology of $NdBa_2Cu_3O_7$ Films Grown by Pulsed Laser Deposition Using a Large Single Crystal Target,"* Physica D **304,** 239-244, 1998.

[140] E. Morintale, C.Constantinescu and M. Dinescu, *"Thin Films Development by Pulsed Laser-Assisted Deposition,"* Physics AUC **20,** 43-56, 2010.

[141] Z. Trajanovic, S. Choopun, R. P. Sharma and T. Venkatesan, *"Stoichiometry and Thickness Variation of $YBa_2Cu_3O_7$ in Pulsed Laser Deposition with a Shadow Mask,"* Appl. Phys. Lett. **70,** 3461-3463, 1997.

[142] M. N. Ashfold, F. Claeyssens, G. M. Fuge and S. J. Henley, *"Pulsed Laser Ablation and Deposition of Thin Films,"* Chem. Soc. Rev. **33,** 23-31, 2004.

[143] Y. E. Lee, D. P. Norton and J. D. Budai, *"Enhanced Photoluminescence in Epitaxial $ZnGa_2O_4$:Mn Thin-film Phosphors Using Pulsed Laser Deposition,"* Appl. Phys. Lett. **74,** 3155-3157, 1999.

[144] C. B. Arnold and M. J. Aziz, *"Stoichiometry Issues in Pulsed Laser Deposition of Alloys Grown from Multicomponent Targets,"* Appl. Phys. A **69,** S23-S27, 1999.

[145] T. Venkatesan, *"Pulsed Laser Deposition-Invention or Discovery?,"* J. Phys. D: Appl. Phys. **47,** 034001, 2014.

[146] R.K Singh, P. Tiwari and J. Narayan, *"Nature of Pulsed Laser Deposition Technique and In-Situ Processing of $YBa_2Cu_3O_7$ Superconducting Thin Films.,"* in Processing of Thin Films for High T_c Superconducting Electronics, Santa Clara, United States, 1989.

[147] R. K. Singh and J. Narayan, *"Pulsed Laser Evaporation Technique for Deposition of Thin Films: Physics and Theoretical Model,"* Phys. Rev. B **41,** 8843-61, 1990.

[148] A. T. Mostako and A. Khare, *"Effect of Target–Substrate Distance onto the Nanostructured Rhodium Thin Films Via PLD Technique,"* Appl. Nanosci. **2,** 189-193, 2012.

[149] S. D. Mo and W. Y. Ching, *"Electronic and Optical Properties of Three Phases of Titanium Dioxide: Rutile, Anatase and Brookite,"* Phys Rev B Condens Matter **51,** 13023-13032, 1995.

[150] A. Kaleva, S. Heinonen, J. P. Nikkanen and E. Levänen, *"Synthesis and Crystallization of Titanium Dioxide in Supercritical Carbon Dioxide (scCO$_2$),"* IOP Conference Series: Materials Science and Engineering **175,** 012034, 2017.

[151] J.P. Colinge and C. A. Colinge, "*Physics of Semiconductor Devices"*. USA.: Kluwer Academic Publishers, 2002.

[152] S. Ramanathan, "*Thin Film Metal-Oxides - Fundamentals and Applications in Electronics and Energy"*. New York, USA.: Springer, 2010.

[153] B. J. Thompson, "*Engineering Thin Films and Nanostructures with Ion Beams"*. New York, USA.: Taylor & Francies Group, 2005.

[154] R. F. Egerton, "*Analytical Electron Microscopy,"* in Physical Principles of Electron Microscopy: An Introduction to TEM, SEM, and AFM, USA.: Springer Science and Business Media Inc. 161-165, 2005.

[155] D. P. Norton, C. Park, J. D. Budai, S. J. Pennycook and C. Prouteau, *"Plume-induced Stress in Pulsed Laser Deposited CeO$_2$ Films,"* Appl. Phys. Lett. **74,** 2134-2136, 1999.

[156] T. Orii, M. Hirasawa and T. Seto, *"Tunable, Narrow-Band Light Emission from Size-Selected Si Nanoparticles Produced by Pulsed-Laser Ablation,"* Appl. Phys. Lett. **83,** 3395-3397, 2003.

[157] "*Instrument X-ray Optics*," in School of Crystallography, R. Geometry, Ed. Birkbeck College, University of London, 1997-2006.

[158] S. Moosakhani, A. A. Sabbagh Alvani, A. A. Sarabi, H. Sameie, R. Salimi, S. Kiani and Y. Ebrahimi, *"Non-toxic Silver Iodide (AgI) Quantum Dots Sensitized Solar Cells,"* Mater. Res. Bull. **60,** 38-45, 2014.

[159] S. Velumania, Xavier Mathew, P.J. Sebastian, Sa.K. Narayandass and D. Mangalaraj, *"Structural and Optical Properties of Hot Wall Deposited CdSe Thin Film,"* Sol. Energy Mater. Sol. Cells **76,** 347-358, 2003.

[160] T. Thirugnanasambandan and M. Alagar, "*Titanium dioxide (TiO$_2$) Nanoparticles - XRD Analyses – An Insight*," in ArXive-prints, C. U. Library, Ed., 2013.

[161] K. Klabunde, "*Thin Films from Free Atoms and Particles"*. United Kingdom: Academic Press 1985.

[162] B. D. Cullity and S. R. Stock, "*Elements Of X-Ray Diffraction"*, 3rd ed. USA: Addison-Wesley Publishing Company, Publishikg Company, Inc., 1956.

[163] J. G. Grasselli, M. K. Snavely and B. J. Bulkin, "*Chemical Applications of Raman Spectroscopy"*: John Wiley & Sons Inc, 1981.

[164] K. Nakamoto, "*Infrared and Raman Spectra of Inorganic and co-ordinatin"*, 3rd ed. New York: New York : Wiley, 1978.

[165] J. Christians, "*Raman Spectroscopy*," Spectroscopic Characterization. 2012.

[166] D. A. Skoog and D. M. West, "*Raman Spectroscopy,"* in Principles of Instrumental Analysis, 2nd Philladelphia: Saunders College 262-270, 1980.

[167] J. K. Behera, *"Synthesis and Characterization of ZnO Nano-Particles,"* M. Sc, Physics, National Institute Of Technology, 2009.

[168] J. Heath, "*Energy Dispersive Spectroscopy"*, 2nd ed. Chichester, West Sussex: John Wiley & Sons Ltd, 2015.

[169] A. Mahapatra, *"Fabrication And Characterization Of Novel Iron Oxide/ Alumina Nanomaterials for Environmental Applications,"* PhD, Department of Chemistry, National Institute Of Technology, Rourkela, Rourkela-769008, Odisha, India, 2013.

[170] B. E. A. Saleh and M. C. Teich, "*Fundamentals of Photonics"*, 2nd ed.**2**. New Jersy, USA.: Wiley Interscience 2007.

[171] "*UV- visible Spectrophotometer*," Ed.: Hitachi, 2013.

[172] H. G. Hecht, *"The Interpretation of Diffuse Reflectance Spectra,"* J. Res. Nat. Bureau Stand.-A, Phys. Chem. **80A,** 567-583, 1976.

[173] D. L. Pavia, G. M. Lampman, G. S. Kriz and J. R. Vyvyan, "*Introduction to Spectroscopy"*, 4th ed. United State of America: Brook/Cole Cengage Learning.

[174] V. M. Huxter, *"Optical and Material Properties of Colloidal Semiconductor Nanocrystals,"* Ph. D, Chemistry, University of Toronto, Toronto, 2009.

[175] R. M. A. Azzam and N. M. Bashara, "*Ellipsometry and Polarized Light,"*. North-Holland, Amsterdam, 1989.

[176] E.W. Williams and H. B. Bebb, "*Photoluminescence"*. New York: Academic Press, 1972.

[177] P. J. Dean, *"Photoluminescence as a Diagnostic of Semiconductors,"* Prog. Crystal Growth Charact **5,** 89-174, 1982.

[178] D. A. Neamen, "*Semiconductor Physics and Devices: Basic Principles"*, 4th ed., 1992.

[179] D. A. H. Hanaor and C. C. Sorrell, *"Review of the Anatase to Rutile Phase Transformation,"* J. Mater. Sci **46,** 855-874, 2011.

[180] I. W. Boyd, *"Thin Film Growth by Pulsed Laser Deposition,"* Ceram. Int. **22,** 429-34, 1996.

[181] Y. Zhao and J. Zhang, *"Microstrain and Grain-Size Analysis from Diffraction Peak Width and Graphical Derivation of High Pressure Thermomechanics,"* J. Appl. Crystallogr. **41,** 1095–1108, 2008.

[182] C. W. S. a. T. Lippert, "*Laser Ablation and Thin Film Deposition*," in Laser Processing of Materials: Fundamentals, Applications and Developments, P. Schaaf, Ed. Berlin, Heidelberg: Springer Berlin Heidelberg, 2010.

[183] P. Jafarkhani, S. Dadras, M. J. Torkamany and J. Sabbaghzadeh, *"Synthesis of Nanocrystalline Titania in Pure Water by Pulsed Nd:YAG Laser,"* Appl. Surf. Sci. **256,** 5, 2010.

[184] M. Melvin, D. Kumar and S. Devadason, *"Phase Transformation and Quantum Confinement Effect in CdSe/Se Multilayer Thin Films Prepared by Physical Vapour Deposition.,"* Phase Transitions **86,** 1216-26, 2013.

[185] J. Olivares, P. Martín, A. Rodríguez, J. Sangrador, J. Jiménez and T. Rodríguez, *"Raman Spectroscopy Study of Amorphous Sige Films Deposited by Low Pressure Chemical Vapor Deposition and Polycrystalline SiGe Films Obtained by Solid-Phase Crystallization,"* Thin Solid Films **358,** 56-61, 2000.

[186] S. Nozaki, S. Sato, S. Rath, H. Ono and H. Morisaki., *"Optical Properties Of Tetragonal Germanium Nanocrystals Deposited by the Cluster-Beam Evaporation Technique: New Light Emitting Material for Future.,"* Bull. Mater. Sci. **22,** 1999.

[187] Timdeschaines, Joe Hodkiewicz and Pathenson, "*Characterization of Amorphous and Microcrystalline Silicon using Raman Spectroscopy*," Thermoscientific, Ed. USA.

[188] A. Welte, C. Waldauf, C. Brabec and J. Peter, *"Application of Optical Absorbance for the Investigation of Electronic and Structural Properties of Sol–Gel Processed TiO_2 Films,"* Thin Solid Films **516,** 7256-7259, 2008.

[189] A. F. khan, M. Mehmood, M. Aslam and S. I. Shah, *"Naostructured Multilayer TiO_2-Ge Films with Quantum Confinement Effects for Photovoltaic Applictaions.,"* J. Colloid Interface Sci. **343,** 10, 2010.

[190] Y.-J. Shim and G.-J. Choi, *"Characterization of TiO_2 Quantum Dots Synthesized by Hydrothermal Method,"* Trans. Electrical Electron. Mater. **17,** 125-127, 2016.

[191] S. N. Andrew M. Smith, *"Semiconductor Nanocrystals: Structure, Properties and Band Gap Engineering,"* Acc. Chem. Res. **43,** 190-200, 2010.

[192] J. R. Heath, J. J. Shiang and A. P. Alivisatos, *"Germanium Quantum Dots: Optical Properties and Synthesis,"* The Journal of Chemical Physics **101,** 1607-1615, 1994.

[193] M. Abbas, B. Ali, S. I. Shah and P. Akhter, *"Germanium Quantum Dot Sensitized TiO_2 Solar Cells,"* Key Eng. Mater. **442,** 404-414, 2010.

[194] A. Goyal, A. K. Rumaiz, Y. Miao, S. Hazra, C. Ni and S. I. Shah, *"Synthesis and characterization of Ti O_2 – Ge nanocomposites,"* J. Vac. Sci. Technol., B **26,** 1315-20, 2008.

[195] S. Shahzada, A. Fatima, A. Nazir, A. Mehmood, M. Mehmood and A. Nadeem, *"Structural and optical properties of TiO_2–Ge nanoparticles prepared through laser ablation in liquid medium,"* Can. J. Phys. **95,** 645-649, 2017.

[196] T. Arguirov, M. Kittler and N. V. Abrosimov, *"Room temperature luminescence from Germanium,"* J. Phys: Conf. Series **281,** 012021, 2011.

[197] Y. Makita, *"Novel Features of Photoluminescence Spectra from Acceptor-Doped Gaas: Formation of Acceptor-Acceptor Pair Emissions and Optical Compensation Effect,"* Mater. Sci. Eng. **R16,** 265-398, 1996.

[198] K. W. Sun, S. H. Sue and C. W. Liu, *"Visible photoluminescence from Ge quantum dots,"* Physica E: Low. Dim, Sys. Nanostruct. **28,** 525-530, 2005.

[199] E. B. Kaganovich, D. V. Korbutyak, Y. V. Kryuchenko, I. M. Kupchak, E. G. Manoilov and A. V. Sachenko, *"Exciton States and Photoluminescence in Ge Quantum Dots,"* Nanotechnology **18,** 295401 (5 pages), 2007.

[200] A. R. Gomez, C. M. Sanchez-Hernandez, I. Fleitman-Levin, J. Arenas-Alatorre, J. C. Alonso-Huitron and M. E. S. Vergara, *"Optical Absorption and Visible Photoluminescence from Thin Films of Silicon Phthalocyanine Derivatives,"* Materials **7,** 6585-6603, 201